Ni-Al Layered Double Hydroxide and Oxide Adsorbents for Fluoride Removal and CO_2 Capturing: The Role of Dopants ($Mn^{2+}$and Ce^{4+})

Ararso Nagari Wagassa

A Dissertation Submitted to

The Department of Applied Chemistry

School of Applied Natural Sciences

Presented in Fulfillment of the Requirement for the Degree of Doctor of Philosophy in Applied Chemistry (Specialization in Materials Chemistry)

Office of Graduate Studies

Adama Science and Technology University

June, 2024

Adama, Ethiopia

Ni-Al Layered Double Hydroxide and Oxide Adsorbents for Fluoride Removal and CO_2 Capturing: The Role of Dopants ($Mn^{2+}$and Ce^{4+})

Ararso Nagari Wagassa

Main supervisor: Enyew Amare Zereffa (Assoc. Prof.)
Co-supervisor: Tofik Ahmed Shifa (Assoc. Prof.)
Co-supervisor: Amit Kumar Bansiwal (PhD, Senior Principal Scientist)

A Dissertation Submitted to
Department of Applied Chemistry
School of Applied Natural Sciences

Presented in Fulfillment of the Requirement for the Degree of Doctor of Philosophy in Applied Chemistry (Specialization in Materials Chemistry)

Office of Graduate Studies
Adama Science and Technology University

June, 2024
Adama, Ethiopia

Declaration

I hereby declare that this Dissertation entitled "Ni-Al Layered Double Hydroxide and Oxide Adsorbents for Fluoride Removal and CO_2 Capturing: The Role of Dopants ($Mn^{2+}$and Ce^{4+})" is my original work. That is, it has not been submitted for the award of any academic degree, diploma or certificate in any other university. All sources of materials used for this thesis have been duly acknowledged through appropriate citations.

Ararso Nagari Wagassa		June 2024
Name of student	Signature	Date

Recommendation

I/we, the supervisor(s) of this dissertation, hereby certify that I/we have read and revised the dissertation entitled “Ni-Al Layered Double Hydroxide and Oxide Adsorbents for Fluoride Removal and CO_2 Capturing: The Role of Dopants ($Mn^{2+}$and Ce^{4+})” prepared under my/our guidance by Ararso Nagari Wagassa submitted in partial fulfillment of the requirements for the degree of Doctor of Philosophy in Materials Chemistry. Therefore, I/we recommend the submission of the dissertation to the department for further review and defense.

Dr. Enyew Amare		June 2024
Major Supervisor	Signature	Date
Co-supervisor	Signature	Date

Approval of Ph.D. Dissertation

I/we hereby certify that the recommendations and suggestions made by the board of examiners are appropriately incorporated into the final version of the dissertation entitled "Ni-Al Layered Double Hydroxide and Oxide Adsorbents for Fluoride Removal and CO_2 Capturing: The Role of Dopants ($Mn^{2+}$and Ce^{4+})" by Ararso Nagari Wagassa.

Major Supervisor	Signature	Date
Co-supervisor	Signature	Date

We, the undersigned, members of the Board of Examiners of the dissertation open defense by Ararso Nagari Wagassa have read and evaluated the dissertation entitled "Ni-Al Layered Double Hydroxide and Oxide Adsorbents for Fluoride Removal and CO_2 Capturing: The Role of Dopants ($Mn^{2+}$and Ce^{4+})" and examined the candidate during open defense. This is, therefore, to certify that the dissertation is accepted for partial fulfillment of the requirement of the degree of Doctor of Philosophy in Materials Chemistry.

Chairperson	Signature	Date
Internal Examiner	Signature	Date
External Examiner 1	Signature	Date
External Examiner 2	Signature	Date

Finally, approval and acceptance of the dissertation is contingent upon submission of its final copy to the Office of Postgraduate Studies (OPGS) through the candidate's Department Graduate Council (DGC) and School Graduate Committee (SGC).

Department Head	Signature	Date
School Dean	Signature	Date
Office of Postgraduate Studies, Dean	Signature	Date

ACKNOWLEDGEMENT

I would like to express my sincere gratitude to my research advisors, Dr. Enyew Amare, Dr. Tofik Ahmed, and Dr. Amit Bansiwal, for their invaluable guidance, patience, and direction throughout my PhD journey. Their support played a significant role in my success.

My deepest appreciation goes to Dr. Amit Bansiwal for providing me with an extraordinary amount of experimental and intellectual freedom during my time in his lab. This fostered my independence and creativity, and I am incredibly grateful for his trust and support. I am also grateful to all members of Dr. Amit's group: Mr. Shahank, Ms. Shraddha Manekar, and Ms. Sophiya Sonaker. Their camaraderie, support, and shared experiences have enriched my PhD journey. I have learned immensely from them and hope to have contributed back to their learning as well.

My appreciation extends to all staff of the Applied Chemistry Department of ASTU, especially Dr. Lema Teshome for his assistance with material characterization in South Korea and other support. My appreciation also extends to Mr. Demeke Tesfaye of the Materials Science and Engineering Department at Adama Science and Technology for his assistance with material characterization by XRD and others.

Finally, I would like to express my deepest gratitude to my family and friends for their unwavering encouragement and support. This journey would not have been possible without them. In particular, I am incredibly grateful to my wife, Rahel Bekele, for her unwavering love, patience, and encouragement throughout my PhD journey, filled with both triumphs and challenges, was instrumental in my success.

I strongly appreciate ASTU and Ambo University for allowing me to pursue my PhD study. I also gratefully acknowledge the financial support provided by TWAS-UNESCO, CSIR, and CSIR-NEERI, which made this research possible.

TABLE OF CONTENTS

LIST OF TABLES

LIST OF FIGURES

List of Acronyms and Abbreviations

ATR FT-IR	Attenuated total reflection Fourier-transform infrared
BET	Brunauer-Emmett-Teller
CNAH	Ce^{4+}-doped Nickel-Aluminium hydroxide
CNAO	Ce^{4+}-doped Nickel-Aluminium oxide
DSC	Deferential scanning calorimetry
EDS	Energy dispersive X-ray spectroscopy
HR-TEM	High-resolution transmission electron microscopy
ISE	Ion selective electrode
LDH	Layered double hydroxide
LDO	Layered double oxide
MFC	Mass flow controller
MNAH	Mn^{2+}-doped Nickel-Aluminium hydroxide
MNAO	Mn^{2+}-doped Nickel-Aluminium oxide
NAH	Nickel-Aluminium hydroxide
PFO	Pseudo-first order
PSO	Pseudo-second order
SAED	Selected area electron diffraction
SEM	Scanning electron microscopy
SSR	Sum of the squared residuals
TGA	Thermogravimetric analysis
XPS	X-ray photoelectron spectroscopy
XRD	X-ray diffraction

Abstract

Environmental pollution, a major global concern, is caused by various harmful pollutants including fluoride and CO_2. They pose specific threats. CO_2, a major greenhouse gas, causes climate change and global warming, while excessive fluoride intake can lead to detrimental health problems like fluorosis. This study explored the potential of layered double hydroxides (LDHs) and layered double oxides (LDOs) for removing fluoride from water and capturing CO_2 from flue gas. Mn^{2+} and Ce^{4+} doped Ni-Al LDHs and LDOs were synthesized through the co-precipitation method. The synthesized materials were characterized using advanced microscopic, spectroscopic, X-ray Diffraction (XRD), Thermogravimetric Analysis (TGA)/Differential Scanning Calorimetry (DSC) and Brunauer-Emmitt-Teller (BET) characterization techniques. The crystallographic structural analysis by XRD showed that the intended LDHs and LDOs were obtained. ATR FT-IR results indicated the presence of essential functional groups in the LDHs and LDOs. XPS confirmed the existence of all the constituent elements in their intended oxidation states. The EDS analysis confirmed a uniform distribution of the intended elements throughout the materials. The composition closely matched the target ratio. The TEM/HRTEM characterization confirmed the successful formation of nano-sized sheet-like LDHs and LDOs. The BET analysis indicated a high surface area of 189 m^2/g for the Ce^{4+}-doped Ni-Al LDO. These materials exhibited significant adsorption performance towards fluoride. The LDOs showed good saturation capacities in CO_2 capture. Doping with Mn^{2+} and Ce^{4+} significantly enhanced fluoride and CO_2 adsorption. LDHs outperformed LDOs, demonstrating an adsorption capacity of 238.27 mg/g for fluoride removal, as confirmed by the Langmuir model. The proposed mechanisms for F^- adsorption involved a combination of ion exchange, hydrogen bonding and surface complexation. Furthermore, a remarkable CO_2 saturation capacity of 14.09 mmol/g was achieved for Ce^{4+}-doped Ni-Al LDO. Regeneration studies indicated good stability for Ce^{4+}-doped LDOs. Fixed-bed models provided further support for the experimental observations. The study revealed that CO_2 capture likely involved a combination of mechanisms such as bidentate and monodentate interactions, and bulk carbonate formation, as evidenced by the ATR FT-IR and XRD analysis of the used adsorbents. In conclusion, this study successfully demonstrated the potential of Mn^{2+} and Ce^{4+} doped Ni-Al LDHs and LDOs as efficient and sustainable adsorbents for fluoride removal and CO_2 capture. Their performance highlighted their potential for mitigating environmental pollution and contributing to a cleaner and healthier future.

***Keywords**: Layered double hydroxides, Layered double oxides, Co-precipitation, Carbon dioxide, Fluoride, Packed-bed column, Breakthrough curve analysis, Adsorption*

CHAPTER 1

INTRODUCTION

1.1. Background of the Study

Environmental pollution refers to the introduction of harmful substances or products into the environment. These harmful substances, known as pollutants, can be natural, such as volcanic ash, or human-made, such as car exhaust fumes and industrial wastes. The three primary types of environmental pollution are air pollution, water pollution, and land pollution (Landrigan and Fuller, 2012). Air pollution arises from the release of harmful substances into the atmosphere, originating from sources like car exhaust, factory emissions, and power plants. It can trigger various health issues, including respiratory infections, heart disease, and cancer (Palupi and Abeng, 2023; Walters, 2014). Water pollution involves the contamination of water bodies, encompassing groundwater, rivers, lakes, and oceans. Sewage, agricultural runoff, and industrial wastes are among the primary sources of water pollution. Its consequences include rendering water unsafe for drinking and harming aquatic life (Shah *et al*., 2020). Land pollution refers to the contamination of soil, often caused by landfills, industrial wastes, and agricultural chemicals. It can lead to soil infertility and contamination of food crops (Balseiro-Romero and Baveye, 2018).

Environmental pollution, specifically air pollution, also contributes to climate change. Climate change is a modern-day threat that has been widely acknowledged worldwide. Greenhouse gases (GHGs), such as carbon dioxide (CO_2), methane (CH_4), chlorofluorocarbons (CFCs), and nitrous oxide (N_2O) that trap heat from the sun leading to a gradual rise in Earth's temperature resulting in global warming and climate change, a pressing issue of the time (Lee *et al*., 2023; Tiwari *et al*., 2017).

Among these GHGs, CO_2 poses the most significant threat to the environment which accounts 78% of the total emission. The primary sources of CO_2 emissions are carbon-emitting fuels such as coal, petroleum, natural gas, and other non-renewable resources. Fossil fuel-powered power plants are the leading emitters of CO_2, contributing to about three-fourths of the global increase in CO_2 levels (Ochedi *et al*., 2021; Osman *et al*., 2020;

Sharma and Maréchal, 2019; Zeng *et al*., 2022). According to the Intergovernmental Panel on Climate Change (IPCC), carbon dioxide concentration in the atmosphere has increased by more than 47% since 1750. This rise, from 280 ppm in the pre-industrial era to around 415 ppm in 2021, is projected to continue potentially reaching 570 ppm by 2100. This alarming increase in CO_2 levels could lead to a rise of approximately 2.8 °C in the mean global temperature and an increase of 38 meters in the mean sea level, posing severe challenges to ecosystems and human societies worldwide (Amiri *et al*., 2017; Lee *et al*., 2023; Sabouni *et al*., 2013; Tiwari *et al*., 2017).

Combating the alarming rise in atmospheric CO_2 emissions requires a multifaceted approach that encompasses a range of mitigation strategies. These strategies can be broadly categorized into four main areas such as enhancing energy efficiency, transitioning to renewable energy sources, implementing geo-engineering approaches and carbon capture and sequestration/storage (CCS) (Osman *et al*., 2020; Razzaq *et al*., 2023).

Implementing energy-efficient practices and adopting energy-saving technologies in various sectors, such as buildings, transportation, and industrial processes, can significantly lower energy demand, thereby reducing CO_2 emissions. Upgrading energy conversion devices, such as power plants and industrial machinery, to operate with higher efficiency can significantly reduce the amount of energy required to produce a given amount of output, leading to lower CO_2 emissions (Ang *et al*., 2023; Razzaq *et al*., 2023; Sturchio and Knapp, 2023). Replacing fossil fuels with renewable energy sources like solar, wind, geothermal, and hydropower can drastically reduce CO_2 emissions from electricity generation and other energy-intensive sectors. Incorporating low-carbon fuels like natural gas, hydrogen, or nuclear power into the energy mix can help bridge the gap during the transition to a fully renewable energy system (Kumar *et al*., 2022; Sturchio and Knapp, 2023; Xu *et al*., 2023). Expanding forest cover through afforestation and reforestation projects can enhance carbon sequestration, as trees absorb CO_2 from the atmosphere. Preserving existing forests is crucial for maintaining their carbon sequestration capacity and preventing the release of stored CO_2 (Chen *et al*., 2020; Lawrence *et al*., 2018). CCS technology involves capturing CO_2 from flue gas emissions, typically from power plants or industrial facilities, using various adsorbents. The captured CO_2 can be stored underground in geological formations or utilized to produce valuable products like bioplastics or fuels (Anderson *et al*., 2023; Osman *et al*., 2020).

While each strategy offers a unique contribution to mitigating CO_2 emissions, a synergistic approach that combines these methods is essential to effectively address the climate crisis. CCS, in particular, can play a significant role in achieving deep decarbonization goals, especially in sectors where transitioning away from fossil fuels is challenging. CCS is a suite of technologies that aim to mitigate climate change by capturing and storing CO_2 emissions from industrial processes and power plants. CCS involves three main approaches such as pre-combustion capture, oxy-combustion and post-combustion capture. The choice of CCS technology depends on several factors, including the type of fuel being used, the emission source, and the desired capture rate (Amiri *et al*., 2017; Gabrielli *et al*., 2020).

In pre-combustion capture, the fuel is converted into a gas mixture of hydrogen and CO_2 before it is burned. The hydrogen is separated and can be used as a clean fuel, while the CO_2 is easily captured and compressed for transport and storage. This approach is particularly well-suited for integrated gasification combined cycle (IGCC) power plants, which use coal or other fossil fuels to produce both electricity and hydrogen. Pre-combustion capture is generally considered the most efficient CCS technology, but it is also the most expensive. Oxy-combustion involves burning fuel in a pure oxygen environment, rather than in the mixture of oxygen and nitrogen found in ambient air. This process produces a flue gas that is primarily composed of CO_2 and water vapor, making it easier to capture CO_2 using various methods, such as absorption or membrane separation. Oxy-combustion is suitable for a range of industrial applications, including power generation, cement production, and steel manufacturing. Oxy-fuel combustion is a promising alternative that is more mature and less expensive than pre-combustion capture. Post-combustion capture involves separating CO_2 from flue gases after combustion has occurred. This approach is the most mature and widely used CCS technology, and it can be applied to existing power plants and industrial facilities. Common post-combustion capture methods include absorption using liquid solvents, adsorption using solid sorbents, and membrane separation. Post-combustion capture is the most widely used CCS technology, but it is the least efficient. Generally, CCS is a promising technology for mitigating climate change, but it is still at an early stage of development. Further research and development are needed to improve the efficiency and cost of CCS technologies (Al Mesfer and Danish, 2018; Amiri *et al*., 2017; Osman *et al*., 2020; Raganati *et al*., 2021).

CO_2 capture from various gas streams is a crucial process for mitigating climate change. Various technologies, including absorption, adsorption, cryogenic separation, and membrane separation, have been explored for CO_2 capture. Absorption using alkanolamines is a common method, but it suffers from drawbacks such as high corrosion, degradation overtime, and the energy penalty associated with regenerating alkanolamines. Cryogenic separation, though effective for high CO_2 concentrations, is energy-intensive and costly. Membrane separation, while a newer technique and promising, faces limitations in terms of CO_2 concentration requirements (minimum 10%) and energy consumption (Farooq *et al*., 2020).

To address these limitations, adsorption using various adsorbents, such as activated carbon, zeolites, mesoporous silica materials, layered double hydroxides, and amine-enriched sorbents, has been investigated. Among these adsorbents, layered double hydroxides (LDHs) have emerged as particularly promising candidates due to their high adsorption efficiencies. This is the result of their properties such as high surface area, tunability, good thermal and mechanical stability, ion-exchange capacity, and the ability to be regenerated over multiple cycles. LDHs are environmentally friendly materials (Albuquerque *et al*., 2016; Lai *et al*., 2021; Osman *et al*., 2020; Santamaría *et al*., 2023).

LDHs are two-dimensional nanomaterials with a layered structure, represented by the general formula $[M_{1-x}^{2+}M_x^{3+}(OH)_2]^{x+}(A^{n-})_{x/n}\cdot zH_2O$. In contrast to most cationic clays, M^{2+} and M^{3+} cations in LDHs are well-distributed within the layers and can be substitutionally doped with metal ions of similar radius to Mg ions over a wide range, enabling control over the properties of the layers (Amiri *et al*., 2017; Gabrielli *et al*., 2020; Osman *et al*., 2020). The interlayer ions of natural LDHs are typically inorganic anions, such as carbonate ions. However, other inorganic anions (such as NO_3^-, Cl^-) and organic ions can also be intercalated into LDHs, providing great versatility in composition. This versatility allows LDHs with various properties to be synthesized for applications in various fields, including adsorbents, base catalysts and supports, inorganic flame retardants, and heat stabilizers for polyvinyl chloride (Wang *et al*., 2022).

The CO_2 adsorption capacity of LDHs, and even more so, the layered double oxides (LDOs) produced by their calcination, makes them potential candidates for effective CO_2 solid adsorbents due to the tunable basicity on the surface of LDHs and LDOs (Yang *et al*., 2019).

For instance, (Wang *et al*., 2022) explored the influence of intercalation and calcination temperature on the MgAl-LDH derived adsorbents on the CO_2 adsorption capacity and obtained improved adsorption capacity of 0.85 mmol/g. (Tang *et al*., 2018) reported (3-aminopropyl)triethoxysilane (APS)-modified MgAl-LDH, demonstrating that the addition of APS improved CO_2 capacity to 2.09 mmol/g. While previous studies have attempted to modify Mg-Al based LDOs by calcination at different temperatures or introducing other molecules as intercalate, these methods have still resulted in relatively low adsorption capacities. The present work aimed to modify the CO_2 adsorption capacity of Ni-Al LDO by incorporating Mn^{2+} and Ce^{4+} as dopants. The LDOs were obtained by calcination from their LDH precursors synthesized using the coprecipitation method. CO_2 removal studies were carried out in a packed-bed adsorption column. To the best of our knowledge, there were no prior research reports on CO_2 adsorption on Mn^{2+} and Ce^{4+}-doped Ni-Al LDOs derived from their hydrotalcite-like LDHs. The novel in-lab-built packed-bed column set-up as well as experimental conditions studied in this work, namely, room temperature and atmospheric pressure have also not been used so far.

Another environmental issue is access to clean water, a critical issue facing humankind today. About 2.2 billion people still lacked access to safely managed water services (Organization, 2020; UNICEF, 2024). These challenges are further intensified by the increasing pollution of water sources by both natural and human-made (Ali and Khan, 2017; Tian *et al*., 2017). Natural sources of water pollution include weathering of rocks, soil erosion, and volcanic activity. Human activities like industrial processes, agriculture, and fossil fuel combustion also significantly contribute to water contamination (Ghosh *et al*., 2012). As a result, water pollution has become a major public health concern globally. Common water pollutants include heavy metals, anions, pesticides, and organic compounds (Tian *et al*., 2017).

Fluoride (F^-) is a major pollutant released from various industrial activities to the water bodies. As a monatomic anion, fluoride is a chemically active element that cannot exist on its own in nature. It is abundantly found on Earth, mainly in rocks, soils, and oceans. Long-term consumption of water with high fluoride concentration can induce fluorosis of bones and teeth, as well as infertility and anemia. Due to the risk of bone and dental fluorosis (Demelash *et al*., 2019; Dessalegne *et al*., 2016; Liu *et al*., 2019), many countries, including Ethiopia and India, struggle to meet the WHO's fluoride standard of 1.5 mg/L in drinking

water (Cai *et al*., 2018a; Haseena *et al*., 2017). Consequently, removing or minimizing fluoride content is essential for safe drinking water.

Adsorption is one of the most promising technologies for fluoride removal. Adsorption offers several advantages for pollutant removal from water as it is versatile, efficient, selective, regenerable, scalable, easily operated, requires minimal energy input and can be integrated with other water treatment processes (Keller and Staudt, 2005).

Adsorption involves binding the molecules to the surface of solid materials, such as activated carbon, zeolites, metal-organic frameworks (MOFs), or layered double hydroxides (LDHs) (Sharifi-Bonab *et al*., 2020). LDHs, a class of anionic clay materials composed of metal hydroxides and carbonate molecules, offer several advantages over other adsorbents, including high adsorption capacity, selectivity, and chemical stability (Crini *et al*., 2018; Tang *et al*., 2018). LDHs are a type of layered inorganic material composed of brucite-like sheets of metal hydroxide ($M(OH)_2$) in which some divalent cations (M^{2+}) are substituted with trivalent cations (M^{3+}) and interlayer anions (A^{-n}). The brucite-like sheets possess a positive charge due to the presence of M^{3+}. Charge compensation occurs through the presence of charge compensating anions and molecules within the interlayer region (Crini *et al*., 2018).

Recently, several papers have proposed high-valent rare-earth and transition elements such as Ce, Zr, and La as modifiers of adsorbents that can selectively complex with fluoride ions and provide an active site for ion-exchange to improve the defluoridation performance of adsorbents (Cai *et al*., 2018b). Only some of the studies containing Ce such as Ce-MOFs (Tang *et al*., 2023), Ce-AlOOH (Tao *et al*., 2020), CeO_2/SiO_2 (Lin *et al*., 2018), and Fe-Al-Ce (Wu *et al*., 2007) have been reported to have promising fluoride removal efficiencies. Compared to other rare-earth elements, Ce modification is largely believed to meaningfully enhance fluoride removal (Tao *et al*., 2020). Ce^{4+}-doped Ni-Al LDHs and LDOs have not been reported so far for fluoride removal from aqueous solutions.

LDHs containing metals such as Mn, Al, etc., have a strong affinity for fluoride (Mullick and Neogi, 2019). Due to their distinct electrical, structural and surface characteristics, transition metal ions like Mn^{2+} have shown tremendous potential for doping in this material (Gao *et al*., 2022; Li *et al*., 2019). Previous studies (Mullick and Neogi, 2019) have shown

that Mn^{2+} doping enhances the stability and mechanical properties of LDHs. While these previous studies have applied to defluoridation, few have used Mn-containing LDHs (Li *et al*., 2019; Mullick and Neogi, 2019). They did not use Mn^{2+}-doped Ni-Al LDHs and LDOs to remove fluoride from the aqueous solution to the best of our knowledge.

Modifying of LDHs can be achieved through doping with different metals and calcination to form LDOs. These processes alter the properties of LDHs, such as their surface area, basicity, and anion exchange capacity. These changes can impact the performance of LDHs in various applications, including CO_2 capture and fluoride removal (Amiri *et al*., 2017; Raganati *et al*., 2021; Reddy *et al*., 2021). Doping LDHs with other metal ions, such as manganese (Mn^{2+}) and cerium (Ce^{4+}), can enhance their adsorption performance. So, this study was focused on Mn^{2+} and Ce^{4+} doped Ni-Al LDHs and LDOs for F^- removal and Mn^{2+} and Ce^{4+} doped Ni-Al LDOs for CO_2 capturing.

1.2. Statement of the Problem

CO_2 and Fluoride are the two major pollutants that can have a significant negative impact on human health and the environment. CO_2 is a major greenhouse gas that contributes to climate change and global warming. CO_2 emissions from human activities, such as the burning of fossil fuels, are increasing at an alarming rate. There is a growing need for technologies that can capture CO_2 emissions from industrial sources and prevent them from being released into the atmosphere (Shukla *et al*., 2022). Current efforts to capture CO_2 emissions from power plants and industrial sources face limitations, including high costs, energy intensity, and the use of hazardous chemicals.

Fluoride is a naturally occurring mineral that is essential for human health in small amounts. However, excessive fluoride consumption can lead to a number of health problems, including fluorosis, which can cause severe health effects such as dental and skeletal deformities (He *et al*., 2019). Fluoride contamination of drinking water is a major public health problem in many parts of the world. According to the World Health Organization, over 180 million people worldwide are exposed to fluoride levels in drinking water that exceed the recommended limit of 1.5 mg/L (Podgorski and Berg, 2022). Existing methods for fluoride removal are often energy-intensive, produce harmful byproducts, and have limited effectiveness.

The development of efficient and cost-effective materials for CO_2 capture and fluoride removal is a critical for mitigating climate change and protecting human health. Layered double hydroxides and oxides, have emerged as promising materials for CO_2 capture and fluoride removal due to their tunable structure, high surface area, layered structure, chemical stability, and anion exchange capacity. Ni-Al LDHs and LDOs have shown promise for these applications, but their performance can be further enhanced by doping with appropriate metals and calcination to high temperature.

Therefore, this study focused on the synthesis and characterization of Mn^{2+} and Ce^{4+} doped Ni-Al LDHs and LDOs, investigating their potential for capturing CO_2 from simulated flue gas and removing fluoride from aqueous solutions.

1.3. Objective of the Study

1.3.1. General Objective

This study aimed to synthesize and characterize Mn^{2+}-doped and Ce^{4+}-doped Ni-Al LDHs and LDOs to investigate the role of the dopants on the performance of Ni-Al LDH and LDO to remove fluoride from aqueous solution and capture CO_2 from simulated flue gas.

1.3.2. Specific Objectives

The specific objectives of the study were to:

- Synthesize Mn^{2+} and Ce^{4+}-doped Ni-Al LDHs and LDOs with the mole ration of divalent to trivalent of 3:1 in the pristine Ni-Al LDH and LDO using the coprecipitation method.
- Characterize the synthesized LDHs and LDOs using XRD, ATR FT-IR, XPS, EDS, SEM, TEM/HRTEM, SAED, BET and TGA/DSC.
- Investigate the fluoride removal efficiency of the synthesized LDHs and LDOs from aqueous solution and the effect of factors such as pH, initial concentration, dose, contact time, temperature, agitation speed and co-existing that influence the fluoride removal efficiency.

- Investigate the CO_2 capturing performance of the synthesized LDOs from simulated flue gas and the effect of factors such as flow rate, adsorbent amount, and packed-bed column length that influence the CO_2 capture performance.

1.4. Significance of the Study

The uncontrolled presence of CO_2 in air and fluoride (F^-) in water sources poses significant threats to human health and the environment. CO_2 emissions contribute to climate change and global warming, while elevated F^- levels in water can cause dental fluorosis and skeletal problems. Therefore, efficient removal or reduction of these contaminants from air and water sources is crucial.

While various materials have been explored for CO_2 and F^- removal, efficiency, selectivity, stability and regeneration remain a major challenge. The existing adsorbents often lack sufficient selectivity, stability and regeneration, requiring larger quantities for effective treatment. This can lead to higher costs, reduced efficiency, and potential secondary environmental impacts.

This study addresses these challenges by exploring the potential of Mn^{2+} and Ce^{4+}-doped Ni-Al LDHs and LDOs for improving the selectivity and efficiency of Ni-Al LDH and LDO materials in CO_2 and F^- removal. The successful development of recyclable, selective and highly effective Mn^{2+} and Ce^{4+}-doped Ni-Al LDHs and LDOs for CO_2 and F^- removal could offer significant environmental benefits by reducing greenhouse gas emissions through efficient CO_2 capture, providing cleaner drinking water by effectively removing F^- contamination and contributing to more sustainable environmental remediation strategies. Significantly, this research aligns with the United Nations Sustainable Development Goals (SDGs), particularly SDG 13 (Climate Action) and SDG 10 (Reduced Inequalities). By developing materials for CO_2 capture, this work contributes to mitigating climate change, a cornerstone of SDG 13. Similarly, the development of materials for fluoride removal can improve water quality, especially in regions facing water scarcity and contamination, thus addressing SDG 10. Furthermore, the findings from this dissertation can potentially contribute to the objectives outlined in the United Nations Climate Change Conference (COP 28) by providing insights into novel materials for carbon capture technologies.

Generally, the findings of this study hold significant potential for advancing the field of environmental remediation by developing advanced and effective materials for selective and efficient CO_2 and F^- removal from air and aqueous solution, contributing to a cleaner and healthier environment.

1.5. Scope of the Study

This research is focused on the synthesis and characterization of Ni-Al LDHs and LDOs doped with Mn^{2+} and Ce^{4+} for fluoride removal from aqueous solutions and CO_2 capturing from simulated flue gas. The materials were synthesized using the co-precipitation method. Various characterization techniques such as XRD, SEM, HRTEM, EDS, SAED, XPS, FT-IR, TGA and BET were employed to analyze the crystal structure, morphology, surface area and elemental composition of the synthesized materials. Batch adsorption technique was applied to study the fluoride adsorption performances of the materials, while in-lab-built setup of a packed-bed column was used for the CO_2 capturing experiments. Breakthrough curve analysis evaluated the CO_2 saturation capacities of the materials. The influence of various factors on both processes were investigated. For fluoride adsorption, the influence of factors such as pH, temperature, agitation rate, dosage, initial fluoride concentration, and coexisting ions were investigated. Similarly, the effects of gas flow rate, adsorbent amount, and packed column length on CO_2 capture were studied.

CHAPTER 2

LITERATURE REVIEW

Layered double (hydro)oxides (LDHs/LDOs) have emerged as promising adsorbents due to their unique properties like tunable structure, high surface area, and diverse functionalities. This review delves into specific applications of LDHs/LDOs in adsorption, structural and physicochemical properties of LDHs/LDOs, synthesis and modification methods of LDHs, explores recent advancements in their research, and applications in water treatment and air purification, and compares their performance with other adsorbents.

2.1 Layered Double Hydroxides

Layered double hydroxides are versatile and emergent class of two dimensional inorganic layered nanomaterials, natural or synthetic anionic clay minerals, of which the general formula is $\left[M_{1-x}^{II} M_{x}^{III} (OH)_2\right]^{x+} (A^{n-})_{x/n}.yH_2O$, with $[M_{1-x}^{II} M_{x}^{III} (OH)_2]^{x+}$ representing the layer and $(A^{n-})_{x/n}.yH_2O$ the interlayer composition, where M^{II} is a divalent ion, M^{III} is a trivalent ion, A^{n-} is an anion and charge density of LDH layers, x is the mole ratio of M^{III} per total cations i.e. $M^{III}/(M^{II}+M^{III})$ whose value lies between 0.2 and 0.33 for pure LDH phase. This formula gives rise to a generic layer sequence $[AcBZAcB]_n$ for layered double hydroxides in which A and B represents layers of hydroxide anions, c represents layers of metal cations and Z represents layers of other anions such as carbonate ion, chloride ion, nitrate ion, etc. and neutral molecules like water molecules. Hydrotalcite is one of the naturally occurring LDH clays and the parent member of the family layered double hydroxides with the chemical formula $Mg_6Al_2(OH)_{16}CO_3.4H_2O$ and its name attributable to high water content (hydro) and talc like appearance. Its existence was first declared by Hochstetter in 1842 and synthesized 100 years later by Feitknecht. It is most common and its structure and properties were studied extensively and is considered as the representative of LDHs. So, LDHs are also known as hydrotalcite-like compounds (Daniel and Thomas, 2020; Forano *et al*., 2013; Grosu, 2018; Mishra *et al*., 2018).

Takovite, a natural mineral with the formula $Ni_6Al_2(OH)_{16}CO_3.4H_2O$ belongs to the large class of layered double hydroxides (LDHs) and contains positively charged Ni(II) and Al(III)

layers alternating with layers containing carbonate ions and water molecules. Mesoporous takovite-type layered double hydroxides (LDH) of the general formula $[Ni_{1-x}Al_x(OH)_2]^{x+}(CO_3^{2-})_{x/2}.nH_2O$ (Jitianu *et al*., 2013).

2.2 Structural and Physicochemical Properties of LDHs

The structure of LDHs (Figure 1) can be easily reviewed by comparing its structure with that of brucite which has the formula $Mg(OH)_2$. Brucite has hexagonal close packing of hydroxide ions in which alternate octahedral sites are occupied by Mg^{2+} ions so that hydroxide layers are neutral (Figure 1a & b). The neutral hydroxide layers are stacked one upon the other and held together by Vander Waal's force of attraction that results in a basal spacing of about 0.48 nm. It can be imagined that the substitution of some divalent ions in brucite structure by some trivalent ions isomorphously results in the formation of positively charged mixed metal hydroxide layers $[M^{II}_{1-x}M^{III}_x(OH)_2]^{x+}$ and the intercalation of anions in the interlayer regions counter balance the residual positive charge on the metal hydroxide layers looking like layered double hydroxide structures. Water molecules in the interlayer region bind to the metal hydroxide layers and anions via extensive hydrogen bonding and; help to stabilize the crystal structure of LDHs. Due to the intercalation of water molecules and anions in the interlamellar region, the basal spacing has been increased from 0.48 nm in brucite to about 0.77 nm in hydrotalcite (Basu *et al*., 2014; Daniel and Thomas, 2020).

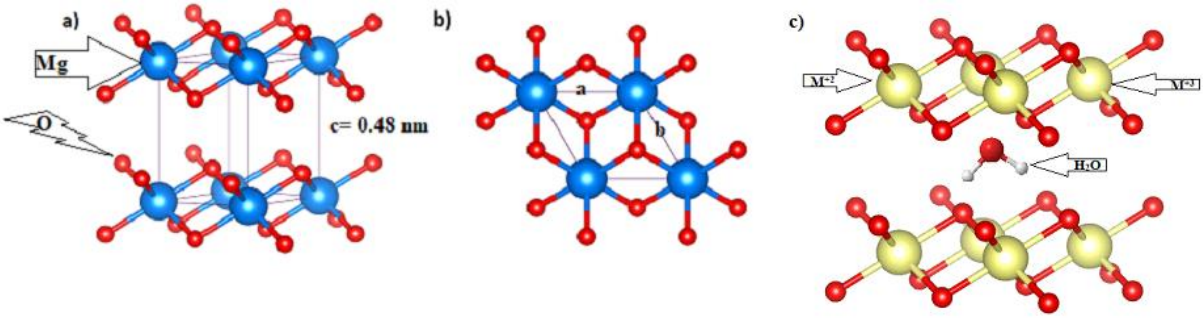

Figure 1. Representation of the brucite structure (a) side and (b) top view and (c) the structure of a generic LDH.

The LDHs are emerging 2D materials with numerous properties that can be tuned through the incorporation of different divalent and trivalent cations, and interlayer ions and molecules in the brucite-like structure utilizing different synthesis methods and modification strategies. The most common properties of LDHs studied so far are optical properties (Daniel and Thomas, 2020; Lin *et al*., 2017; Monzó *et al*., 2019), ion-exchange properties

(Almoisheer *et al*., 2019; Mir *et al*., 2020), magnetic properties (Milanovic, 2016), catalytic capacities (Cabrera-Munguia *et al*., 2020; He *et al*., 2017; Zhou *et al*., 2021), adsorption capacities (Jiang *et al*., 2020; Lei *et al*., 2017; Zhang *et al*., 2018; Zhou *et al*., 2021), electrochemical properties (Baig and Sajid, 2017; Baig *et al*., 2019; Prevot *et al*., 2020; Wang *et al*., 2021), dielectric properties (Daniel and Thomas, 2020; Sokol *et al*., 2019a), swelling properties and ability to intercalate different types of anions and memory effect after calcination (Prasad *et al*., 2018), etc. These properties of LDHs enabled them to be used for different applications such as environmental remediation (water purification, soil remediation, and air mitigation) through adsorption and catalytic degradation, medicine (e.g., drug delivery), food (e.g., preservative), energy (e.g., super-capacitors, H_2 generation from water), catalyst support, electronics, and sensor (e.g., specific electrode preparation). Among these applications of LDHs, the adsorptive application for environmental remediation overshadows due to its most common ion-exchange properties.

The layers in LDHs accommodate cations with two different oxidation states, which can induce different magnetic interactions of the cations' unpaired electrons. Introducing magnetic substrates into already magnetic like layers is open for further new magnetic compounds. Magnetism in LDHs is controlled by two main parameters: (1) the in-layer magnetic super-exchange between metal centers through OH bridges and (2) the less intense dipolar interactions between the individual layers. If one assumes a cation-ordered LDH with a metal cation compositional ratio of 2:1 (x = 0.33), then each M(III) cation will be surrounded by six M(II) cations, and each M(II) will be surrounded by three M(II) and three M(III), which gives M(II)-OH-M(III) and M(II)-OH-M(II) coupled pairs, respectively. For instance, for the NiFe LDH system the coupled pairs Fe(III)-OH-Fe(III) give antiferromagnetic interactions while the coupled pairs of Ni(II)-OH-Fe(III)/Fe(III)-OH-Ni(II) give ferromagnetic interactions, and for the NiMn LDH system the antiferromagnetic interactions come from the Mn(III)-OH-Mn(III) and Ni(II)-OH-Mn(III)/Mn(III)-OH-Ni(II) couplings, while the ferromagnetic interactions come from the Ni(II)-OH-Ni(II) coupling. The magnetic properties can therefore be efficiently modified by carefully choosing the M(II) and M(III) cations and their compositional ratio (in-layer interactions), as well as varying the interlayer distance by the ability of introducing different interlayer anions (between layer interactions). By changing the compositional ratio of the cations (varying x value) one can adjust the relative number of ferromagnetic and antiferromagnetic pairs within the layer (Milanovic, 2016).

2.3 Synthesis Methods of LDH Materials

As it was explained previously, generally LDHs can be of natural origin or synthetic. The main advantage of synthesizing LDHs is the ability to excellently tune their properties in view of the specific application. In this perspective, the appropriate combination of reactants in specific M^{II}/M^{III} mole ratio to be adopted. The most important factors to be considered are the nature of metallic cations, the concentration of reactants, pH, temperature, aging time, and preparation method to synthesize LDH with different particle sizes, morphology and crystallinity. Generally, the crystallinity of LDH increases with rising temperature in the synthesis process, while reducing the lateral size further is challenging due to rapid crystallization kinetics and/or aggregation of sheets (Chaillot *et al*., 2021; Jiang *et al*., 2020).

Several synthesis methods have been developed throughout the last decades, but here only those most commonly used are summarized. Each synthesis method is detailed to enlighten the advantages and drawbacks.

2.3.1 Co-precipitation Method

Co-precipitation is the most commonly used method to synthesize LDHs. It involves dissolving the inorganic salts in alkaline media, at constant or increasing pH. This reaction allows controlling the morphology and particle size, depending on the super-saturation of the solution. Co-precipitation is a powerful method for synthesizing LDHs with tunable structures by controlling several factors. This control is primarily achieved by adjusting the M^{II}/M^{III} mole ratios and the pH of the reaction medium. The type of interlayer anion can be influenced by the choice of precipitating agent, while synthesis duration and temperature can affect crystal size and morphology. Co-precipitation can be performed at low or high super-saturation conditions, depending on the desired crystallization state. In both cases, the initial concentration of the reactants has to be above the saturation state of the solution. The pH of the solution must be controlled because a too-low pH value does not allow the complete precipitation of all metallic ions, while a too-high value leads to the leaching of one or more metallic ions. Usually, basic media are preferred in most cases, but the optimal pH depends mainly on the metal cations (Chaillot *et al*., 2021).

Co-precipitation synthesis can be considered as an efficient method to obtain crystalline LDHs, particularly through a long synthesis duration time (several days), the controlled synthesis pH, and the addition of post treatments such as hydrothermal treatment. However, due to the large dimension of the obtained particles, the specific surface area values (between 50 and 100 $m^2\ g^{-1}$) are lower than those obtained by sol-gel synthesis (150–200 $m^2\ g^{-1}$) (Chaillot *et al*., 2021).

The advantage of the co-precipitation method is the possibility of controlling the charge density (Li *et al*., 2019; Sheng *et al*., 2019). LDHs obtained by co-precipitation at low super-saturation present a higher crystallinity than those obtained at high super-saturation conditions with the continuous regulation of the pH LDHs obtained by co-precipitation at low super-saturation present a higher crystallinity than those obtained at high super-saturation conditions with continuous regulation of the pH because of a small excess of alkali bicarbonates in the latter case, but gives rise to a high number of small aggregates due to the interlayer confinement effect of the carbonate ions (Solovov *et al*., 2018).

2.3.2 Sol-gel Method

This method was first explored by Lopez *et al*., 1996 for the preparation of (Mg-Al) LDH which showed high thermal stability and enhanced specific surface area (Forano *et al*., 2013). Thus, the sol–gel method is preferred for its low cost, fast reaction, for the possibility to obtain high purity LDHs, and for the possibility to tune their composition. This process allows controlling the structural properties of the final LDHs by simply varying the chemical nature of the reactants, the aging time and by removing/adding reactant species. This technique involves dissolving the desired metal sources (inorganic salts or metal-organic compounds) in water, at room temperature (Chaillot *et al*., 2021).

The concentration of the metal cations can be varied to tune the substitution ratio of M^{II} and M^{III} cations and to obtain a wide range of materials. The appropriate amount of acid or base is then added to the reactant solution during hydrolysis to favor the condensation reaction. The solution is finally aged for several hours or days, at room temperature or lightly heated up to 100 °C. A general sol-gel method was proposed for the preparation of LDHs that can be adapted to obtain materials containing specific metallic cations and possessing a defined morphology in view of a specific application. It also evidenced the formation of small

amounts of brucite phase, in addition to hydrotalcite, with a Mg/Al mole ratio of 2 and explained this behavior by the similar structure of the two materials. Synthetic hydrotalcite can also be calcined and rehydrated without losing their lamellar structure. During regeneration, they show a "memory effect," as reported by using rehydrated sol–gel hydrotalcite for different applications. Several parameters can be varied to improve the crystallinity of the particles, to modify their morphology, and to enhance the surface area. Parameters, such as the composition of the aqueous media, the pH, and the aging time, were considered (Chaillot *et al*., 2021).

The sol-gel synthesis method has the advantage of simplicity, high reproducibility, high homogeneity, getting LDHs with good crystallinity and purity, obtaining small-sized particles (nanoscale), and high specific surface area, cost efficiency, and suitability for the synthesis of different LDH compositions (Smalenskaite *et al*., 2017; Valeikiene *et al*., 2019; Valeikiene *et al*., 2020). This technique also limits the amounts of alkaline required and thus it is beneficial for industrial synthesis processes (Banerjee and Gautam, 2016).

2.3.3 Ion Exchange Method

LDHs can be also prepared by the ion exchange method. The method is useful when co-precipitation methods are inapplicable, especially when divalent/trivalent metal cations or the anions involved are unstable in alkaline solutions, or when the direct reaction between the metal ions and the guest anions is more favorable. In this method, guest anions are exchanged with host anions, the anions present in the interlayer regions of the LDHs, to produce new material, specific anion-pillared LDHs, with different chemical or physical properties. Ion exchange in layered metal hydroxides depends on the electrostatic interaction between the positively charged layers and the guest anions. Several factors have been reported to affect the extent of reaction in these layered materials: (i) affinity of guest anion, (ii) exchange medium, (iii) pH value and the chemical composition of the layers (Goh *et al*., 2008).

Anion exchange is the most effective technique to synthesize LDHs consisting of anions other than carbonates. LDHs have been synthesized containing variable anions, for example by exchange of NO_3^-. LDHs consisting of bulky organic or inorganic anions have been also

prepared. The order of intercalation is as follows: $CO_3^{2-} \gg SO_4^{2-} \gg OH^- \gg F^- \gg Cl^- \gg Br^- \gg NO_3^- \gg I^-$. The equation of anion exchange is shown as follows (Jamil *et al*., 2019):

$$M^{2+}_{1-x}M^{3+}_{x}(OH)_2A^{n-}_{x/n}.mH_2O + I^{n-} \longrightarrow M^{2+}_{1-x}M^{3+}_{x}(OH)_2I^{n-}_{x/n}.mH_2O + A^{n-};$$

I = Intercalated anion

2.3.4 Urea Hydrolysis

Urea is a highly soluble weak Brönsted base. It can be used as a precipitating agent instead of sodium hydroxide to increase the pH through its thermal decomposition. The slow decomposition, starting around 90 °C, leads to an increase of the pH up to 10. Since urea decomposes slowly, it leads to a lower degree of super-saturation. Moreover, prolonged hydrolysis results in the formation of CO_3^{2-} anions in basic medium which act as interlayer anions. Therefore, urea enables efficient pH control and the formation of mono-dispersed LDH materials with high crystallinity through a low-cost method. The purity and crystallinity of hydrotalcite phases can also be optimized by tuning the M^{II}:M^{III} mole ratio, the urea concentration, and the aging time. The main steps involved in hydrotalcite synthesis via urea hydrolysis are summarized in Figure 2 (Chaillot *et al*., 2021).

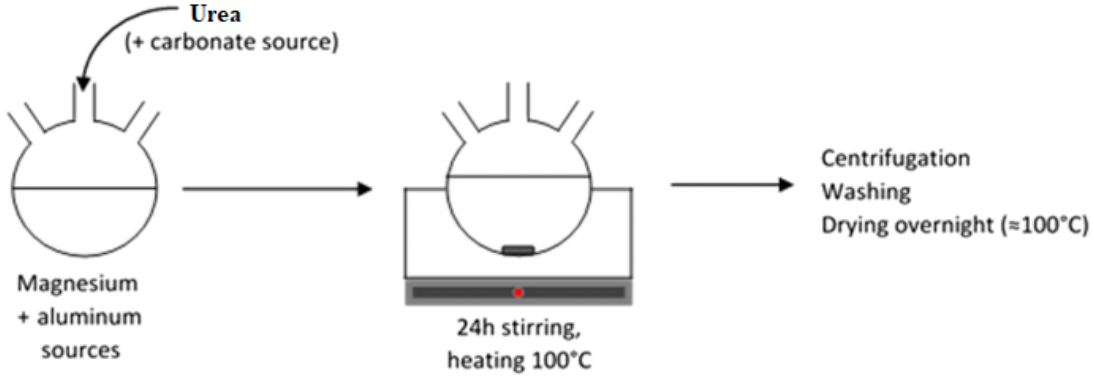

Figure 2. Scheme of the synthesis of hydrotalcite via urea hydrolysis (Chaillot *et al*., 2021).

As a partial conclusion, urea hydrolysis is a slow reaction that leads to a low degree of super-saturation during the precipitation. It presents the advantage of providing large and thin sheets with a narrow particle size distribution in a shorter aging time than co-precipitation. However, the decomposition of urea leads to the formation of CO_2 that reacts with water to form carbonates and acts as compensating anions. In such cases, a further anion exchange may be required depending on the targeted application (Chaillot *et al*., 2021; Naseem *et al*., 2019).

2.3.5 Hydrothermal Treatment

The synthesis of LDHs by co-precipitation, sol-gel method, or urea hydrolysis can be optimized by hydrothermal treatment to improve the crystallinity and the size of the crystallites. The treatment generally occurs under mild hydrothermal conditions, up to 200 °C, autogenous pressure, with duration between hours to several days (Chaillot *et al*., 2021).

Besides the improvement of crystallinity, hydrothermal synthesis can be directly used as a synthesis method, in order to form LDH phases with increased particle sizes. It involves dissolving the metallic salts into water, then putting the solution into a stainless-steel reactor and heating under hydrothermal conditions (30–300 °C) and steam pressure, with different synthesis times (a few hours to several days). Most commonly, metal oxides and hydroxides or nitrate salts are used as reactants, but other sources can also be used (Chaillot *et al*., 2021).

The advantages of using this synthesis process as an additional treatment are the higher LDH crystallinity, crystallite dimension, and purity of the samples. In general, a higher content of hydrotalcite is observed by increasing the preparation temperature and the time of the hydrothermal treatment. Unfortunately, the energy required to heat up the solution and the long synthesis time represent drawbacks for the industrial implementation of the hydrothermal treatment (Chaillot *et al*., 2021).

2.3.6 Reconstruction

Another common method to produce LDHs is rehydration/reconstruction using the structural ‘‘memory effect’’. This method involves the calcination of LDHs to remove the interlayer composition, resulting in mixed metal oxides and then exposing them to water and anions to regenerate the original layered structure. In addition, the anions included need not be the same species originally present in the interlayer of the uncalcined LDHs, and therefore this is an important method to synthesize LDHs with desired inorganic or organic anions to fulfill specific application requirements (Forano *et al*., 2013; Goh *et al*., 2008).

2.4 Modification Strategies of LDHs

Various chemical modifications of layered double hydroxides have been developed to fabricate LDH-based adsorbents with excellent sorption behaviors (Tian *et al*., 2017). To enhance the properties of LDHs, lots of variations have recently been introduced by researchers across the globe, such as Mg-Zn-Al-CO_3 LDH clay (Tabana *et al*., 2020), NiAlTi LDH (Rathee *et al*., 2020b), Ni/Fe/Ti LDH (Rathee *et al*., 2019), $Mg_{3-x}M_x/Al_1$ (M = Mn, Co, Ni, Cu, Zn) LDH (Valeikiene *et al*., 2019), ZnAl-LDH/$Al(OH)_3$ (Guo *et al*., 2018), Mn-doped MgAl-LDH (Li *et al*., 2019), Ternary Mg/(Al + Fe) LDHs (Das *et al*., 2018), NiCoTi, NiCoLa and MnNiAl-LDHs (Abasi *et al*., 2018), Ca-Fe/LDH-Cit (Rahmanian *et al*., 2018), etc.

2.4.1 Intercalation

LDHs can be intercalated with organic and inorganic anions due to their anion exchange properties to enhance their adsorption efficiency. The intercalation chemistry of LDH hosts has been used extensively for improving the adsorption capacity. In recent years LDHs have been successfully intercalated with halides, OH^-, CO_3^{2-}, NO_3^-, SO_4^{2-}, ClO_3^-, silicates, terephthalates, benzoates, citrate, malate, tartrate, chelating agents (such as chromotropic acid (CTA), ethylenediaminetetraacetate (EDTA), and nitrilotriacetate (NTA)) and polyoxometalates via ion exchange, co-precipitation, and reconstruction methods (Jiang *et al*., 2020; Tian *et al*., 2017).

2.4.2 Calcination

Calcination is a process in which LDHs are treated thermally at an optimum temperature to form the disturbed layer stacking. This process can be divided into four parts based on the various temperatures, such as dehydration, dehydroxylation, decomposition of anions, and oxide reformation, which can be expressed as:

$$\text{Dehydration}: M^{2+}_{1-x}M^{3+}_{x}(OH)_2\,A^{n-}_{x/n}.mH_2O \rightarrow M^{2+}_{1-x}M^{3+}_{x}(OH)_2\,A^{n-}_{x/n}(s) + mH_2O$$

$$\text{Dehydroxylation}: M^{2+}_{1-x}M^{3+}_{x}(OH)_2A^{n-}_{x/n}(s) \rightarrow M^{2+}_{1-x}M^{3+}_{x}O.A^{n-}_{x/n}(s) + H_2$$

$$\text{Decomposition of anion}: [M^{2+}_{1-x}M^{3+}_{x}O]^{x+}(A^{n-}_{x/n})(s) \rightarrow M^{2+}_{1-x}M^{3+}_{x}O_{1+x/2}\,(AO_y)$$

$$\text{Oxide reformation}: M_{1-x}^{2+}M_x^{3+}O_{1+x/2}(AO_y) \rightarrow M^{2+}O(s) + M^{2+}M^{3+}{}_2O_4 + AO_y$$

Where AO_y represents the species of decomposed anion (Jamil *et al*., 2019; Otgonjargal *et al*., 2017; Zou *et al*., 2016).

The calcination temperature of LDHs is determined by intercalated anionic species. The dehydroxylation of LDHs results in formation of mixed metal oxide (MMO) with high specific surface area, improved basic properties, fine crystallites and stability towards thermal treatments. For instance, the calcination of Mg-Al-LDH is extensively studied and resulted in MgO (Jamil *et al*., 2019).

In addition, the formed mixed metal oxides are mostly amorphous, with a high specific surface area and an ability to recover the original layered structure in contact with anions from aqueous solution. Therefore, the calcined LDHs have been widely used in water treatments in which they can remove anions, cations and organic matters; and in air purification by capturing GHGs due to their high affinity and efficiency, ease of operation, low cost, and potential for regeneration (Tian *et al*., 2017).

2.4.3 Reconstruction

LDHs possess a unique property called the "memory effect" which allows for their reconstruction after partial or complete deconstruction. This section explores reconstruction as a valuable technique for synthesizing LDHs with desired functionalities (Tian *et al*., 2017).

The initial step involves heating the LDHs at high temperatures. This process removes most of the interlayer anions (guest species residing between the LDH layers). The resulting material is a mixed metal oxide, retaining the basic layered structure of the original LDH. The calcined mixed metal oxide is then exposed to water and new guest anions. Remarkably, the LDH structure reforms incorporated these new anions within the interlayers. This ability to exchange interlayer anions makes reconstruction a powerful tool for tailoring LDH properties for specific applications (Chubar *et al*., 2017; Jamil *et al*., 2019).

2.4.4 Exfoliation

Delamination or exfoliation is a process in which layers of LDHs are peeled off into single or discrete sheets. As a result of the delamination process nanosheets of thickness 1~5 nm are obtained and it has remained a difficult task because of electrostatic interactions among layers (Figure 3) (Jamil *et al*., 2019).

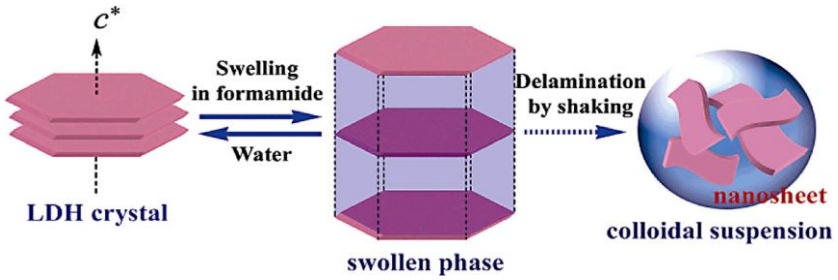

Figure 3. Schematic illustration of the possible delamination mechanism for LDHs in formamide (Daniel and Thomas, 2020).

2.4.5 Compositing

Combining LDHs with other materials leading to synergistic properties as a combined composite has also been explored. Many efforts have been made to enhance the dispersity (non-aggregation), regeneration, efficiency and stability of LDHs for their application in water treatment and air purification. The immobilization of LDHs on a suitable solid support could make the sorbent ease of operate in a dynamic system. In addition, the dissolution of LDHs can be avoided when alkaline stripping reagents are used for the recovery of the adsorbed analytes (Tian *et al*., 2017).

2.4.6 Substitutional Doping

Substitutional doping involves replacing a host atom in the crystal lattice with a foreign atom. The foreign atom occupies the same site in the lattice as the host atom, but it may have a different size or charge. This can change the lattice spacing and introduce defects, which can affect the material's electronic properties. LDHs/LDOs display attractive physical and chemical properties including effectual dispersion, large specific surface areas, and high anion exchange capacities that make them ideal adsorbents for many cations and anions. Generally, the substitution with other metallic cations, such as Fe, Zn, Cu, and Ni, adds the

possibility to modify the crystallite dimensions and influence the thermal stability of LDHs/LDOs. Various ternary LDHs/LDOs with combinations of diverse divalent and trivalent metal ions were reported (Chaillot *et al*., 2021; Das *et al*., 2018; Gevers *et al*., 2019).

2.5 The Role of LDHs and LDOs in Adsorption

Due to their structure, together with their compositional flexibility, LDHs possess highly versatile physicochemical properties leading to various applications of which environmental remediation is much explored, especially water treatment. Specific properties such as porosity and surface area can be tailored by varying the synthesis method, composition and conditions, leading to a wide range of materials adapted to targeted applications. The structure can also be modified by changing the combination of the cations and the interlayer anions, to confer specific properties (Chaillot *et al*., 2021; Pavel *et al*., 2020; Sheng *et al*., 2019; Sideris *et al*., 2008; Tian *et al*., 2017).

Adsorption is a process where gas or liquid molecules (adsorbates) accumulate on the surface of a solid or liquid (adsorbents). It's a surface phenomenon, meaning the molecules gather at the interface rather than penetrating deeper into the material. Sorption is a broader term encompassing both adsorption and absorption. Absorption involves the uptake of a substance (liquid or gas) throughout the volume of another substance (liquid or solid). So, while adsorption happens on the surface, absorption happens throughout the bulk material. Desorption is the opposite of adsorption. It's the process where the adsorbed molecules are released back from the surface of the adsorbent. This can happen due to changes in temperature, pressure, or the introduction of another gas/liquid (Chubar *et al*., 2017; Keller and Staudt, 2005).

Adsorption is one of the most promising technologies for fluoride removal. Adsorption offers several advantages for pollutant removal from water:
Versatility: Adsorption can effectively remove a wide range of pollutants, including organic and inorganic contaminants, heavy metals, and dyes, making it a versatile method for water treatment.
Efficiency: Adsorption processes typically achieve high removal efficiencies, especially for specific pollutants that may be challenging to remove using other methods.

Selectivity: Certain adsorbents can be tailored or selected to target specific pollutants, enhancing selectivity and minimizing interference with other substances present in the water.
Regenerability: Many adsorbents can be regenerated and reused multiple times, reducing operational costs and minimizing waste generation compared to single-use treatment methods.
Low energy requirements: Adsorption processes often require minimal energy input, making them cost-effective and environmentally friendly compared to energy-intensive treatment methods such as membrane filtration or chemical oxidation.
Scalability: Adsorption systems can be easily scaled up or down to meet varying water treatment needs, from small-scale household systems to large municipal or industrial facilities.
Ease of operation: Adsorption processes are generally straightforward to operate and maintain, requiring minimal operator training and supervision.
Compatibility with other treatment methods: Adsorption can be integrated with other water treatment processes, such as filtration or disinfection, to enhance overall treatment efficiency and effectiveness (Keller and Staudt, 2005).

Adsorption is a physicochemical process occurring at the interface between two phases. It is not expected to have this interface disappear due to the dissolution of the solid phase or allowing its full transformation during the adsorption process. In accordance with the definition of adsorption, root reconstruction processes of the solid phase are not expected to take place during the adsorption process. The preparation of an adsorbent is finalized before it is contacted with an adsorbate. It is expected that such a considerable change of the material structure/surface might be accompanied by chemical reactions taking place inside the purifying water solutions in parallel with the reconstruction of the layered structure, which might cause water contamination (Chubar *et al*., 2017).

In addition to the large surface area and high anion exchange capacity, the flexible interlayer region for various anionic and polar molecular species is another important feature of LDHs promising their high removal efficiencies of contaminants from wastewater. LDHs can remove inorganic contaminants such as mono-atomic anions (e.g., fluoride, chloride, bromide, and iodide) and oxyanions (e.g., arsenite, arsenate, chromate, phosphate, selenite, borate, and nitrate) and organic dyes (e.g., Remazol red 3BS, Evans blue, Chicago blue sky,

Niagara blue, etc.) from aqueous solutions based on adsorption and ion exchange (Ashekuzzaman and Jiang, 2014).

Besides, the adsorption site is crucial for the adsorption process. So far, various strategies have been adopted to increase the number of accessible adsorption sites such as regulating the particle size, composition and morphology of adsorbents via a top-down or bottom-up method. For example, LDH nanosheets with an average size of about 2.3 nm were prepared and reported (Zhao *et al*., 2018). Synthesized nano-size particles (7.8 nm) of LDH materials were also reported (Jiang *et al*., 2020; Tokudome *et al*., 2016).

2.5.1 Adsorption Mechanisms

Adsorption is a surface phenomenon, used for the accumulation of contaminants between two phases such as solid-liquid interface or solid-gas interface. Adsorption usually occurs due to intermolecular forces of attraction between adsorbent and adsorbate. When a solution having adsorbate encounters the adsorbent (porous media), surface forces at the interface concentrate the solutes on the surface of the adsorbent. Adsorption is considered to be a favorable process for wastewater treatment (Daud *et al*., 2019).

To realize the promising mechanisms involved in pollutant adsorption on LDHs and LDOs, studies such as FT-IR, XRD and SEM after the adsorption experiments have to be performed (Rahmanian *et al*., 2018). Different mechanisms have been suggested for the elimination of pollutants by these materials from wastewater, including physical adsorption (electrostatic attraction, van der Waals forces, hydrogen bonding, π–π interactions, etc.), hydroxide precipitation, ion exchange, complexation and chemical bonding, etc. (Daud *et al*., 2019; Mallakpour and Behranvand, 2020; Trana *et al*., 2019).

2.5.2 Adsorption Isotherm Studies

The experimentally observed adsorption isotherms can be classified according to IUPAC recommendations in six different types of I-VI (Figure 4). Type I isotherms can be described by the Langmuir Equation. They are characterized by a horizontal plateau, i.e. the asymptotic value of mass adsorbed approaches and maintains for even very high gas pressures. These isotherms are characteristic of micro-porous materials showing micro-pore filling but no

multilayer adsorption. Here the adsorption rate depends on the available micro-pore volume instead of the total interior surface area. Type II isotherms describe adsorption in mesoporous materials showing at low pressures monolayer, at higher pressures near saturation represents multilayer adsorption and pore condensation but no hysteresis. These isotherms can also be observed in dispersed, nonporous, or only macro-porous solids (pore diameter > 50 nm). They often can be described by the BET Equation or its generalizations. Type III isotherms occur in systems where the adsorbate-sorbent (a-s) interaction is small compared to the adsorbate-adsorbate (a-a) interaction, i.e. strongly associating molecules. Type IV isotherms describe the adsorption behavior of special meso-porous materials showing pore condensation together with hysteresis behavior between the adsorption and the desorption branch. Type V isotherms deviate from Type IV curves by nearly perpendicular middle portions of the adsorption and the desorption branches often near relative gas pressures $\frac{p}{p_s(T)} \cong 0.5$, indicating the existence of mesopores in which phase change like pore condensation may occur. Type VI isotherms present stepwise multilayer adsorbates in which the layers become more pronounced at low temperatures (Keller and Staudt, 2005; Ng *et al*., 2017).

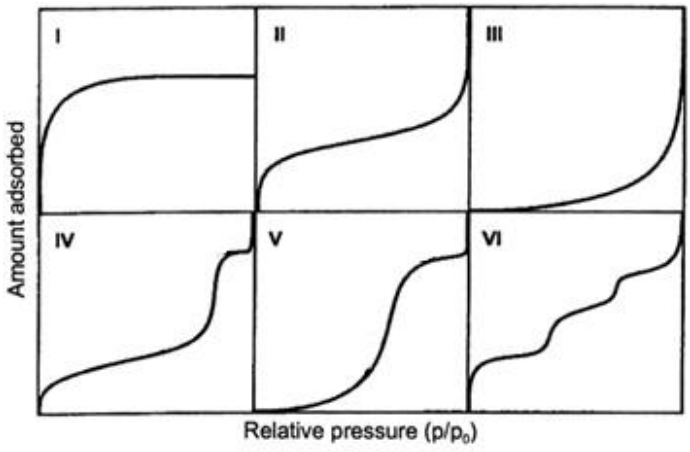

Figure 4. IUPAC classification of main types of gas physisorption isotherms (Keller and Staudt, 2005).

One of the important parameters to improve the properties of adsorbent is the adsorption isotherms for evaluation of the adsorption capacity and also its use in studying the behavior of adsorbent (Rahmanian *et al*., 2018). Adsorption isotherms, relate the amount of solute/adsorbate adsorbed (removed) and the concentration of pollutant/adsorbate remained in the solution at equilibrium condition. The isotherms are used to predict the adsorption uptake capacity. The adsorption performance specifically depends on the solution phases

(solid-liquid or solid-gas) and process variables such as solution pH, initial concentration and resident time (Daud *et al*., 2019).

The quantity of adsorbate removed by the adsorbents in aqueous solution and the percentage can be calculated using Equations (1) and (2):

$$q_e = \frac{C_o - C_e}{m} xV \quad (1)$$

$$q_e\% = \frac{C_o - C_e}{C_e} x100\% \quad (2)$$

where C_o and C_e are, respectively, the initial and equilibrium concentrations of adsorbate in solution (mg/L), q_e is the amount adsorbed at equilibrium, V is the volume of the solution (L) and m is the layered double hydroxide dosage (Kg) (Ayawei *et al*., 2015; Bo *et al*., 2016; Rahmanian *et al*., 2018).

In addition to adsorption capacity, adsorbate removal rate (R%) or adsorption efficiency is also calculated at the same time according to the following equation (Bo *et al*., 2016):

$$R\% = \frac{C_o - C_e}{C_o} x100\% \quad (3)$$

Langmuir and Freundlich isotherms are the most commonly used models and are applied to homogeneous and heterogeneous surfaces, respectively. Freundlich isotherm describes the relationship between the amount of gas or solute adsorbed onto a solid surface and the pressure (for gases) or concentration (for solutes) of the surrounding medium at a constant temperature. It's an empirical equation, meaning it's based on observations rather than a detailed theoretical model (Vigdorowitsch *et al*., 2021). Another isothermal model known as Sips isotherm is also used sometimes and is the combined form of Langmuir and Freundlich isotherms. The Sips model transforms into Langmuir and Freundlich isotherms at high and low concentrations of adsorbate respectively (Daud *et al*., 2019).

Adsorption isotherms are the route to get qualitative information of the adsorption capacity of adsorbents and the distribution of the adsorbates between liquid and solid phases after reaching equilibrium. Langmuir and Freundlich isotherm models are used to study the adsorption capacity of the adsorbent at different equilibrium concentrations. The linear representation of the Langmuir isotherm is

$$\frac{C_e}{q_e} = \frac{C_e}{q_m} + \frac{1}{q_m b} \quad (4)$$

where, C_e (mg/L) is the equilibrium concentration of the adsorbate, q_e (mg/Kg) is the equilibrium adsorption capacity of the adsorbent, q_m (mg/Kg) is the maximum adsorption capacity of the adsorbent and b (L/Kg) is the Langmuir constant. The linear plot of C_e/q_e versus C_e (Equation 4) gives the values of q_m, b and correlation coefficient (R^2) values. The correlation coefficient (R^2) values help to identify whether it is best fitted or not (Ayawei *et al*., 2015; Bo *et al*., 2016; Rahmanian *et al*., 2018; Rathee *et al*., 2019).

The information regarding the favorability of the adsorption is determined by the dimensionless constant separation factor or equilibrium parameter, S_f, which is given by the Equation,

$$S_f = \frac{1}{1 + bC_o} \quad (5)$$

where, b (L/mg) and C_o (mg/L) are the Langmuir adsorption constant and the initial adsorbate concentration, respectively. For an adsorption process to be favorable, the S_f value must lie between 0 and 1 ($0 < S_f < 1$). For an irreversible process, $S_f = 0$ and for an unfavorable process, $S_f > 1$ (Ayawei *et al*., 2015; Rahmanian *et al*., 2018; Rathee *et al*., 2019).

The linear form of the Freundlich adsorption isotherm is represented by

$$\log q_e = \frac{1}{n}\log C_e + \log k_f \quad (6)$$

where, k_f and n give the value of the Freundlich constants. The intercept and the slope of the linear plot of $\log q_e$ versus $\log C_e$ give the values of k_f and n, respectively and R^2. All the correlation coefficient (R^2) values are used to test whether the adsorption results are fitted the model or not. If the n values lie within 1 to 10, it indicates that the adsorption process is favorable one (Ayawei *et al*., 2015; Bo *et al*., 2016; Rahmanian *et al*., 2018; Rathee *et al*., 2019).

2.5.3 Adsorption Kinetics Studies

The adsorption kinetic study is important in predicting the mechanisms (chemical reaction or mass-transport process) that control the rate of the pollutant removal and retention time of adsorbed species at the solid-liquid interface (Ayawei *et al*., 2015).

Adsorption reactions can be understood with the aid of kinetic analysis, which can be utilized for the synthesis of efficient adsorbents. Chemical kinetics involves the study of reaction rates and reaction mechanisms by parameterizing as a function of temperature and concentration. The fundamental view of chemical kinetics is that reaction mechanisms cannot be solely proved from kinetic data alone; at best, one can only demonstrate that a given mechanism is consistent with the obtained kinetic data. The kinetic concepts are generalization of empirical knowledge about homogeneous reactions but, their application to the results from heterogeneous reactions should not be expected to be accurate. This is because of the factors that affect the diffusion of matter to and from a reaction site, the heterogeneous systems, are different from those in homogeneous systems. Again, the properties of the solid such as particle size and/or the possibility of phase transformations occurring during the reaction may affect the overall reaction mechanism (Machingauta, 2013).

Therefore, the experimental data has to be further subjected to some kinetic models. Three most commonly used models, namely the pseudo-first-order (PFO), pseudo-second-order (PSO), and the intraparticle diffusion models have to be fitted to the kinetic experimental data.

PFO model, $\log(q_e - q_t) = \log q_e - \frac{k_1}{2.303} t \; or \; \ln(q_e - q_t) = \ln q_e - k_1 t$ (7)

PSO model, $\frac{t}{q_t} = \frac{1}{k_2 q_e^{\,2}} + \frac{t}{q_e}$ (8)

Intraparticle diffusion model, $q_t = k_i t^{\frac{1}{2}} + c$ (9)

where, q_e (mg/g) and q_t (mg/g) are the adsorbed amount of adsorbate at equilibrium and at time (t), respectively; k_1 (min^{-1}), k_2 (g/mg min) and k_i (g/mg $min^{1/2}$) are the pseudo-first-order, pseudo-second-order and intraparticle diffusion rate constants, respectively and C is

the intercept (Ayawei *et al*., 2015; Bo *et al*., 2016; Daud *et al*., 2019; Rahmanian *et al*., 2018; Rathee *et al*., 2019).

2.5.4 Adsorption Thermodynamic Studies

Thermodynamic parameters such as enthalpy change (ΔH^o) and entropy change (ΔS^o) are obtained using the van't Hoff Equation (11). Whereas the Gibbs free energy of sorption ΔG^o, which is a fundamental criterion for spontaneity, is obtained from Equation (10).

$$\Delta G^\circ = -RT \ln K_d \tag{10}$$

$$\ln K_d = \frac{\Delta S^\circ}{R} - \frac{\Delta H^\circ}{RT} \tag{11}$$

where K_d equals the ratio of C_{solid} and C_{liquid}. C_{solid} is the equilibrium concentration of adsorbate on the adsorbent (mg/L), C_{liquid} is the equilibrium concentration of adsorbate in solution (mg/L), T is temperature (K) and R is the ideal gas constant (8.314 $J \cdot mol^{-1} \cdot K^{-1}$). K_d is the thermodynamic equilibrium constant that is estimated by plotting $\ln(q_e/C_e)$ vs q_e and extrapolating q_e to zero. The values of ΔS and ΔH were calculated from the intercept and the slope of the linear plot of $\ln K_d$ vs 1/T (Abasi *et al*., 2018; Ayawei *et al*., 2015; Ichou *et al*., 2020; Zubair *et al*., 2017).

Generally, the negative values of ΔG at any temperature indicate that the adsorption of adsorbate onto adsorbent/LDH/ is spontaneous and thermodynamically feasible. The negative value of ΔH suggests that the adsorption of adsorbate onto adsorbent is exothermic and consequently, decreases the adsorption capability with increasing temperature. This is in agreement with the increase in ΔG with increasing temperature. However, if the ΔH value is positive, it shows that the adsorption of adsorbate is endothermic and results in increase in adsorption capacity with increasing temperature. This may be attributed to the enlargement of pore size or activation of the adsorbent surface at higher temperatures. The negative values of ΔS indicate the greater order of reaction during the adsorption of adsorbate onto adsorbent. The positive values of ΔS demonstrate that randomness increases at the solid-solution interface during the adsorption of adsorbate onto LDH (Zubair *et al*., 2017).

2.5.5 Effects of Parameters on Adsorption Performance of LDH Materials

Several parameters can influence the adsorption performance of the LDH and LDO materials. These are detailed in the following.

2.5.5.1 pH of the solution

The initial pH of contaminated water is an important parameter for the efficient removal of pollutants using LDH materials as it significantly affects the chemistry and surface morphology of the LDHs which can be described as a surface charge of the LDHs and the ionic chemistry of a solution. LDH clays can neutralize hydrogen ions in solutions with low pH, while they get deprotonated in solutions with high pH (Daud *et al*., 2019; Tabana *et al*., 2020). The pH effect on the adsorption performance of LDHs is dependent on the types of adsorbate and the types of LDHs (Goh *et al*., 2008).

2.5.5.2 Temperature

Temperature is another physiochemical adsorption parameter that has a substantial effect on the adsorption performance. The temperature has two major effects on the adsorption process. Increasing the temperature is known to increase the rate of diffusion of the adsorbed molecules across the external boundary layer and the internal pores of the adsorbent particles, owing to the decrease in the viscosity of the solution. In addition, changing temperature will change the equilibrium capacity of the adsorbent for a particular adsorbate (Elhalil *et al*., 2016).

In an endothermic process, adsorption capacity increases by increasing the temperature because of the ease in mobility of adsorbate molecules and increased reactivity of the surface sites with temperature (Daud *et al*., 2019; Goh *et al*., 2008). On the other hand, for an exothermic process, the adsorption capacity has an inverse relation with operating temperature. This is because, by increasing temperature, the adsorptive forces between the adsorbate species and the active sites on the adsorbent surface reduce, consequently, the adsorption capacity decreases (Daud *et al*., 2019).

2.5.5.3 Adsorbent Dosage

Applying an optimum dosage of suitable adsorbent for adsorbate removal in a batch adsorption system is crucial for its cost-effective application (Goh *et al*., 2008).

2.5.5.4 Initial Concentration of Adsorbate

The initial concentration of adsorbate also influences the adsorption capacity of LDHs because of its relationship with available sites on the LDH surface. It was reported that generally, adsorbate (pollutant) removal has an inverse relation with the initial concentration. With an increase in initial concentration, the adsorption sites become saturated faster. Besides, by increasing the concentration, the adsorption capacity also increases because of the high driving forces available for mass transfer (Daud *et al*., 2019).

2.5.5.5 Contact Time

Contact time is an important factor to assess the favorability of the adsorption process. Generally, increasing the contact time of adsorption shows an increase in the removal of contaminants from aqueous solution until it reaches equilibrium (Zubair *et al*., 2017). To find an optimum time for the maximum removal of adsorbate, uptake studies were carried out at different time intervals using a fixed ratio (e.g. 1 g/L) of LDH in a fixed amount of sample solution (e.g. 100 mL). The time at which the maximum equilibrium uptake is attained will be recorded (Elhalil *et al*., 2016).

The short contact time to equilibrium saturation capacity is a key parameter for the application of LDH in the design of industrial-scale water treatment plants. The short contact time implies more treatment volume/batches can be processed in each time interval. Consequently, the size of the wastewater treatment plant can be reduced with the subsequent reduction in capital cost (Zubair *et al*., 2017).

2.5.5.6 Particle Size

Downsizing LDHs (i.e., lowering particle size or thickness of LDH layers) offers a significant opportunity to enhance a range of LDH properties that are attributed to factors

such as more coordinately unsaturated metal cations (i.e., defect-rich structures that serve as active centers), more available exposed active sites, larger specific surface area, and higher electronic conductivity than the bulk LDHs (Laipan *et al*., 2020; Sun *et al*., 2014; Zhao *et al*., 2015).

LDH particle sizes are particular characteristic to be investigated for adsorption on LDHs as it is indeed an important parameter in diffusion-controlled models. It was reported that decreasing the particle size of the LDHs has a dramatic effect on the adsorption rate but not on the adsorption capacity. The relatively higher adsorption rate with smaller adsorbent particles may be attributed to the fact that smaller particles yield large surface area and require shorter intra-particle diffusion time to reach sorption equilibrium (Goh *et al*., 2008).

2.5.5.7 Nature of Precursor Metals of LDHs

The nature of the LDH precursor metals, including different combinations of the metals, atomic ratio of the metals, metal–metal distance in the brucite-like sheet, etc., and the crystallinity of LDHs can significantly influence the adsorption of the guest adsorbate. The nature and the content of bivalent and trivalent metal ions in LDHs can also influence the adsorption efficiency of LDHs (Goh *et al*., 2008).

2.5.5.8 Charge Density

It is generally believed that the adsorption by LDHs can be enhanced by increasing the anion exchange capacity of the LDHs. This may be achieved by incorporating more trivalent cations or higher valent cations in the brucite-like sheet, which can subsequently increase its net positive charge in the brucite-like sheet (layer charge). The charge and species of the interlayer anion can also affect the adsorption of guest adsorbate. For this case, LDHs can be possibly synthesized containing tetravalent cations (e.g., Zr^{4+}) (Goh *et al*., 2008).

2.5.6 Regeneration and Reuse of LDHs

Regeneration of adsorbents is the most difficult and expensive part of an adsorption technology which may account for more than 70% of the total operating and maintenance cost for an adsorption system. A successful desorption/regeneration process should restore

the adsorbent similar to its initial properties for effective reuse. Adsorbates can be recovered either for reuse or for proper disposal, depending on their market demand (Goh *et al*., 2008).

Various alkaline solutions and salt solutions or a mixture of these solutions have been used successfully to desorb adsorbate-loaded LDHs. Reusability and recycling of an adsorbent is an important aspect of the viability of the adsorption process. Calcined LDHs are capable of being regenerated due to a "memory effect". The spent LDHs can be completely decomposed upon re-calcination; hence the suspensions were recovered after completing equilibrium adsorption experiments and re-calcined at high temperature. Thermal regeneration of LDHs for re-use is only feasible over many cycles after which the LDHs lose their sorption capacity (Goh *et al*., 2008; Tabana *et al*., 2020).

2.6 LDHs and LDOs in Water Treatment

LDHs and LDOs effectively remove various pollutants from water, including heavy metals, organic dyes, inorganic anions and pharmaceuticals. Their positively charged layers selectively bind negatively charged contaminants, while the interlayer anions can be tailored for specific targets. Examples include Fe–Al–Ce tri-metal oxide for fluoride adsorption (Wu *et al*., 2007), calcined Mg/Al LDH for defluoridation of groundwater (Elhalil *et al*., 2016), La-doped Li/Al LDHs for enhanced fluoride removal (Cai *et al*., 2018b), Mg-Al LDHs for phosphate removal (Benhiti *et al*., 2020) and Co-Al LDH for efficient removal of methylene blue and methyl orange from water (Nazir *et al*., 2020).

The versatility and effectiveness of LDHs/LDOs make them promising candidates for various water treatment applications. As research in this field continues, further advancements can be expected in optimizing these materials for even broader and more efficient water treatment solutions (Wang *et al*., 2023).

2.7 LDHs and LDOs in Air Purification

LDHs and their derived LDOs are emerging as a class of promising materials for air purification due to their unique properties and tunability. LDHs can capture harmful gases like CO_2, NO_2, SO_2 and VOCs from polluted air. Their tunable pore size and surface chemistry enable selective adsorption of specific gas molecules. For instance, exfoliated Ni-

Al LDH has shown promising results in CO_2 capture from flue gases (Hanif *et al*., 2019), again Mg-Al, Mg-Fe, and Mg-Mn LDHs also showed good performance in CO_2 adsorption (Santamaría *et al*., 2023).

LDHs and LDOs hold immense potential for addressing various air pollution concerns. Their tunability, efficient pollutant capture abilities, and potential for regeneration make them promising candidates for developing sustainable and effective air purification technologies (Santamaría *et al*., 2023). With further research and development, LDHs and LDOs can play a significant role in creating cleaner air for a healthier future.

CHAPTER 3

MATERIALS AND METHODS

3.1 Chemicals and Materials

Various metal salts, including $NiCl_2.6H_2O$ (97%, LOBA CHEMIE Pvt. Ltd), $MnSO_4.H_2O$ (98%, SAMIR Tech-chem Pvt. Ltd), $Ce(NH_4)_2(NO_3)_6$ (0.1 M, INDETA Chemicals (India) Pvt. Ltd.), and $AlCl_3.6H_2O$ (98%, CDH(P) Ltd), were employed as starting materials for the synthesis of Ce^{4+} and Mn^{2+} substitutional doped Ni-Al LDHs. Aqueous fluoride solution was prepared from NaF (99.5%, Blulux, India). The mixture of NaOH (98%, LOBA CHEMIE Pvt. Ltd, India) and $NaHCO_3$ (97%, Merk) was used as a precipitating agent and as well as to control the pH during the synthesis process. Additionally, HCl (35%, Blulux, India) was utilized for pH adjustments. The stated chemicals were used without further purification. The flue gas mixture (87% N_2 and 13% CO_2) was used as simulated gas for CO_2 capture studies. Aalborg® DPC Digital Mass Flow Controllers was used to control the flow of CO_2 inlet and it also indicates the pressure and temperature. A CO_2 meter (VAISALA) with a CO_2 sensor/probe was used to record the online CO_2 concentrations. The acrylic glass tube of 12 cm in length and 11.19 mm in diameter and inert ceramic balls were used for packing the adsorbents.

3.2 Methods

3.2.1 Synthesis of $Ce^{4+}$and Mn^{2+}-Doped Ni-Al LDHs

In this study, pristine Ni-Al ($Ni_{0.075}Al_{0.025}(OH)_{0.2}(CO_3)_{0.0125}.yH_2O$), Mn^{2+}-doped Ni-Al ($Ni_{0.075-x}Mn_xAl_{0.025}(OH)_{0.2}(CO_3)_{0.0125}.yH_2O$, where x = 0.00375, 0.0075, and 0.015) and Ce^{4+}-doped Ni-Al ($Ni_{0.075}Al_{0.025-x}Ce_x(OH)_{0.2}(CO_3)_{(0.025+x)/2}.yH_2O$, where x = 0.00125, 0.0025, and 0.005) LDHs were synthesized via the co-precipitation method. This synthesis was done by modifying the method in Sokol *et al.* (2019a) and Velu *et al.* (1997), considering the mole ratio of divalent to trivalent (M^{2+}/M^{3+}) in pristine Ni-Al LDH to be 3:1. Initially, a solution denoted as "Sol A" was prepared by dissolving the predetermined amounts of the respective inorganic salts in 60 mL deionized water. A 17.827 g of $NiCl_2.6H_2O$ and 6.036 g

of $AlCl_3.6H_2O$ were used for pristine Ni-Al LDH. A 16.935 g of $NiCl_2.6H_2O$, 6.036 g of $AlCl_3.6H_2O$ and 0.634 g of $MnSO_4.H_2O$ for x=0.00375; 16.044 g of $NiCl_2.6H_2O$, 6.036 g of $AlCl_3.6H_2O$ and 1.268 g of $MnSO_4.H_2O$ for x=0.0075; and 14.261 g of $NiCl_2.6H_2O$, 6.036 g of $AlCl_3.6H_2O$ and 2.535 g $MnSO_4.H_2O$ for x=0.015 were used in Mn^{2+}-doped Ni-Al LDHs. A 17.827 g of $NiCl_2.6H_2O$, 5.735 g of $AlCl_3.6H_2O$ and 12.5 mL of 0.1 M $Ce(NH_4)_2(NO_3)_6$ for x=0.00125; 17.827 g of $NiCl_2.6H_2O$, 5.434 g of $AlCl_3.6H_2O$ and 25 mL of 0.1 M $Ce(NH_4)_2(NO_3)_6$ for x=0.0025; and 17.827 g of $NiCl_2.6H_2O$, 4.830 g of $AlCl_3.6H_2O$ and 50 mL of 0.1 M $Ce(NH_4)_2(NO_3)_6$ for x=0.005 were used in Ce^{4+} doped Ni-Al LDHs. Subsequently, a precipitating agent, a mixture of 2 M NaOH (20 g in 250 mL) and 1 M $NaHCO_3$ (21 g in 250 mL), designated as "Sol B," was also prepared. This precipitating agent was also used to maintain the pH. While maintaining a pH of 10 under vigorous stirring, "Sol B" was added dropwise to "Sol A." The resulting slurry was aged at 80 °C for 2 hours. The precipitate was then filtered, washed extensively to achieve near-neutral pH (7 ± 0.5), and dried at 110°C for 15 hours. Finally, the synthesized LDHs were ground and stored at room temperature for further characterization and applications. The synthesized samples were coded as NAH (for pristine), CNAH-0.05, CNAH-0.1 and CNAH-0.2 (for Ce^{4+}-doped) and MNAH-0.05, MNAH-0.1, and MNAH-0.2 (for Mn^{2+}-doped).

3.2.2 Synthesis of Ce^{4+}- and Mn^{2+}-Doped Ni-Al LDOs

Following the synthesis of Ce^{4+}- and Mn^{2+}-doped Ni-Al LDHs, LDOs were obtained through calcination according to Cavani *et al*. (1991). The optimal calcination temperature of the precursor LDHs was determined using TGA/DSC. Based on the analysis, all LDHs were calcined at 450 °C for 2 hours in a microwave muffle furnace. The resulting LDOs were designated according to their composition as NAO, CNAO-0.05, CNAO-0.1, CNAO-0.2, MNAO-0.05, MNAO-0.1, and MNAO-0.2. Finally, to obtain a uniform particle size distribution, the calcined LDOs were ground and sieved. This step ensures consistent material properties for subsequent characterization and performance evaluation.

3.2.3 Characterization of Ce^{4+}- and Mn^{2+}-Doped Ni-Al LDHs and LDOs

The synthesized LDHs and LDOs were characterized using various techniques. The surface morphology was examined using Scanning Electron Microscopy (SEM) with a TESCAN VEGA3 instrument and High-Resolution Transmission Electron Microscopy (HRTEM)

with JEOL JEM 2100 PLUS. Energy Dispersive X-ray Spectroscopy (EDS) was performed to analyze the elemental composition. Oxidation states of elements on the surface layer were determined by X-ray Photoelectron Spectroscopy (XPS) of Omicron ESCA made by Oxford Instrument, Germany. X-ray diffraction (XRD) patterns were obtained using an X-ray diffractometer (Rigaku Miniflex-600) with a copper K_α source (λ = 1.5406 Å), scanning over the 2θ range of 5 to 80 degrees at a constant scanning rate. Thermogravimetric analysis/differential scanning calorimetry (TGA/DSC) was used to explore the stability of the materials. Attenuated total reflection Fourier transform infrared (ATR FT-IR) spectra of the synthesized materials were recorded using a VERTEX70 spectrometer (BRUKER, Germany) over the range of 400 to 4000 cm^{-1} to identify the functional groups that were present in the materials.

3.2.4 Fluoride Adsorption Experiments

The study employed a one-parameter-at-a-time approach utilizing batch adsorption techniques to evaluate the influence of factors such as pH, temperature, agitation speed, dose, initial concentration and coexisting ions on the fluoride removal efficiency of CNAH and MNAH LDHs and LDOs. All batch adsorption studies were carried out in a thermostatic shaker. To facilitate the analysis, the synthesized materials were categorized into four groups: Ce^{4+}-doped Ni-Al LDH, Ce^{4+}-doped Ni-Al LDO, Mn^{2+}-doped Ni-Al LDH and Mn^{2+}-doped Ni-Al LDO. Within each category, initial screening experiments identified the highest-performing LDH and LDO based on adsorption efficiency. This better-performing material was then used to study the factors influencing the adsorption efficiencies (Cai *et al*., 2018a; Dessalegne *et al*., 2016).

Adsorption experiments employed 40 mL of a fluoride ion solution prepared in Milli-Q water within polypropylene conical flasks from the stock solution. The stock solution of 500 ppm F^- was prepared by weighing 42 g NaF and dissolving with 500 mL Milli-Q water in polypropylene conical flask. The investigated factors included: contact time (15, 30, 45, 60, 90 and 120 min), solution pH (3, 5, 7, 9 and 11), adsorbent dose (0.25, 0.5, 0.75, 1.0 and 1.25 g/L), initial fluoride concentration (10, 20, 40 and 60 mg/L), agitation rate (50, 100, 200 and 250 rpm) solution temperature (25, 35, 45 and 55 °C) and co-existing ions (Cl^-, NO_3^- and SO_4^{2-}). The impact of each factor on fluoride removal efficiency was evaluated. Following each experiment, the solution was filtered through a 0.45 µm nylon syringe filter

for fluoride ion concentration determination using a potentiometer equipped with a fluoride ion selective electrode (ISE). ISE was calibrated against the known F^- concentrations of the standards prepared from the stock solution and a calibration curve was created. The F^- concentration in the unknown sample was determined using the calibration curve. Subsequently, the adsorption capacity (q_e) and removal efficiency (R) were calculated using the Equations 1 and 3, respectively (Dessalegne *et al*., 2016).

3.2.4.1 Adsorption Kinetics, Isotherm and Thermodynamic Modelling

The fluoride adsorption in aqueous solutions onto Mn^{2+} and Ce^{4+} doped Ni-Al LDHs were analyzed with some selected kinetics, isotherm and thermodynamic models, and their Equations are given in Table 1. In the evaluation of all these models, the CAVS adsorption evaluation software was used to identify the one that fits best.

Table 1. Kinetics, isotherm and thermodynamic models and their Equations (Ayawei *et al*., 2017; Dada *et al*., 2021; López-Luna *et al*., 2019).

Model types		Expressions	
Kinetic models	PFO	$q_t = q_e - e^{k_1 \times t}$	(12)
	PSO	$q_t = \frac{k_2 \times {q_e}^2 \times t}{1 + k_2 \times q_e \times t}$	(13)
Isotherm models	Langmuir	$q_e = \frac{K_L C_e}{1 + b_L C_e}$	(14)
	Freundlich	$q_e = K_F {C_e}^{a_F}$	(15)
	Temkin	$q_e = \frac{RT}{b_T}(\ln A_T C_e)$	(16)
Thermodynamics	Van't Hoff	$\ln(K_c) = \frac{\Delta S^o}{R} - \frac{\Delta H^o}{RT}$ $K_c = \frac{q_e}{c_e} and \Delta G^o = -RT \times \ln(K_c)$	(17)

3.2.5 CO_2 Adsorption Experimental Setup and Measurements

CO_2 adsorption experiments were carried out according to previously reported works (Mesfer *et al*., 2020; Raganati *et al*., 2019). CO_2 capture was studied in a packed-bed column reactor (Figure 5). The setup included a mass flow controller (0-500 mL/min) with pressure

and temperature indicators, an acrylic glass tube (11.19 mm diameter, 12 cm length), an online CO_2 meter (0-20 vol.%, 0.1% accuracy), and all necessary valves and connections. To facilitate analysis, the synthesized layered double oxides were categorized into two groups: Ce^{4+}-doped Ni-Al LDO and Mn^{2+}-doped Ni-Al LDO. Within each category, initial screening experiments identified the highest-performing LDO based on adsorption efficiency. This more efficient material was then subjected to further parameter optimization.

To investigate the adsorption of CO_2 onto LDOs, approximately 100, 200 and 300 mg of the material were placed in a column with inert ceramic balls. The ceramic balls were thoroughly pre-treated by washing them with de-ionized water and heating them at 150 °C for 4 hours before use. A gas mixture containing 13±1 vol.% CO_2 was passed through the column at a flow rate of 10, 20 and 40 mL/min, inlet pressure of 14.15±0.1 psi, temperature of 31±2 ^oC, and bed height of 5 and 10 cm. Blank experiments were conducted by running the column packing using ceramic balls only.

The column was flushed with N_2 gas before each CO_2 adsorption experiment to eliminate any previously present gas. A CO_2 analyzer was used to measure and record the outflow CO_2 amount. The outflow data were collected until the concentration of outflow was greater than 90% of the concentration of CO_2 inlet. This steady state condition is evident from the graph of CO_2 out vs. time displayed on the CO_2 analyzer. The collected data was then utilized to investigate the breakthrough curve and estimate the adsorption capacity of the adsorbents.

Due to the low flow rate and short bed height, the pressure drop across the adsorbent bed remained low. Thus, the flow rates at the inlet and exit of the column were presumed to be equal for each experimental condition, and the pressure across the bed remained constant. The breakthrough (q_b, at 10%), saturation (q_s, at 90%), and equilibrium (q_e, at 100%) capacities of the synthesized LDOs were determined using CO_2 mass balancing Equation (19) with necessary conversions (Bhatta *et al*., 2016; Tiwari *et al*., 2017).

$$q = \frac{Q}{m \times 22.4} \int_0^t (C_i - C_e) dt \qquad (18)$$

where q denotes the CO_2 adsorption capacity in mol/g, Q flow rate of gas in L/min, m mass of adsorbent in g, and t time in minutes. C_i and C_e are intake and effluent CO_2 amounts (percentage of volume).

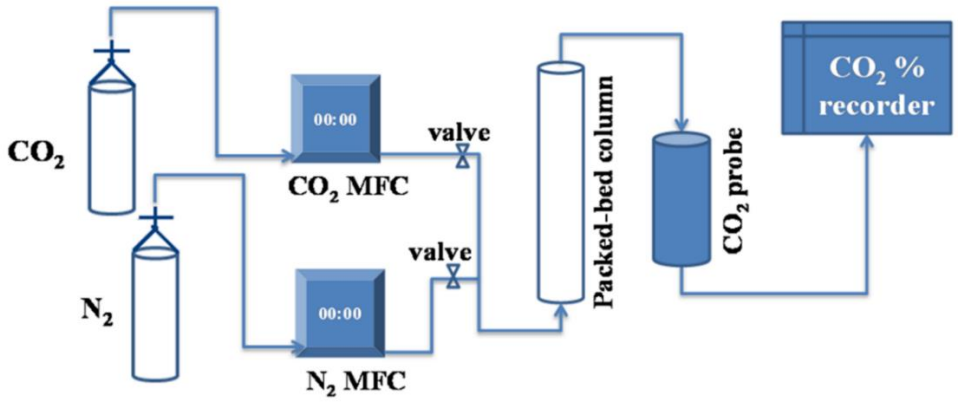

Figure 5. A design of in-lab-built packed-bed column experiment for CO_2 capture

3.2.5.1 Fixed-bed Adsorption Models

The Bohart-Adams, Clark, and Yoon-Nelson models are mathematical models that can be used to predict the breakthrough curve of a packed column adsorption process. The breakthrough curve is a plot of the effluent concentration of the adsorbate versus the time or volume of the effluent. The models are based on different assumptions and have different forms of Equations.

The Bohart-Adams model assumes that the rate of adsorption is proportional to the remaining adsorption capacity of the adsorbent and the concentration of the adsorbate in the liquid phase. The model also neglects the mass transfer resistance and axial dispersion in the column. The model can be expressed as Equation (19) (Hu *et al*., 2021; Özdemir and Onay, 2018):

$$\ln(\frac{C}{C_0}) = k_{BA}C_0t - k_{BA}N_0(1-e^{-k_{BA}t}) \quad (19)$$

where C is effluent concentration, C_0 is initial concentration, k_{BA} is Bohart-Adams rate constant, N_0 is initial adsorption capacity of the adsorbent, and t is time.

The Clark model describes the rate of adsorption as a function of the driving force, which is the difference between the equilibrium concentration and the actual concentration of the adsorbate on the adsorbent. The model also considers the mass transfer resistance and the axial dispersion in the column. It can be expressed by Equation (20) (Rafati *et al*., 2019):

$$\frac{dC}{dt} = -\frac{k_C A}{V_L}(C_e - C) + D_L \frac{d^2 C}{dz^2} \quad (20)$$

where k_C is the Clark rate constant, A is cross-sectional area of the column, V_L is the volume of liquid in the column, C_e is an equilibrium concentration, D_L is the axial dispersion coefficient, and z is the axial distance.

The Yoon-Nelson model assumes that the rate of adsorption is directly related to the probability of adsorption, which decreases linearly with time. The model also neglects mass transfer resistance and axial dispersion in the column. It can be expressed by Equation (21) (Özdemir and Onay, 2018):

$$\ln\left(\frac{C}{C_0 - C}\right) = k_{YN} t - \tau k_{YN} \quad (21)$$

where k_{YN} is the rate constant and τ is the time required for a 50% breakthrough.

These models can be used to fit experimental data and estimate the parameters of the models using linear or nonlinear regression methods. The models can also be used to predict the breakthrough time, adsorption capacity, and mass transfer coefficients of a fixed-bed adsorption process. Therefore, it is important to choose a suitable model for a specific system and validate it with experimental data.

CHAPTER 4

RESULTS AND DISCUSSION

This section included the characterizations of the synthesized LDHs and LDOs, studies of fluoride removal from aqueous solution by Ce^{4+} and Mn^{2+}-doped Ni-Al LDHs and LDOs, and CO_2 capture onto Ce^{4+} and Mn^{2+}-doped Ni-Al LDOs.

4.1 Characterizations of Mn^{2+} and Ce^{4+}-Doped Ni-Al LDHs

4.1.1 XRD Analysis

According to the XRD investigation depicted in Figure 6, the synthesized MNAHs and CNAHs exhibited distinct diffraction patterns at specific 2θ values. The observed peaks occurred at 11.47°, 23.12°, 34.94°, 39.22°, 61.0°, and 62.32°, are related to the (003), (006), (012), (015), (110), and (113) crystal planes, respectively in the LDHs. These planes are associated with the hydrotalcite-like structure of the LDHs, as per the JCPDS reference code 00-015-0087 (Gabrovska *et al*., 2016; George and Saravanakumar, 2018; Hanif *et al*., 2019; Jitianu *et al*., 2013).

As Mn^{2+} content increased in MNAHs (Figure 6), the intensity of diffraction peaks decreased, and the peaks broadened which led to decreased crystal size and crystallinity. This can be attributed to the slightly larger size of Mn^{2+} ions (0.83 Å) compared to Ni^{2+} ions (0.69 Å), causing distortions in the host layer. However, no significant shift in peak positions was observed (Liao, 2006; Żaba *et al*., 2021).

In contrast, Ce^{4+} doping in CNAHs (Figure 6) led to a more pronounced shift of diffraction peaks towards lower angles with increasing Ce^{4+} content. This indicates compressive strain in the lattice due to the significantly larger size of Ce^{4+} ions (0.87 Å) compared to Al^{3+} (0.39 Å). Additionally, Ce^{4+} doping also resulted in decreased peak intensity and the appearance of secondary phases (between 25^o and 30^o) at higher Ce^{4+} concentrations, further highlighting the impact of Ce^{4+} doping on the crystal structure and crystallite size (Liao, 2006; Velu *et al*., 1997).

The a and c lattice parameters of the hexagonal crystal structure of the synthesized LDHs can be expressed as in Equation (22) (Benhiti *et al*., 2020):

$$\frac{1}{d^2}=\frac{4}{3}\left(\frac{h^2+hk+k^2}{a^2}\right)+\frac{l^2}{c^2} \quad (22)$$

where d represents the lattice spacing between two planes; h, k, and l are representing the Miller indices of the planes. The cell parameters c and a of the synthesized LDHs were calculated from the d-spacing of the (003) and (110) planes, respectively. The c parameter represents the thickness of three layers plus the interlayer space between them and was usually three times the d_{003} parameter ($c=3d_{(003)}$). The lattice parameter, a, indicates an average distance between cations in the layer and was calculated from the (110) plane using $a = 2d_{(110)}$ and the results are presented in Table 2 (Ahmed *et al*., 2012; Benhiti *et al*., 2020; Evans and Slade, 2006; Sokol *et al*., 2019b). The lattice parameters, calculated from the XRD data, reflected the influence of doping. Cell parameters generally increased with Ce^{4+} doping, mirroring the larger size of Ce^{4+} ions. In contrast, Mn^{2+} doping had minimal effect on lattice parameters due to the smaller difference in ionic radii (Liao, 2006; Żaba *et al*., 2021).

Table 2. The crystallographic parameters of the MNAHs and CNAHs.

LDH Samples	Basal spacing, (d_{003}) Å	$d_{(110)}$ Å	Lattice parameters (Å)		Average crystallite size, (nm)
			a	c	
NAH	7.72	1.52	3.04	23.16	8.67
MNAH-0.05	7.71	1.5	3.0	23.13	5.16
MNAH-0.1	7.66	1.52	3.04	22.98	6.27
MNAH-0.2	7.67	1.5	3.0	23.01	4.13
CNAH-0.05	7.73	1.52	3.04	23.19	6.81
CNAH-0.1	7.94	1.52	3.04	23.82	8.15
CNAH-0.2	8.0	1.53	3.06	24.0	7.81

The average crystallite size of the synthesized LDHs was calculated from the full width at half-maximum (FWHM) of the diffraction peaks at the (003), (006), (012) and (110) planes. The Debye-Scherrer Equation was used to approximate the crystallite size of the synthesized LDHs from the major diffraction peaks using the Equation (Ali and Khan, 2017; Valeikiene *et al*., 2020):

$$D = \frac{K\lambda}{\beta \cos\theta} \tag{23}$$

where the average crystallite size, the wavelength of the X-ray radiation (Cu Kα = 0.15418 nm), the Scherrer constant 0.9, the FWHM, and the Bragg's diffraction angle are represented by D, λ, K, β and θ, respectively. The average crystallite size, estimated from the peak width, also varied depending on the dopant. NAH exhibited the largest crystal size, possibly due to more favorable interactions between Al and Ni ions (Table 2). Doping generally led to smaller crystallite sizes, with the extent of reduction depending on the type and amount of dopant (Liao, 2006; Żaba *et al*., 2021).

XRD analysis provided valuable insights into the structural changes induced by doping in Ni-Al LDHs. Both Mn^{2+} and Ce^{4+} doping affected the crystal structure, with Ce^{4+} having a more pronounced impact due to its larger ionic radius. These structural changes, including lattice strain, secondary phase formation, and altered crystallite size, could potentially influence the functional properties of LDHs, making them suitable for various applications. The lattice strain caused by doping results in defect-full material which can serve as active sites for adsorption. The decreased crystal size as a result of doping mostly leads to smaller particle size with a high surface area which enables the material to be an efficient adsorbent.

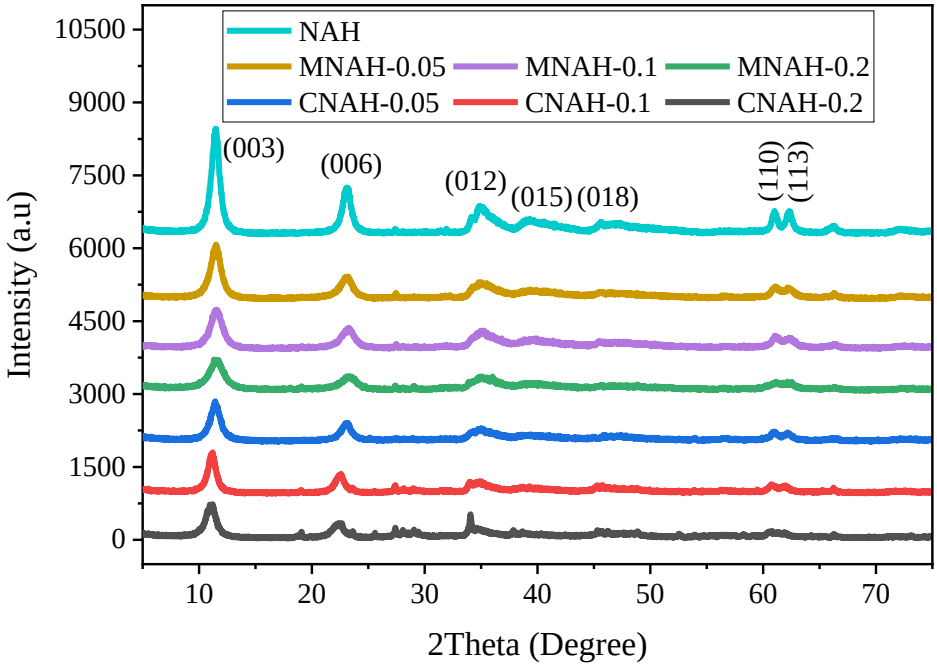

Figure 6. XRD patterns of MNAHs and CNAHs

4.1.2 ATR FT-IR Analysis

The FT-IR was also used to investigate the functional groups and nature of the bonds of MNAHs and CNAHs and their spectra are shown in Figure 7. A broad band at 3391 cm^{-1} indicated stretching vibrations of hydroxyl groups in metal hydroxides, interlayer water molecules and hydrogen bonding between them (dos Santos *et al*., 2013; Karami *et al*., 2019). A separate band at 1619 cm^{-1} suggested bending vibrations of water molecules. This band slightly shifted to a higher wavenumber in Mn^{2+} and Ce^{4+}-doped LDHs, suggesting interaction with these metal ions (Jabeen *et al*., 2017; Karami *et al*., 2019). A band at 1360 cm^{-1} is attributed to the carbonate anion within the layers (George and Saravanakumar, 2018; Jabeen *et al*., 2017; Karami *et al*., 2019; Lei *et al*., 2017). A unique peak at 1101 cm^{-1} arose from O-H bending coordinated to Mn^{2+} and shifted to a higher wavenumber with increasing Mn^{2+} content (Anandan *et al*., 2013; Falkowski *et al*., 2018). A band at 992 cm^{-1} indicated that Ce-O-Ce vibration was absent in the pristine material and shifted to around 1106 cm^{-1} with increasing Ce^{4+} content (Aponte *et al*., 2020). The low-frequency region (500-900 cm^{-1}) contains several peaks assigned to bending vibrations involving various metal-oxygen combinations (Al-O, Ni-O, Mn-O, Ce-O, mixed metal-oxygen) (dos Santos et al., 2013; Gao *et al*., 2022; Li *et al*., 2019). The position of the peak at 728 cm^{-1} changed depending on the dopant (higher wavenumber with Mn^{2+}, lower with Ce^{4+}), reflecting changes in their interactions with oxygen (George and Saravanakumar, 2018; Jabeen *et al*., 2017; Ouyang *et al*., 2021).

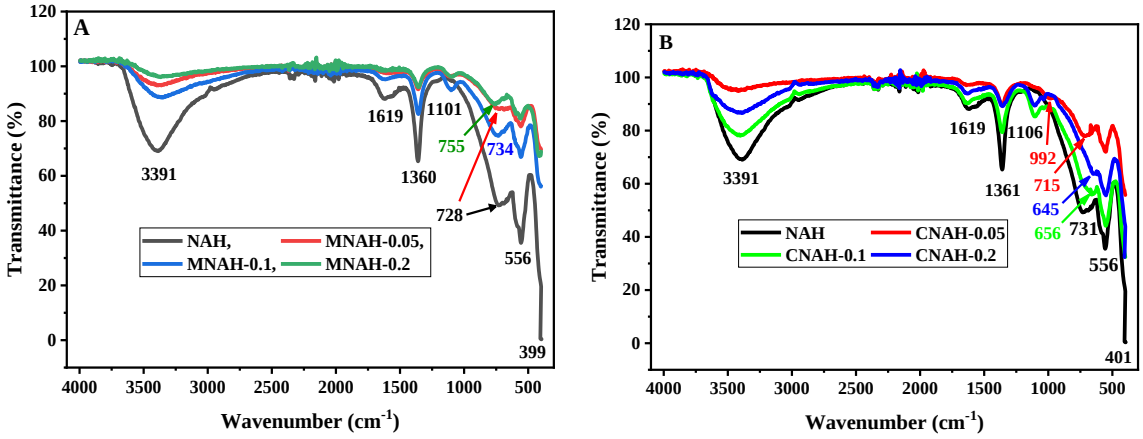

Figure 7. ATR FT-IR spectrum of the synthesized A) MNAHs and B) CNAHs

4.1.3 XPS Analysis

XPS was utilized to analyze the composition and electronic state of the constituents of the synthesized MNAH-0.1 and CNAH-0.05 LDHs. The XPS analysis of MNAH-1 (Figure 8A-F) showed the presence of Ni, Mn, Al, O, and C elements. The Ni 2p spectrum (Figure 8B) indicated the presence of Ni^{2+} ions having spin-orbital doublet peaks at the binding energy of 855.86 and 873.47 eV with a spin-energy separation of 17.6 eV (Lei *et al*., 2017; Ng and Hercules, 1976; Wang *et al*., 2019a). The Mn 2p spectrum (Figure 8C) confirmed that Mn^{2+} with two peaks at a binding energy of 641.58 and 653.37 eV (Tan *et al*., 1991; Wang *et al*., 2019a; Wang *et al*., 2019b). The Al 2p spectrum (Figure 8D) showed peaks corresponding to Al 2p3/2 and Al 2p1/2 at 68.42 eV and 74.08 eV, respectively, confirming the existence of Al^{3+} (Lei *et al*., 2017; Wang *et al*., 2019a). The C 1s spectrum (Figure 8E) indicated the presence of C-C, C–O, C=O, and carbonate species from deconvolution (George and Saravanakumar, 2018; Lei *et al*., 2017; Zhu *et al*., 2019). The O 1s spectrum (Figure 8F) confirmed the presence of O–H, O=C, and O–C by deconvolution (George and Saravanakumar, 2018; Zhu *et al*., 2019).

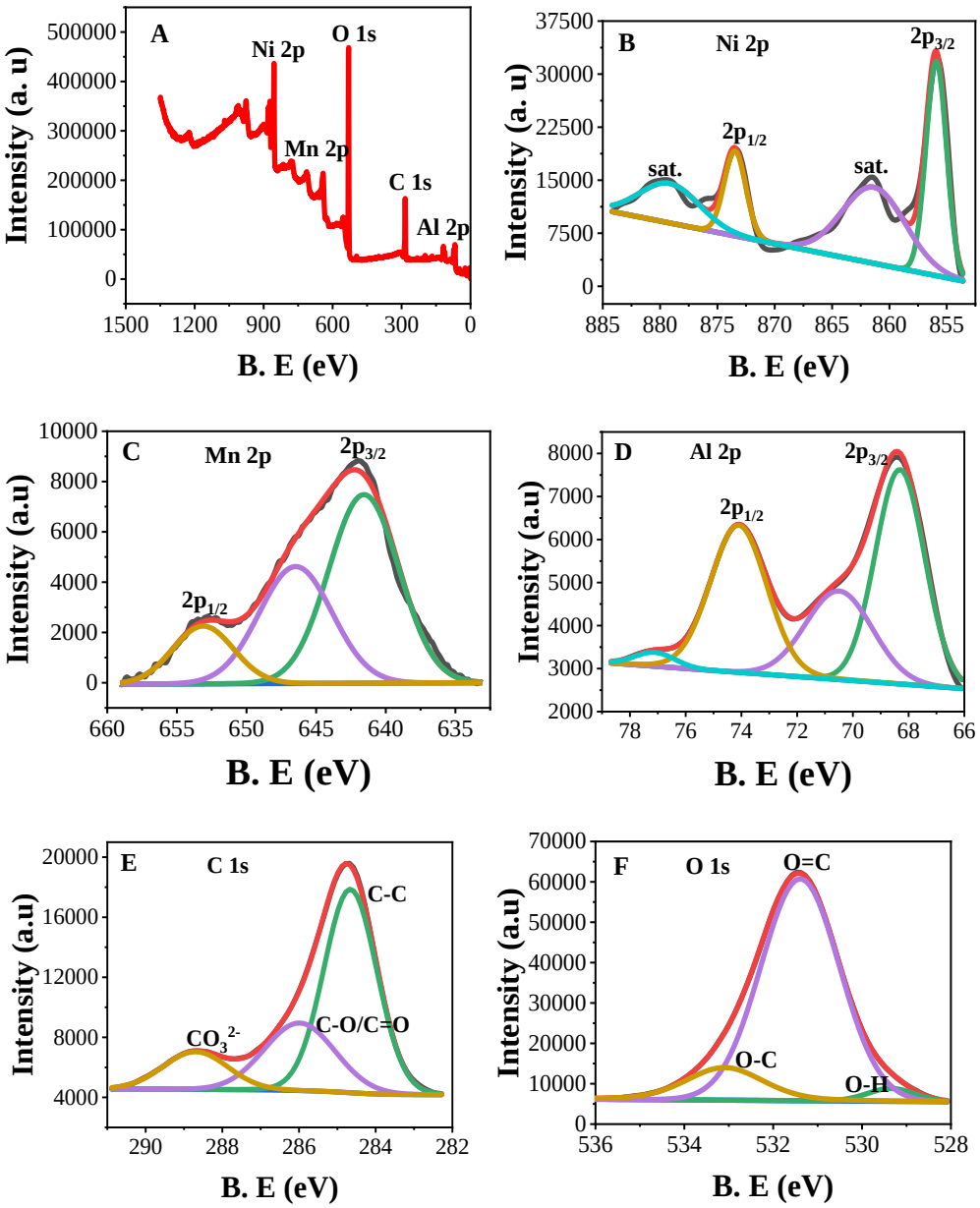

Figure 8. The XPS spectra of MNAH-0.1

The XPS analysis of CNA-0.05 (Figure 9) also showed the presence of Ni, Al, O, and C elements, as well as Ce. The Ni 2p spectrum (Figure 9B) confirmed the presence of Ni^{2+} ions. The Al 2p spectrum (Figure 9C) showed peaks corresponding to Al $2p_{3/2}$ and Al $2p_{1/2}$ indicating the existence of Al^{3+}. The Ce 3d spectrum (Figure 9D) spanning from 870 to 925 eV provided further evidence for the presence of Ce^{4+} ions in the LDH matrix (Gao *et al.*, 2021).

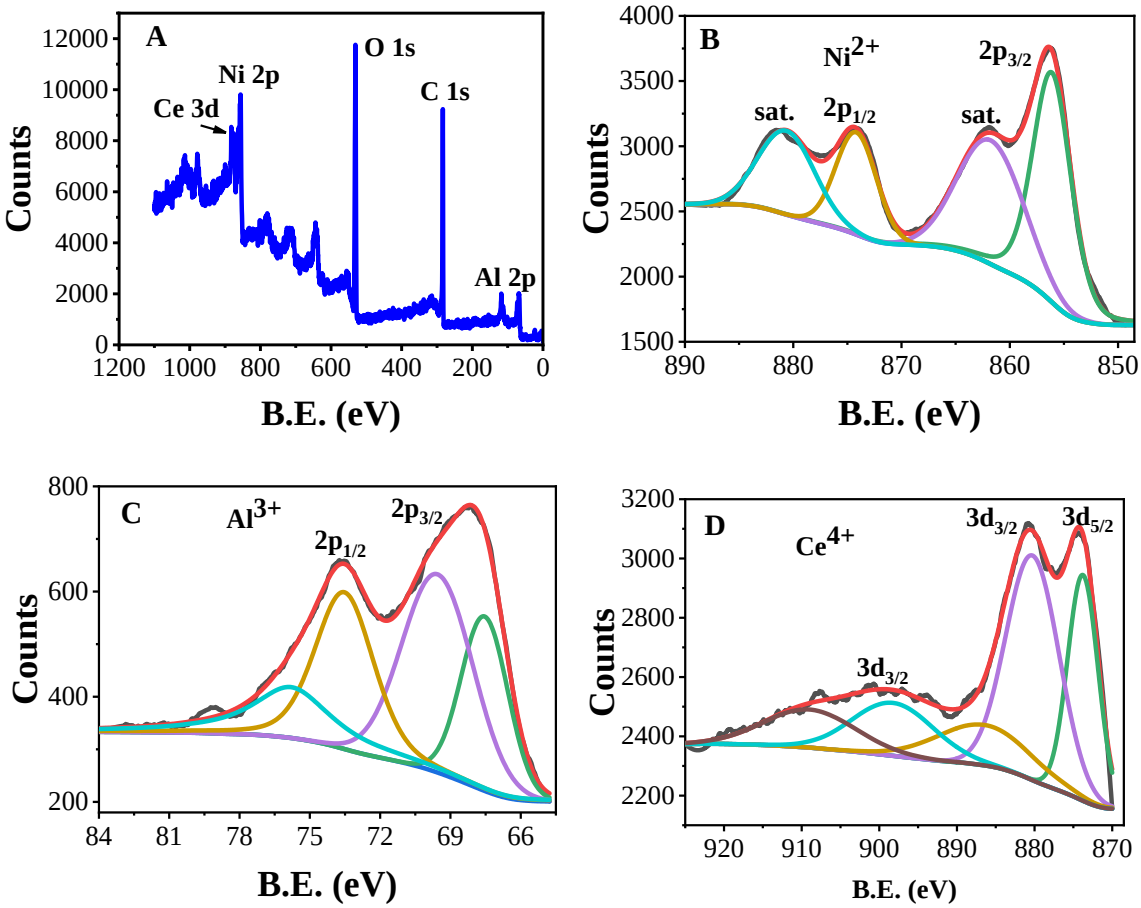

Figure 9. The XPS spectra of CNAH-0.05

4.1.4 EDS Analysis

The SEM-EDS and TEM-EDS mapping analyses were used to investigate the elemental distribution and composition of Mn^{2+} and Ce^{4+} doped Ni-Al LDHs, respectively. For both MNAH-0.1 and CNAH-0.05, the elemental mapping analysis which created a color-coded image showed a uniform distribution of all constituent elements, indicating a homogeneous dispersion throughout the LDH structure (Figure 10). The EDS analysis confirmed the intended elemental ratios for both materials. In MNAH-1, the mole ratio of divalent (Ni^{2+} + Mn^{2+}) to trivalent (Al^{3+}) was 3.4:1 close to the initial stoichiometric ratio of 3:1, and the mole ratio of Mn^{2+} to (Ni^{2+} + Mn^{2+}) was 0.097 close to the initial proportion of 0.1 (Figure 10E). In CNAH-0.05, the mole ratios of elements were close to the theoretical values, and the intended amount of Ce^{4+} was found (Figure 10F). These results confirmed the successful synthesis of the doped LDHs with the desired elemental compositions. This finding was further supported by the consistency with XPS results, solidifying the reliability of the

characterization methods employed. A similar EDS investigation was documented by (Lu *et al*., 2018) in which they also obtained the intended compositions.

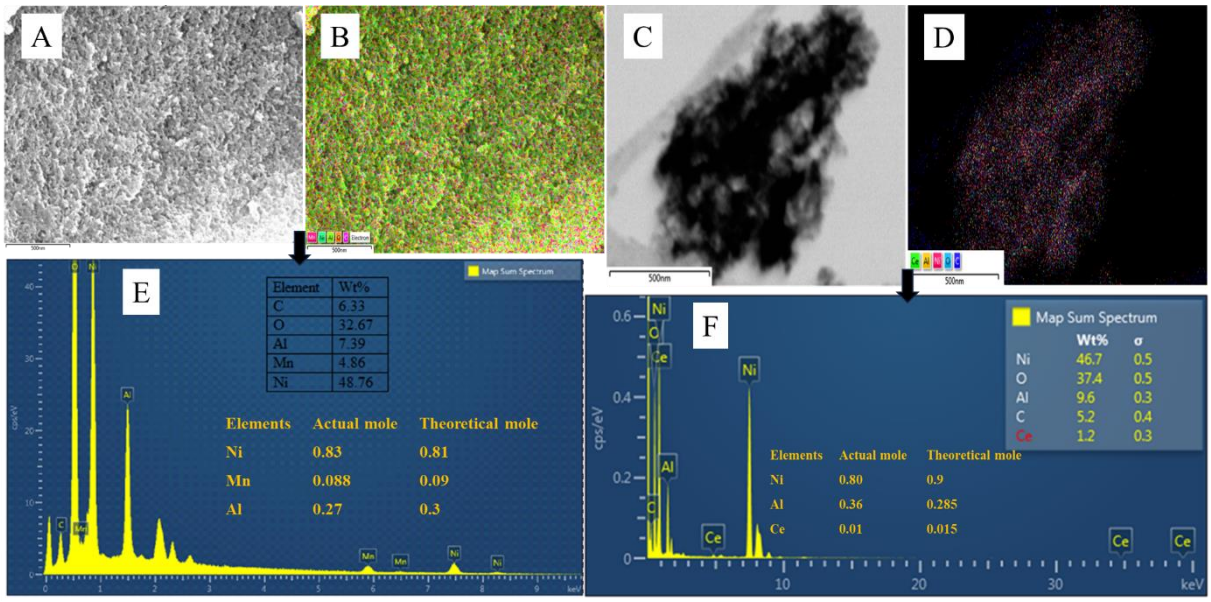

Figure 10. (A, B, E) SEM-EDS image, mapping and spectrum of the synthesized MNAH-0.1 LDH and (C, D, F) TEM-EDS image, mapping and spectrum of the synthesized CNAH-0.05

4.1.5 SEM Analysis

Figure 11 presented SEM micrographs of the synthesized LDHs: NAH, MNAH-0.05, MNAH-0.1, MNAH-0.2, CNAH-0.05, CNAH-0.1, and CNAH-0.2. The micrographs were obtained after sonicating the LDH samples in ethanol to form uniform colloidal suspensions. The micrographs revealed distinct morphologies for the synthesized LDHs. At first glance, the particles appear irregular. However, closer examination shows that these irregularities are agglomerations of tiny, sheet-like grains arranged in a layered fashion. Lu *et al*. (2018) and Xu *et al*. (2018) reported LDHs with similar morphological structures. The irregular particle shapes and layered structure point towards the crystalline nature of the LDHs. The layers are stacked on top of each other, with the sheet-like grains likely arising from the growth of individual layers during the co-precipitation process.

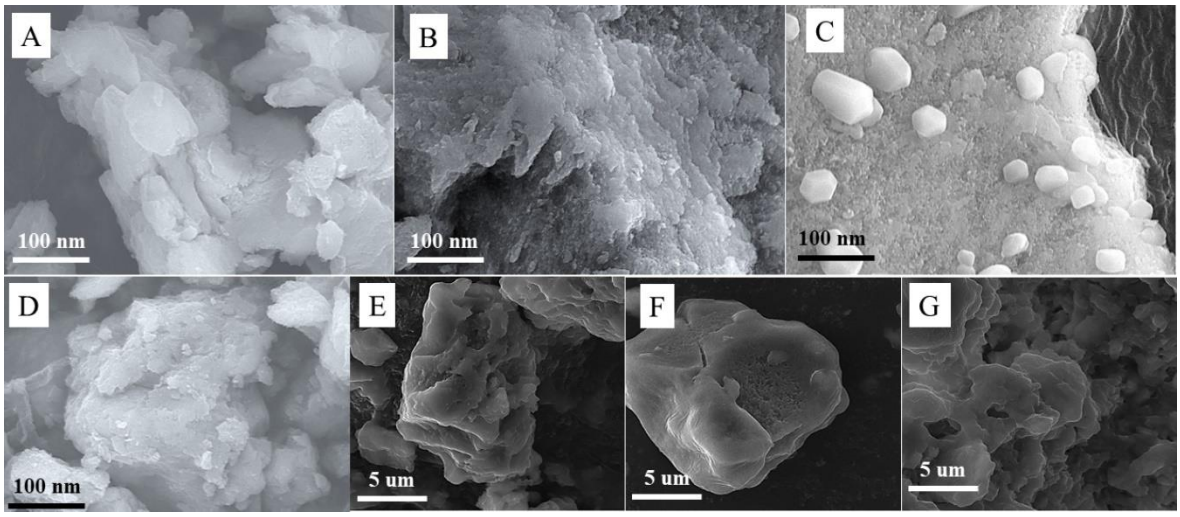

Figure 11. SEM micrographs of the synthesized A) NAH B) MNAH-0.05, C) MNAH-0.1, D) MNAH-0.2, E) CNAH-0.05, F) CNAH-0.1 and G) CNAH-0.2

4.1.6 HRTEM-SAED Analysis

The HRTEM images of the LDHs are shown in Figure 12. By investigating different regions of the TEM and HRTEM images of MNAH-0.1 (Figure 12A, B), it was observed to have a well-defined nano-sheet morphology with a characteristic stacked multilayer structure. Furthermore, the HRTEM results showed lattice fringes with the d-spacing of 0.786, 0.386 and 0.265 nm, corresponding to the (003), (006) and (012) planes (Figure 12C), respectively, confirming sheet-like particles with the hydrotalcite structure. The synthesized material has a 9.93 ± 3.71 nm average particle size. These findings aligned with similar previous LDH studies of Lu *et al*. (2018).

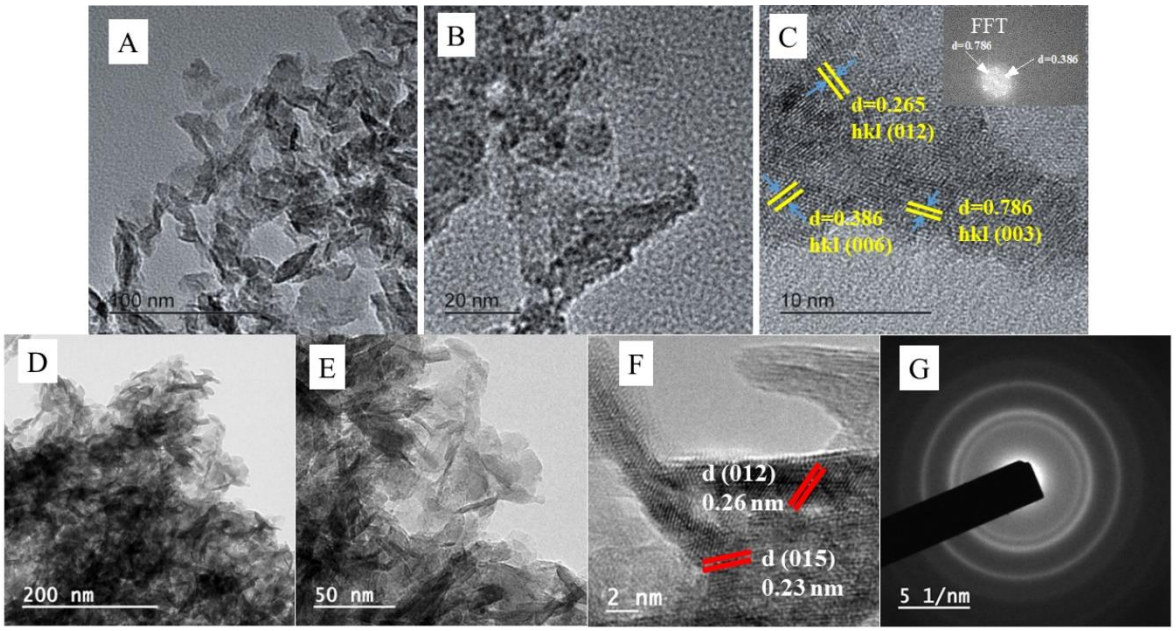

Figure 12. TEM images (A, B) and HRTEM images (C) of the synthesized MNAH-0.1 and TEM images (D, E), HRTEM images (F) and SAED pattern (G) of CNAH-0.05

Similar to the MNAH-0.1 case, HRTEM images revealed the presence of nanosheets in CNAH-0.05 (Figure 12D). These nanosheets exhibited formed aggregates of superimposed multilayer structures. The average size of these nanosheets is approximately 11.51 nm. Similar to MNAH-0.1, HRTEM analysis confirms the hydrotalcite structure of the CNAH-0.05 with lattice fringes corresponding to the (012) and (015) crystallographic planes (Figure 12F). The corresponding SAED pattern (Figure 12G) revealed the polycrystalline nature of the CNAH-0.05 nanosheets. This indicated the presence of multiple crystal domains within each nanosheets, adding further detail to the crystallographic structure. These findings aligned with the findings from XRD (Figure 6) and SEM (Figure 11) investigations and other previous studies (Li *et a*l., 2018; Lu *et al*., 2018; Wu *et al*., 2017).

4.1.7 TGA/DCS Analysis

The TGA/DSC analysis of MNAH-0.1 and CNAH-0.05 revealed decomposition behaviors at different stages (Figure 13). The MNAH-0.1 underwent three distinct stages of weight loss (totaling 39%). The initial minor loss (5%) around 163 °C was attributed to the removal of adsorbed or interlayer water, while the second stage at 250 °C (8% loss) likely involved dehydroxylation of the brucite-like metal hydroxide layers (Colonna et al., 2018). The major weight loss (26%) occurred at 343 °C was attributed to the decomposition of interlayer CO_3^{2-}

anions. Notably, no further weight change was observed above 450 °C, indicating the complete conversion of the LDH to LDO (Bhattacharyya, 2015; Karami *et al*., 2019; Klemkaite *et al*., 2011; Smalenskaite *et al*., 2017).

The CNAH-0.05 exhibited a similar decomposition pattern but with two main stages. The first stage around 175 °C (12.5% loss) was again attributed to water removal, while the second stage at 395 °C (18.5% loss) likely involved a combined process of dehydroxylation and interlayer carbonate decomposition (Colonna *et al*., 2018). Similar to the MNAH-0.1, the LDH structure of CNAH-0.05 decomposed above 500 °C, resulting in the formation of LDO (Bhattacharyya, 2015; Smalenskaite *et al*., 2017). Based on this TGA analysis, the intersection of the tangent line (drawn at the inflection point of final weight loss) and the horizontal stability line signified the temperature to be 450 °C where the material reached a stable state after decomposition. This was considered as the calcination temperature to convert LDHs to LDOs, as it represents the point where the conversion of LDHs to LDOs is likely completed. The synthesized LDHs were converted to LDOs at this temperature.

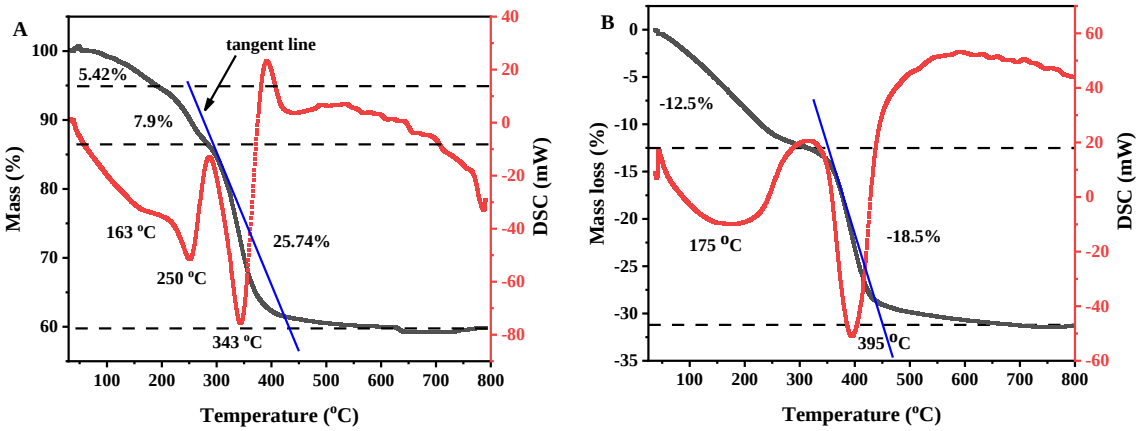

Figure 13. TGA/DSC curve of A) MNAH-0.1 and B) CNAH-0.05

4.1.8 BET Analysis

In this study, the 2D sheet-like MNAH-0.1 was investigated using the BET (Brunauer-Emmett-Teller) method to determine its textural characteristics. The results, presented in Table 3, revealed a significant improvement compared to the pristine Ni-Al LDH. MNAH-0.1 exhibited a higher specific surface area (52.06 m^2/g), pore volume (0.195 cm^3/g), and pore size (15.315 nm) compared to its undoped counterpart. This larger pore size indicates

the presence of micropores, which are particularly effective for capturing smaller molecules (Clark *et al*., 2019; Zhang *et al*., 2021).

Table 3. BET textural characteristics of MNAH-0.1 and CNAH-0.05.

Samples	Surface area (m^2 g^{-1})	Pore volume (cm^3 g^{-1})	Average pore size (nm)
NAH	45.11	0.125	13.24
MNAH-0.1	52.06	0.195	15.32
CNAH-0.05	110.55	0.253	8.15

The BET analysis was also performed of CNAH-0.05 sample. The results, again presented in Table 3, showcase a remarkable enhancement in textural properties compared to both the pristine and MNAH-0.1 samples. CNAH-0.05 showed a high specific surface area (110.547 m^2/g) and pore volume (0.253 cm^3/g), highlighting its potential for efficient adsorption. The average pore size is smaller in CNAH-0.05 (8.15 nm) compared to MNAH-0.1, indicating a more refined pore structure. This could potentially lead to improved mass transfer within the material, further enhancing its adsorption performance (Wang *et al*., 2014).

4.2 Characterizations of Mn^{2+} and Ce^{4+} -Doped Ni-Al LDOs

4.2.1 XRD Analysis

Calcination of LDHs resulted in the loss of interlayer anions and water molecules, transforming them into LDOs (Figure 14). This transformation was evident in the disappearance of LDH peaks in the XRD patterns (Figure 14). The XRD analysis (Figure 14) provided valuable insights into the crystallographic properties and phase composition of the synthesized Ce^{4+}- and Mn^{2+}-doped Ni-Al LDOs. The distinct diffraction peaks observed at specific 2θ corresponded to crystallographic planes (111), (200), and (220), confirming the well-defined crystalline nature of the LDOs. These peaks can be attributed to the dominant presence of NiO, as evidenced by their alignment with the reference pattern for NiO (JCPDS: 01-1239) (Ali *et al*., 2020; Lv *et al*., 2018). The dopants created significant changes in the XRD patterns when compared to the pristine. The broader and less intense peaks as a result of Mn^{2+} suggested that the doping process with Mn^{2+} disrupted the crystal structure of NiO. This led to the formation of smaller crystallites and a strained lattice. This

phenomenon can be explained by the larger ionic radii of Mn^{2+} compared to the host Ni^{2+} and Al^{3+} (do Nascimento *et al*., 2022). On the other hand, the XRD peaks of CNAO-0.05 are broader and less intense than NAO whereas, that of CNAO-0.1 and CNAO-0.2 became sharper and less intense with increasing Ce^{4+} content leading to increased crystallinity. With increasing Ce^{4+} content, distinct peaks associated with cerium oxide emerged at 29.0° corresponding to (110) (CPDS no. 34–0394) (do Nascimento *et al*., 2022), indicating the presence of a secondary crystalline phase (Lv et al., 2018). This phenomenon can also be the result of larger ionic radii of Ce^{4+} compared to the host Ni^{2+} and Al^{3+} (do Nascimento *et al*., 2022).

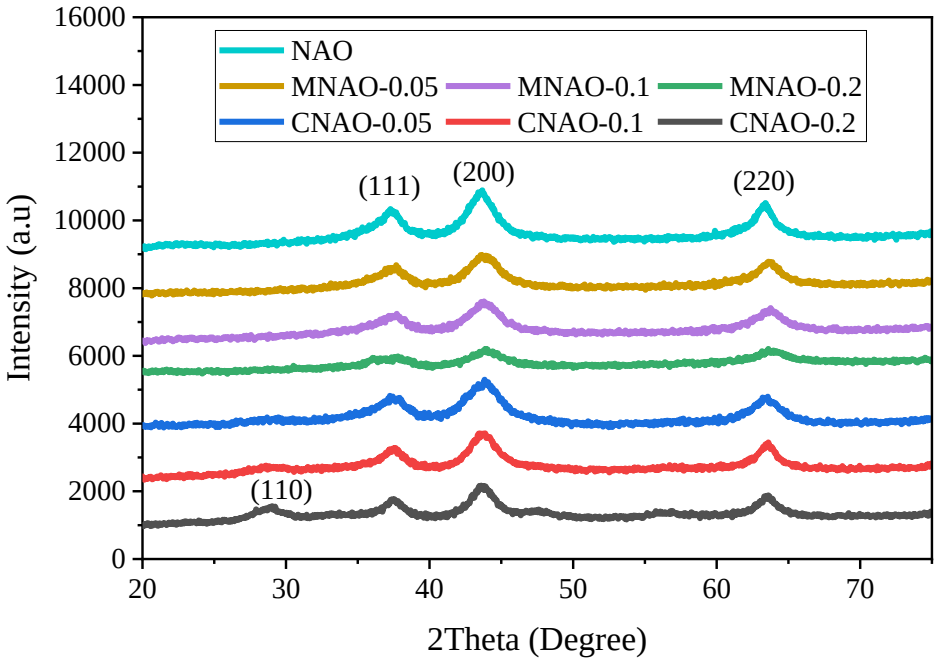

Figure 14. XRD patterns of MNAOs and CNAOs

Average lattice constants of the synthesized LDOs were determined using Equation (24) (Kedesdy and Drukalsky, 1954). The obtained results are depicted in Table 4.

$$a = d \times \sqrt{h^2 + k^2 + l^2} \qquad (24)$$

where a is the distance between atoms in the crystal, d is lattice spacing (inter-atomic spacing) and (hkl) is Miller indices.

The lattice constants, calculated from the prominent XRD peaks, confirmed the formation of LDOs. Notably, the values were lower than that of pure NiO, further solidifying the incorporation of Mn^{2+}, Al^{3+} and Ce^{4+} ions into the NiO lattice (Clause *et al*., 1992). This

finding aligned with the expected cubic crystal structure, characterized by alternating layers of metal cations and anions (Sato *et al*., 1988).

Table 4. Crystallographic properties of MNAOs and CNAOs

Materials	Lattice parameter (Å)	Average crystallite size (nm)
NAO	4.155	4.70
MNAO-0.05	4.139	3.68
MNAO-0.1	4.130	3.30
MNAO-0.2	4.129	2.68
CNAO-0.05	4.142	3.32
CNAO-0.1	4.147	4.63
CNAO-0.2	4.145	5.02

The average crystallite sizes, calculated using the Debye-Scherrer Equation, ranged from 2.68 nm to 5.02 nm across the different LDOs. While variations were observed, the differences were relatively small, suggesting that dopant introduction had a limited impact on overall crystallite size (Chatterjee, 2010). The lattice parameters of the LDOs measured in this study aligned with those previously reported in the literature (Pan *et al*., 2020).

In conclusion, the XRD analysis confirmed the successful synthesis of LDOs with the anticipated cubic crystal structure. It provided valuable details regarding crystallographic planes, lattice constants, and crystallite sizes. Notably, the incorporation of dopants with larger ionic radii influenced the XRD peak characteristics. The study revealed a general trend of smaller crystal sizes in LDOs compared to their LDH precursors as a result of calcination. This is confirmed by the BET surface area investigation (Table 5). LDOs showed greater surface area than their respective LDHs.

4.2.2 ATR FT-IR Analysis

The ATR-IR spectra of MNAOs and CNAOs revealed information about their chemical bonding and structural changes (Figure 15). The disappearance of the intensified ATR-IR peaks at 3391, 1619, and 1361 cm^{-1}, which were typically associated with LDHs functional

groups such as OH^-, H_2O and CO_3^{2-}, indicated the transformation of the LDH structure into the desired LDO structure upon calcination (dos Santos *et al*., 2013; Karami *et al*., 2019).

The presence of distinct absorption bands at around 1106 and 731 cm^{-1} confirmed the successful incorporation of Mn^{2+} into the LDO lattice, contributing to the formation of Mn-O bonds within the structure (Aponte *et al*., 2020). Peaks in the low-frequency region at 410 cm^{-1} were associated with metal-oxygen-metal and oxygen-metal-oxygen bending vibrational modes, further confirming the incorporation of Mn^{2+} and the formation of complex metal-oxygen networks within the MNAO structure (George and Saravanakumar, 2018; Jabeen *et al*., 2017; Ouyang *et al*., 2021).

ATR FT-IR peaks observed at 995, 1022, and 1119 cm^{-1} in CNAO-0.05, CNAO-0.1, and CNAO-0.2, respectively, provided clear evidence of the presence of Ce-O in the CNAOs (Aponte *et al*., 2020). An additional peak observed in CNAO-0.2 at 1042 cm^{-1} can be attributed to the presence of Ce-O-Ce in the structure. The shift towards higher wavenumbers with increasing Ce^{4+} concentration suggested the influence of Ce^{4+} on the vibrational behavior of the LDOs. This shift likely indicated the formation of stronger bonds between Ce^{4+} and surrounding oxygen atoms within the LDO framework (Aponte *et al*., 2020). The pronounced peak at 405 cm^{-1} signified the formation of LDOs involving Ni, Al, and Ce. The appearance of this peak suggested the presence of intricate interactions and bonding arrangements among these elements, leading to the creation of distinct LDOs (Clause *et al*., 1991; Jawad *et al*., 2019).

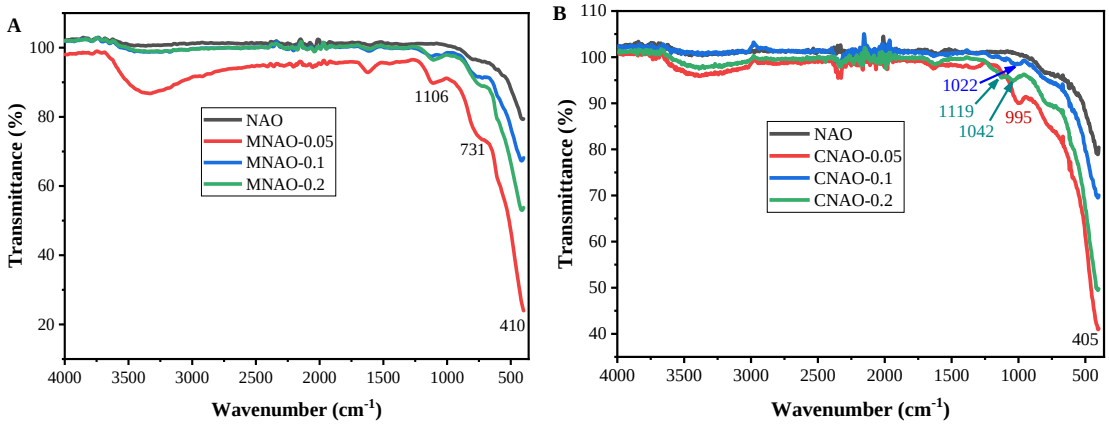

Figure 15. ATR FT-IR spectra of A) MNAOs and B) CNAOs

These findings suggested that the MNAOs and CNAOs have successfully been synthesized with the desired structures and compositions. The presence of Mn-O and Ce-O bonds in the MNAOs and CNAOs, respectively, were indicative of the successful incorporation of these dopants into the LDO structures. The formation of complex metal-oxygen networks in both MNAOs and CNAOs was expected to have important implications for their properties, such as adsorption, catalytic activity, electronic behavior, or structural stability (Jabeen *et al*., 2017).

4.2.3 XPS Analysis

The XPS analysis of MNAO-0.05 revealed the presence of peaks corresponding to Ni 2p, Mn 2p, Al 2p, and O 1s, with negligible contribution from carbon (C 1s), indicating the successful synthesis of the MNAO and absence of significant carbonaceous impurities (Figure 16A). Further analysis of the Ni 2p region confirmed the presence of Ni^{2+} at 855.12 eV ($2p_{3/2}$) and 873.09 eV ($2p_{1/2}$) binding energies (Li et al., 2017). The Mn 2p region displayed peaks characteristic of Mn^{2+} species at 641.35 eV ($2p_{3/2}$) and 651.71 eV ($2p_{1/2}$), confirming the successful incorporation of Mn^{2+} ions into the LDO lattice (Wang *et al*., 2019b). The Al 2p region exhibited peaks corresponding to Al^{3+} species at 67.2 eV ($2p_{3/2}$) and 73.54 eV ($2p_{1/2}$) (Lei *et al*., 2017), indicating the presence of Al in its trivalent state.

The XPS analysis of CNAO-0.05 revealed the presence of Ni 2p, Ce 3d, Al 2p and O 1s, indicating the successful incorporation of these elements into the LDO structure (Figure 16B). The negligible C 1s signal confirmed the removal of carbonate during the calcination of the precursor LDH. The Ni 2p spectra exhibited characteristic peaks indicative of the oxidation state Ni^{2+} at 855.25 eV ($2p_{3/2}$) and 873.12 eV ($2p_{1/2}$) (Li *et al*., 2018). The Ce 3d spectra showed peaks at 873.09 eV ($3d_{5/2}$) and 879.97 eV ($3d_{3/2}$), in line with a peak at 898.4 eV ($3d_{3/2}$). The presence of a single spin-orbit couplet with these binding energies suggested a dominant presence of Ce in the +4 oxidation state in the sample. These findings are consistent with the reported values for Ce(IV) in various materials (Gao *et al*., 2021). Furthermore, the Al 2p spectra displayed peaks consistent with the presence of Al^{3+} ions at 67.8 eV ($2p_{3/2}$) and 73.4 eV ($2p_{1/2}$) (Lei *et al*., 2017). XPS spectra of LDOs can share some similarities with their LDH precursors, particularly for the elements present in both types of materials such as Ni, Al, O, Mn and Ce.

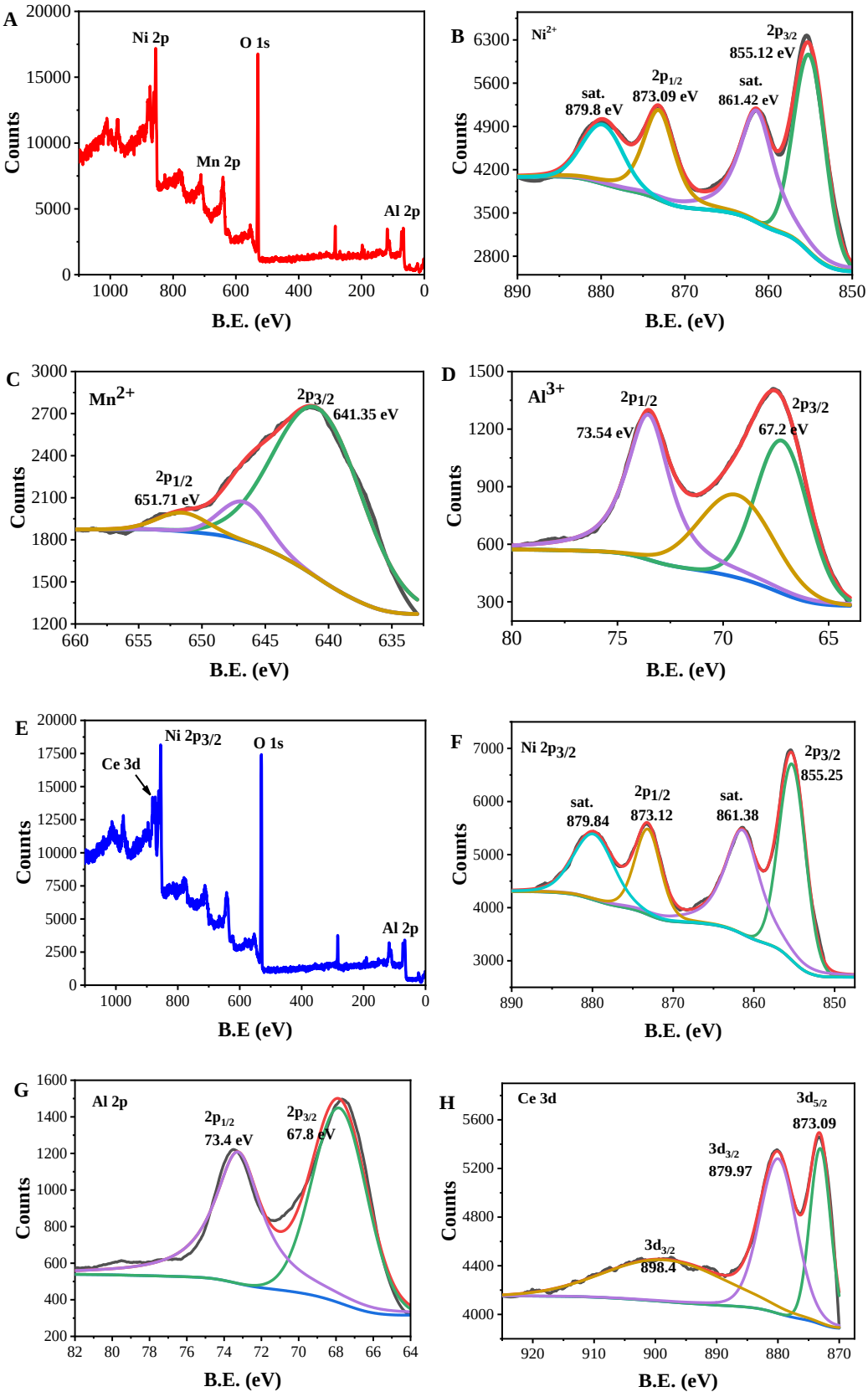

Figure 16. XPS spectra of elements existing in MNAO-0.05 and CNAO-0.05 with their characteristic binding energies

4.2.4 EDS Analysis

Figure 17 analyzes the elemental distribution in MNAO-0.05 and CNAO-0.05 using TEM, EDS mapping, and spectra. Both materials exhibited a uniform distribution of their constituent elements (Ni, Al, Mn, O for MNAO, and Ni, Al, Ce, O for CNAO). This confirmed the successful synthesis of these LDOs. The absence of carbon in both materials was attributed to the removal of the LDH interlayer anion during calcination, which was consistent with the XPS findings. EDS analysis further confirmed the intended composition of both MNAO and CNAO, including the successful incorporation of Mn^{2+} and Ce^{4+} into the Ni-Al LDO matrix. The mole ratio of (Ni^{2+} + Mn^{2+}) to Al^{3+} in MNAO-0.05 was 2.51, while $Ni^{2+}/Al^{3+}/Ce^{4+}$ in CNAO-0.05 was 0.97/0.37/0.01. The observed mole ratios of elements closely match the theoretical values, solidifying the conclusions drawn from the analyses. Overall, Figure 16 provided compelling evidence for the homogeneous elemental distribution and successful synthesis of MNAO and CNAO LDOs.

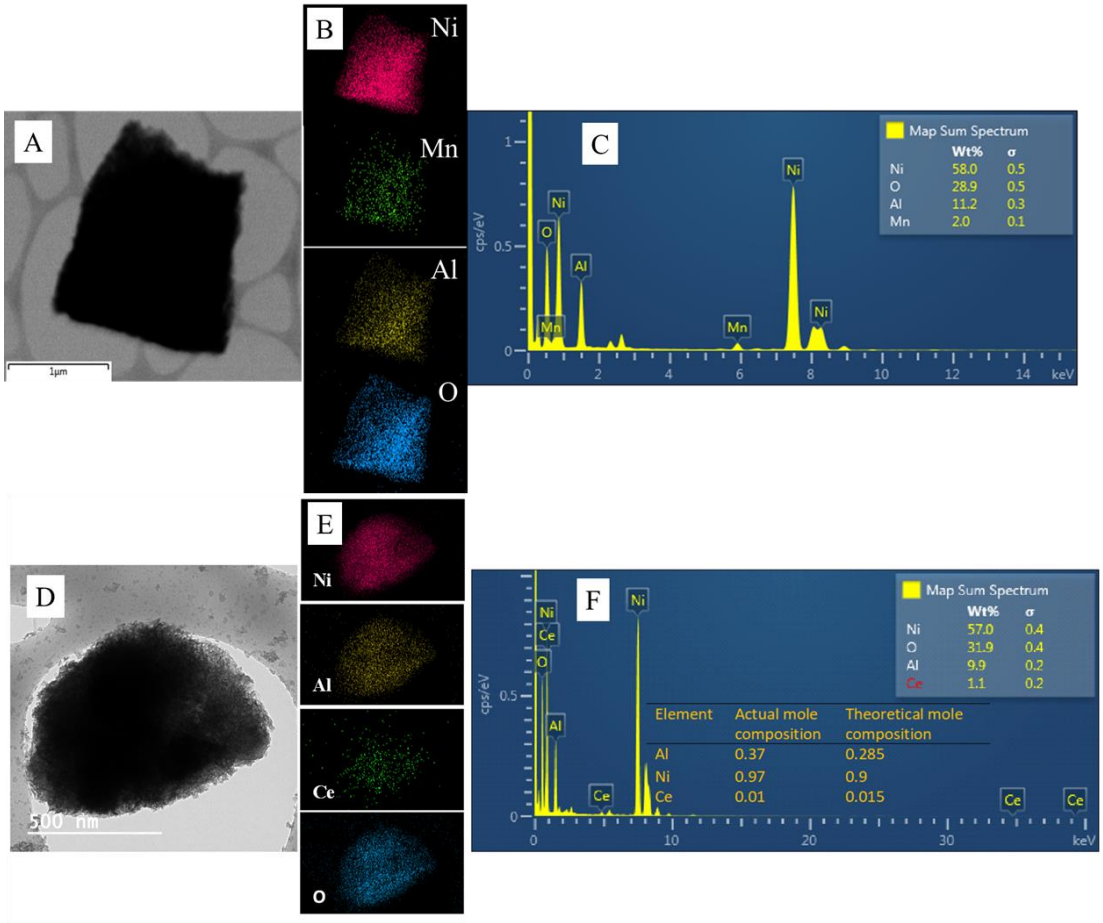

Figure 17. TEM image, EDS elemental mapping images and EDS spectra of MNAO-0.05 and CNAO-0.05

4.2.5 SEM Analysis

SEM analysis of the synthesized MNAO and CNAO materials (Figure 18) revealed attractive insights into their morphology. Both types of nanomaterials displayed agglomerated porous structures, characterized by interconnected voids and channels. These porous features played a crucial role in enhancing the adsorption capacity by providing a significantly larger surface area for interaction between the adsorbent and target molecules. Furthermore, both MNAOs and CNAOs exhibited unique, irregularly ordered sheet-like structures. These sheet-like structures might contribute to the overall stability of the adsorbents and can also facilitate the diffusion of fluoride ions and CO_2 molecules throughout the material. The irregular arrangement of these sheets further amplified the available surface area, ultimately leading to more efficient removal of fluoride and capture of CO_2. In essence, the distinctive morphology of both MNAO and CNAO adsorbents, characterized by interconnected pores and irregular sheet-like structures, played a key role in their enhanced adsorption capabilities. From the SEM analysis, it was observed that, after calcination, the sample maintained the morphology of the LDH precursor, although the calcination had led to considerable modifications in the surface area. Similar observations of sheet-like morphologies have been documented for Ni-Al LDHs and calcined LDOs (Rathee *et al*., 2020a).

This SEM morphological results obtained for LDOs were found to be similar to the LDH precursors previously described. The observed morphological similarities between the LDOs and their LDH precursors suggested that the basic structural features might be preserved during calcination. However, calcination can lead to alterations in pore size distribution, surface area, and crystallinity, potentially impacting the final adsorption performance.

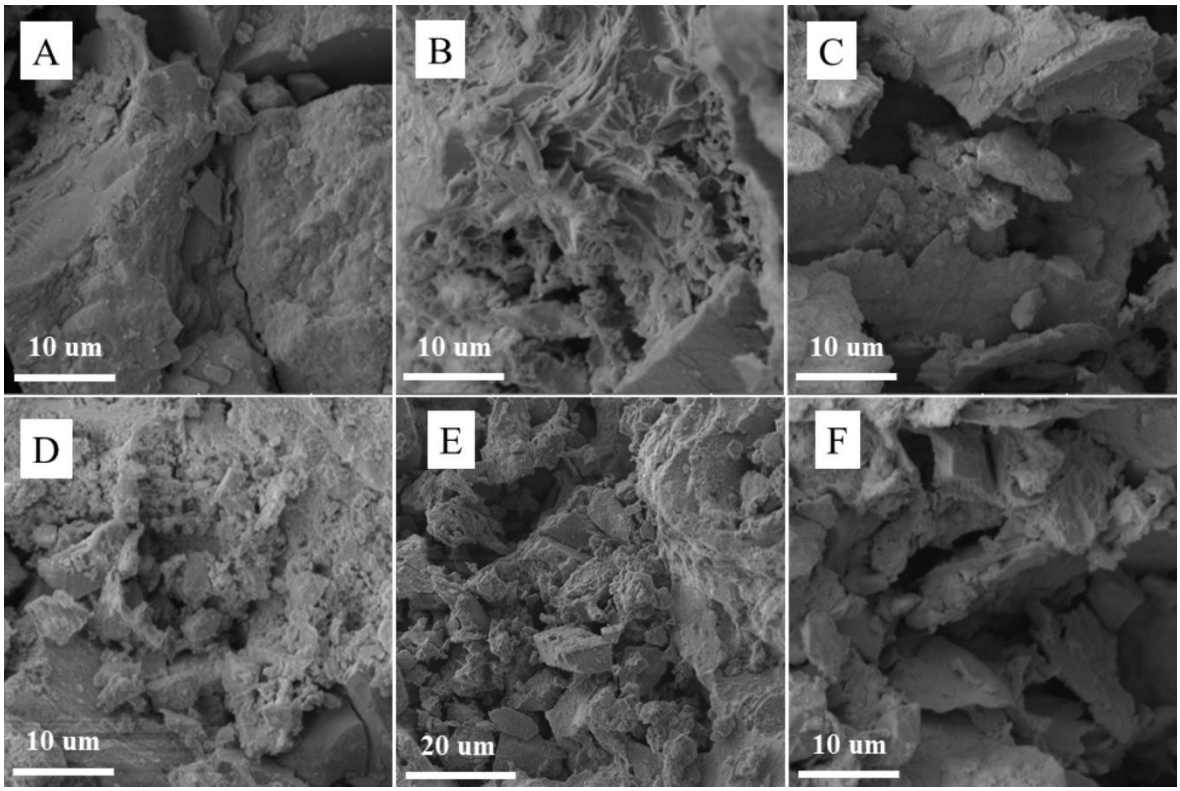

Figure 18. SEM images of the synthesized A) MNAO-0.05, B) MNAO-0.1, C) MNAO-0.2, D) CNAO-0.05, E) CNAO-0.1 and F) CNAO-0.2

4.2.6 HRTEM-SAED Analysis

Both MNAO-0.05 and CNAO-0.05, promising materials for adsorption, were investigated using HRTEM-SAED techniques to gain insights into their morphology and crystal structure (Figure 19). HRTEM analysis revealed distinct morphologies for each material. Both MNAO-0.05 and CNAO-0.05 exhibited sheet-like aggregates with an average size of 5.96 and 2.57 nm, respectively.

Moving beyond morphology, HRTEM and SAED measurements provided valuable information about the crystal structure of both materials. Both MNAO-0.05 and CNAO-0.05 displayed a well-defined crystalline structure, confirmed by consistent d-spacing values across the different techniques. These values, 0.23 and 0.21 nm, corresponded to the (111) and (200) crystallographic planes, respectively, further corroborated the findings from XRD analysis. This agreement reinforced the reliability of the employed characterization methods. (Rathee *et al*., 2020a) reported similar findings. Further analysis through SAED revealed an additional noteworthy feature in which both MNAO-0.05 and CNAO-0.05 exhibited a

polycrystalline nature, indicating the presence of multiple crystal orientations within their structures. This polycrystallinity might influence various material properties, including their potential for adsorption.

Overall, this microscopic exploration provided significant details about the morphology and crystal structure of both MNAO-0.05 and CNAO-0.05. While they exhibited distinct aggregate shapes and sizes, both share a well-defined crystalline structure and a polycrystalline nature. The remarkable agreement between the different characterization techniques strengthens the confidence in the obtained results. Considering the potential influence of these structural features on adsorption performance. This study revealed that LDOs with smaller particle sizes compared to their LDH precursors were obtained as a result of calcination although they have similar morphological structures.

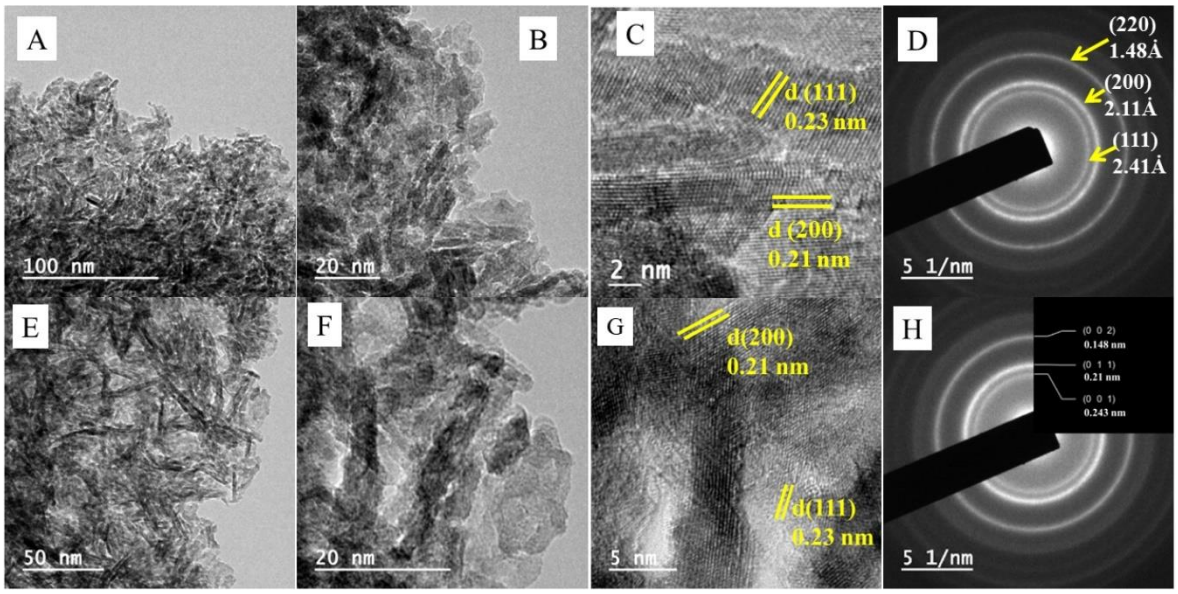

Figure 19. TEM images (A, B), HRTEM (C), SAED image (D) of MNAO-0.05 and TEM images (E, F), HRTEM (G), SAED image (H) of CNAO-0.05

4.2.7 BET Analysis

The textural properties of MNAO-0.2 and CNAO-0.2, specifically surface area, pore volume, and pore size, were significantly influenced by the introduction of dopant ions as revealed by BET analysis (Table 5).

Table 5. BET textural properties of MNAO-0.2 and CNAO-0.2

	NAO	MNAO-0.2	CNAO-0.2
Surface area (m^2/g)	130.77	148.59	189
Pore volume (cm^3/g)	0.296	0.206	0.210
Average pore size (nm)	4.52	2.77	2.63

Doping NAO with Mn^{2+} led to a notable increase in surface area, from 130.77 to 148.59 m^2/g. This enhancement was likely attributed to the incorporation of Mn^{2+} ions into the LDO structure, creating additional active sites and increasing surface roughness. However, the pore volume exhibited a slight decrease, from 0.296 to 0.206 cm^3/g. This suggested that the presence of Mn^{2+} ions might occupy some of the pore spaces or alter the arrangement of the layered structure, leading to a reduction in overall pore volume. Furthermore, the average pore size also decreased, dropping from 4.52 to 2.77 nm. This indicated the formation of smaller and more restricted pores, which could potentially hinder the diffusion of molecules and impact the adsorption properties of the material (Wang *et al*., 2014).

Like MNAO-0.2, Ce^{4+} doping in CNAO-0.2 increased surface area, from 130.77 to 189 m^2/g. This can be attributed to the introduction of Ce^{4+} ions, which might create more defects and vacancies in the crystal lattice, acting as nucleation sites for adsorption and consequently increasing the overall surface area (Kim *et al*., 2020). However, the pore volume followed the same trend as MNAO, decreasing from 0.296 to 0.21 cm^3/g. This again suggested that the dopant ions might be occupying pore spaces or influencing the structural arrangement, leading to a reduction in pore volume. The average pore size also displayed a similar decrease, shrinking from 4.52 to 2.63 nm. This potential reduction in pore size could have similar implications for diffusion and adsorption properties as observed in MNAO. In both MNAO and CNAO, the introduction of dopant ions significantly impacted their textural properties. While doping resulted in increased surface area, it also led to decreased pore volume and average pore size. Considerable differences between the surface area of the LDOs and the LDHs were observed as a result of calcination. These alterations in textural characteristics could potentially influence the materials' performance in various applications, such as catalysis and adsorption (Cavani *et al*., 1991).

4.3 Fluoride Adsorption onto Mn^{2+}-Doped Ni-Al LDHs

4.3.1 Investigation of Factors Affecting Fluoride Removal Efficiency

Dopant Amount: Here we studied the effect of Mn^{2+} dopant on the adsorption performance of fluoride from aqueous solution onto MNAH LDHs under the same conditions at 25 ºC, 45 min, pH 7, 0.25 g/L adsorbent, 40 mL 20 ppm F^- and 150 rpm. The results are displayed in Table 6. As indicated in Table 6, the adsorption capacity of fluoride onto NAH, MNAH-0.05, MNAH-0.1 and MNAH-0.2 were found to be 72.73, 75.25, 74.01 and 73.84 mg g^{-1}, respectively.

Table 6. Fluoride adsorption performance of MNAHs

Adsorbent	q_e, mg/g	R, %
NAH	72.73	90.91
MNAH-0.05	75.25	94.07
MNAH-0.1	74.01	92.52
MNAH-0.2	73.84	92.30

The amount of fluoride adsorption on MNAH-0.05 was higher than the others. Similarly, a high percentage of fluoride removal was obtained by this LDH. This might be due to the hydrotalcite properties of the material in which the layered structure was more pronounced at this dopant concentration as shown in the XRD results of LDHs in addition to the synergetic effect of the mixed hydroxides. Again, it might have a greater surface area than the others (Table 3). Therefore, MNAH-0.05 LDH was used to study the influence of other parameters such as pH, initial concentration, adsorbent amount, time and temperature on its adsorption performance.

Adsorbent amount: The influence of adsorbent mass on the adsorption efficiency of fluoride from aqueous solution onto MNAH-0.05 was studied, and the results are shown in Figure 20. The effect of an adsorbent amount (10, 15, 20, 25, 30 mg) at an agitation speed of 150 rpm, pH 7, contact time of 45 min, and reaction temperature of 25 ºC was investigated using 40 mL of F^- solution at an initial concentration of 20 mg L^{-1}. Figure 20A showed that the removal efficiency of fluoride increased significantly from 82.1 to 89.95%, as the

adsorbent amount increased from 10 to 20 mg, then slightly decreased as the adsorbent amount reached 30 mg. This is because a further increase in the adsorbent concentration might restrict the mass transfer of fluoride, consequently minimizing the number of active adsorption sites. An increased adsorbent dosage might also lead to adsorbent aggregation, and consequently, decreased available adsorbent sites (Mullick and Neogi, 2019).

pH: The adsorption experiment of aqueous fluoride by MNAH-0.05 LDH was carried out with the pH values of 3, 5, 7, 9 and 11 at the initial fluoride concentration of 20 mg L^{-1}, adsorbent dose of 0.01 g/40 mL, 25 ^{o}C, and 45 min. The influence of initial pH values on fluoride adsorption in an aqueous solution is given in Figure 20B. The adsorption efficiency reached a maximum at pH 5, and beyond this, it gradually decreased.

The adsorption efficiency can be explained by the charge properties of the LDH surface as it interacts with an aqueous solution. With the positive charge from the isomorphic substitution, LDH acquires other charges due to the adsorption of ions from aqueous, like H^+ or OH^- which is greatly influenced by the solution pH. In this case, at pH greater than 5, the surface of LDH becomes negatively charged due to the presence of more OH^- in the solution as a result of electrostatic interaction between LDH and OH^- decreasing its affinity for fluoride, whereas at pH < 5, the surface of LDH becomes more positively charged as a result of more H^+ (proton) in the solution. Therefore, this LDH preferred the adsorption of fluoride ions at pH below 5. Indeed, with a pH value of around 5, good fluoride adsorption was observed on the LDH material. This was because at low pH, the hydroxyl groups on the surface of LDHs were protonated, and the electrostatic interaction dominated fluoride adsorption (Wei *et al*., 2020). However, the removal efficiency decreased with increasing pH, primarily due to electrostatic repulsion between similarly charged species (Ali *et al*., 2020).

Initial concentration: The equilibrium results obtained for five different aqueous F^- concentrations (5, 10, 20, 30 and 40 mg/L) to determine the effect of initial fluoride concentration are given in Figure 20. As indicated in Figure 20, the highest removal efficiency of about 85.22% was obtained at low concentrations ranging from 5 to 10 mg L^{-1}, but otherwise, it was gradually decreased with further increased initial concentration which was due to exhaustion of the active sites of the adsorbent surface as the initial concentration increased (Figure 20C). The slight increase in adsorption efficiency from 5 to 10 ppm might

be attributed to the increase in driving force as the initial concentration increase (El-Bery *et al*., 2022; Hadi *et al*., 2021).

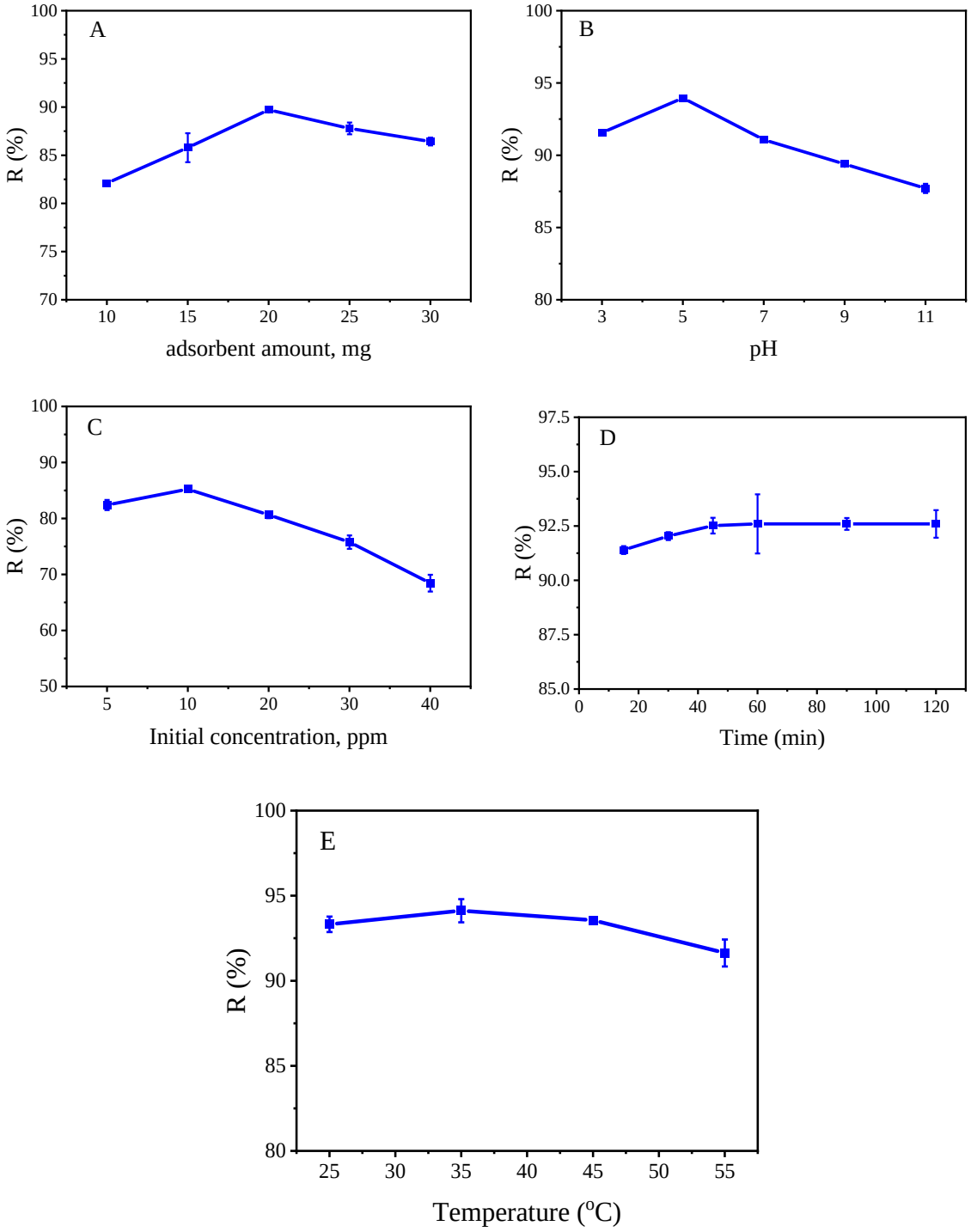

Figure 20. Effect of A) adsorbent amount, B) pH, C) Initial concentration, D) Time and E) temperature on removal efficiency of fluoride by MNAH-0.05

Time: The impact of contact time on adsorption of fluoride ion onto MNAH was examined by altering the duration of contact from 15 to 120 minutes while keeping the initial fluoride

amount at 20 mg/L, pH at 7 and temperature at 25 °C. The adsorption efficiency of MNAH exhibited a significant augmentation with increasing contact time and reached equilibrium after 45 min (Figure 20D). Within the first 45 minutes, about 92.5% of the fluoride adsorption was accomplished. The adsorption process certainly slowed down in the subsequent time frame. A comparable investigation was reported by Yu *et al*. (2015).

Temperature: The influence of temperature on adsorption efficiency of fluoride (20 mg/L) was tested using 0.25 g/L adsorbent at 150 rpm in the range from 25 to 55 °C, and the results are presented in Figure 20E. The results showed that throughout this range the effect of temperature was found to be negligible, and the material showed a wide range of thermal stability.

4.3.2 Fluoride Adsorption Kinetics, Isotherm and Thermodynamics

To characterize the sorption behavior of fluoride in aqueous solution over time, two kinetic models, namely pseudo-first order and pseudo-second order, were investigated. Results of fluoride removal kinetics onto MNAH-0.05 are shown in Figure 21A. Kinetic modeling was performed using nonlinear regression according to pseudo-first and pseudo-second order Equations in CAVS software which gave the results listed in Table 7.

Table 7. Outputs of the kinetic models fitted for aqueous fluoride adsorption data at a temperature of 25 ^{o}C and adsorbent amount of 0.01 g/40 mL.

Kinetics models	Parameters	MNAH-0.05
PFO	q_e	73.978
	K_1	0.296
	R^2	0.9999
PSO	q_e	74.304
	K_2	0.055
	R^2	0.9999

Both these kinetic models indicated that the equilibrium sorption capacity, q_e, obtained from the kinetic Equations was close to that obtained from the equilibrium study (experimental

adsorption capacity) (74.077 mg g^{-1}) for the fluoride initial concentration of 20 mg L^{-1}. Thus, it can be stated that both kinetic models fit the fluoride adsorption process well.

Since fluoride adsorption follows both pseudo-first-order and pseudo-second-order kinetics, the rate of fluoride adsorption might be controlled by the physisorption and chemisorption process associated with the physical and chemical characteristics of LDH and fluoride ions which involves the sharing of electrons between them, usually confined to only one layer of molecules on the surface and as well physically binding onto the adsorbent surface or entrapped into the pores (Mahjoubi *et al*., 2017).

Isotherm models such as Langmuir, Freundlich and Temkin were applied to identify the influence of fluoride initial concentration on the sorption process. The maximum adsorption capacity, q_{max}, listed in Table 8 exceeded that obtained experimentally, indicating that the studied adsorbent can retain larger quantities of fluoride (Langmuir, 1918).

Table 8. Outputs of the equilibrium isotherm models fitted for aqueous fluoride equilibrium adsorption data at a temperature of 25 ^{o}C and adsorbent amount of 0.01 g/40 mL.

Isotherm models	Parameters	MNAH-0.05
Langmuir	q_{max}	162.84
	K_L	0.168
	R^2	0.991
Freundlich	K_f	27.784
	N	1.785
	R^2	0.937
Temkin	K_T	1.776
	B_T	70.75
	R^2	0.996

In terms of the values of the correlation coefficients, R^2, listed in Table 8, which are goodness-of-fit measures and confirm the representativeness of the experimental data, the Temkin model provided a better fit to the experimental results than the other models tested (Figure 21B). The regression (R^2) of the Temkin isotherm plot of fluoride adsorption onto MNAH-0.05 LDH was found to be 0.996 (Table 8), indicating the interactions between

adsorbate and adsorbent likely play a vital role in the fluoride adsorption process. Notably, the equilibrium binding constant (k_T) was also significant. This indicated that this LDH could form a strong bond with fluoride (Sarma and Rashid, 2018). The positivity of the B_T value means that the adsorption processes were exothermic and predominantly physical (Nimibofa *et al*., 2017).

Table 9 presented the thermodynamic parameters obtained from the thermodynamic data of the sorbent material using van't Hoff plot in CAVS software.

Table 9. Thermodynamic parameters of the adsorption of fluoride onto MNAH-0.05.

Kc	T (°C)	ΔG (KJ mol^{-1})	ΔH (KJ mol^{-1})	ΔS (J mol^{-1})
55.86	25	-9.97	-6.49	12.55
64.011	35	-10.66		
58.09	45	-10.74		
43.82	55	-10.31		

The negative value of ΔG^o indicates that the sorption of fluoride onto the sorbent was spontaneous under the experimental conditions and thermodynamically feasible. The calculated ΔG^o values indicate the interaction between fluoride and LDH can be considered as physical process as the ΔG^o is in the range of 0 to -20 kJ mol^{-1} (Liu *et al*., 2014; Nimibofa *et al*., 2017).

The negative value of ΔH^o of fluoride adsorption confirms that the process is exothermic and proceeds well at low temperatures. So, the amount adsorbed at equilibrium decreased with increasing temperature. The positive value of ΔS^o confirms the selectivity of fluoride on the surface of LDH and suggests the possibility of structural changes or rearrangements in the fluoride–LDH interaction due to increased random effects of their interface (Asouhidou *et al*., 2012; Gök, 2020; Nimibofa *et al*., 2017).

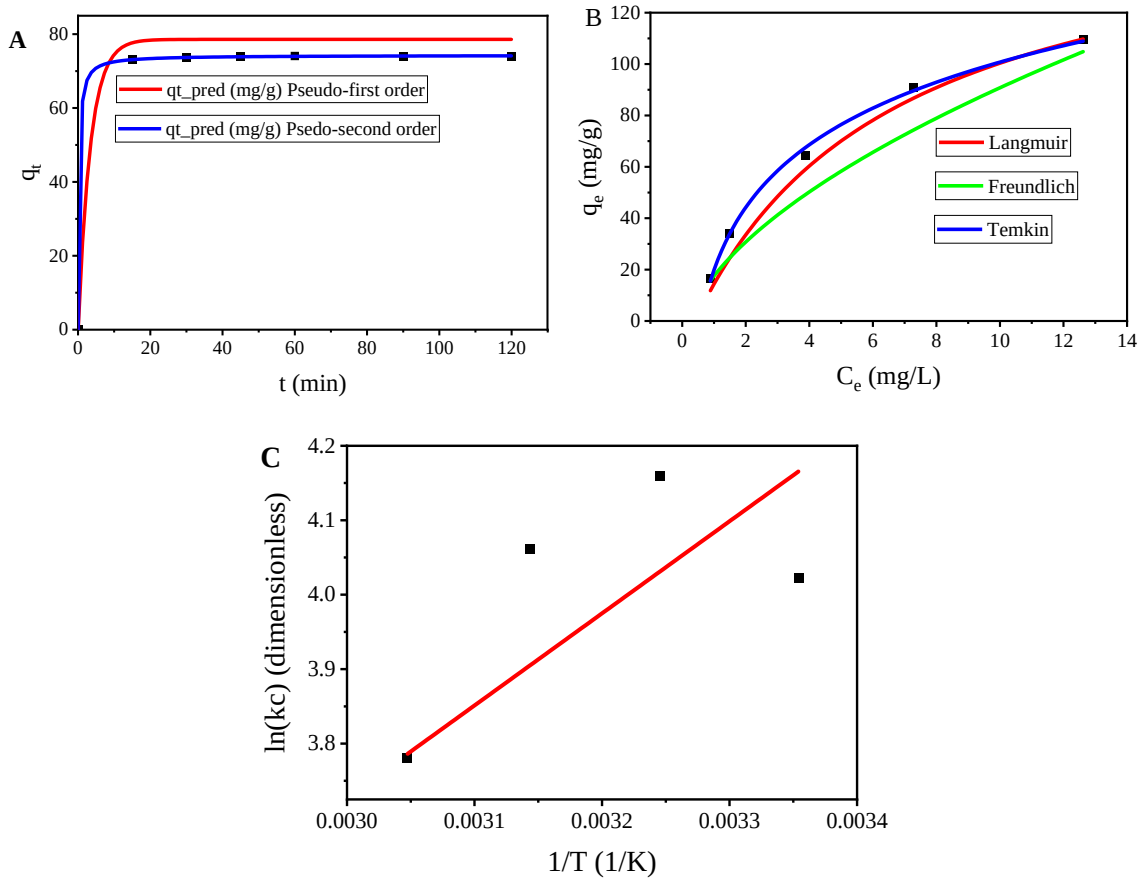

Figure 21. Graph of A) kinetic models, B) isotherm models and C) van't Hoff plot fitted to fluoride adsorption onto MNA-0.05

4.4 Fluoride Adsorption by Ce^{4+}-Doped Ni-Al LDHs

4.4.1 Investigation of Factors Influencing Fluoride Removal Efficiency

To investigate the effect of pH, initial concentration, contact time, adsorbent dose, temperature and agitation speed on the adsorption efficiency of fluoride on Ce^{4+}-doped Ni-Al LDHs, batch adsorption technique was used. The adsorption efficiencies of CNAHs were compared in the first set of tests in which CNAH-0.05 LDH (Table 10) was identified as the best-performing adsorbent and it was used for further studies. This test was done under the same conditions at 25 ºC, 45 min, pH 7, 0.2 g/L adsorbent, 40 mL 10 ppm F^- and 150 rpm. The results are displayed in Table 10. As indicated in Table 10, the adsorption capacity of fluoride onto NAH, CNAH-0.05, CNAH-0.1 and CNAH-0.2 were found to be 25.50, 31.32, 28.11 and 28.64 mg g^{-1}, respectively.

Table 10. Fluoride adsorption performance of CNAHs

Adsorbent	q_e, mg/g	R%
NAH	25.50	51.01
CNAH-0.05	31.32	62.64
CNAH-0.1	28.11	56.22
CNAH-0.2	28.64	57.28

Dosage: The Ce^{4+}-doped Ni-Al LDH with different doses (0.25, 0.5, 0.75, 1, 1.25 and 1.5 g/L) were studied for the adsorption efficiency of F^- from an aqueous solution of initial concentration of 10 mg/L fluoride at 25 ^oC agitating at 200 rpm for a contact time of 60 min. The result in Figure 22A shows that the adsorbent exhibited high removal efficiency of more than 90% and which marginally improved from 90.86 to 94.04% with the rise in the adsorbent concentration from 0.25 to 1.25 g/L, while it decreased when the adsorbent weight was further increased to 1.5 g/L. As proved in previous literature, increasing the adsorbent dosage increased the removal of fluoride ions as the number of sites available for adsorbent–adsorbate interaction increased. A further increase in the concentration of adsorbent made restrictions to the mass transfer of F^-, causing less efficiency. An increase in adsorbent dosage might also lead to adsorbent aggregation, and consequently, a decrease in available adsorbent sites (Mullick and Neogi, 2019).

pH: To investigate the pH effect on fluoride adsorption efficiency, experiments were performed at pH values of 3, 5, 7, 9 and 11 with an initial concentration of 10 mg/L, adsorbent dosage of 1.25 g/L, temperature of 25 °C, and interaction time of 60 min. The result of the pH effect on fluoride adsorption is given in Figure 22B. As the results indicated, the removal efficiency decreased slightly from pH 3 to pH 5, then remained constant up to pH 9 and decreased beyond that. Thus, it can be witnessed that the synthesized LDH has a wide range of pH stability and removal efficiency.

Initial fluoride concentration: Experimental results on the influence of initial concentration of fluoride ion on its removal were tested at 10, 20, 30, 40, 50 and 60 mg/L using 1.25 g/L adsorbent at 25 ^oC, pH 3 and 200 rpm for 60 min is shown in Figure 22C. The results revealed that the adsorption efficiency decreased with increasing initial concentration. Similar findings were previously reported indicating a decrease in uptake when initial concentration

increases due to the filling of the adsorbents' active sites with increasing initial concentration (El Rouby *et al*., 2020).

Contact time: A study showing the impact of interaction time on the efficiency of F^- removing using 1.25 g/L LDH adsorbent in 10 ppm F^- aqueous solution at agitation of 200 rpm, pH 3 and 25 ºC temperature is shown in Figure 22D. The results specified that the removal efficiency of F^- increased in the first 60 min, and thereafter there was no significant change. The existence of more adsorption sites at the start of the adsorption process allows faster removal because of the more surface area of adsorbent available for fluoride adsorption. However, a further increase in contact time leads to almost a constant fluoride removal rate as the adsorption sites are occupied (El Rouby *et al*., 2020).

Temperature: The influence of temperature on adsorption efficiency of fluoride (10 mg/L) was tested using 1.25 g/L adsorbent at 200 rpm and pH 3 in the range from 25 to 55 °C, and the results are presented in Figure 22E. The results showed that throughout this range the effect of temperature was found to be negligible, and the material showed a large range of thermal stability.

Agitation speed: The influence of agitation rate was also conducted by changing the agitation rate from 50 to 250 rpm using a thermostat shaker with 10 mg/L (initial concentration), 1.25 g/L (adsorbent concentration), 60 min (contact time), pH 3 and 25 ºC (temperature). Experimental results showed the removal efficiency increased significantly as the agitation speed increased up to 200 rpm (Figure 22F). The increase in agitation rate results in the dispersion of adsorbent particles in aqueous solution which can minimize the boundary layer for mass transfer and enhances the fluoride removal efficiency.

However, after 200 rpm, the efficiency of fluoride removal decreased with increasing agitation rate. This was happened due to the higher the agitation rate, the faster the adsorbate movement and the adsorbent kinetic energy and this leads to the temporary entrapment of F^- to the surface of the adsorbent. Therefore, the loosely attached adsorbates began to separate from the surface of the adsorbent. Again, high agitation may create a vortex which may decrease the fluoride-adsorbent interaction. A similar study by Mondal and Roy, (2016) also reported that increasing the agitation rate beyond 200 rpm reduced the fluoride removal efficiency by MWCNTs.

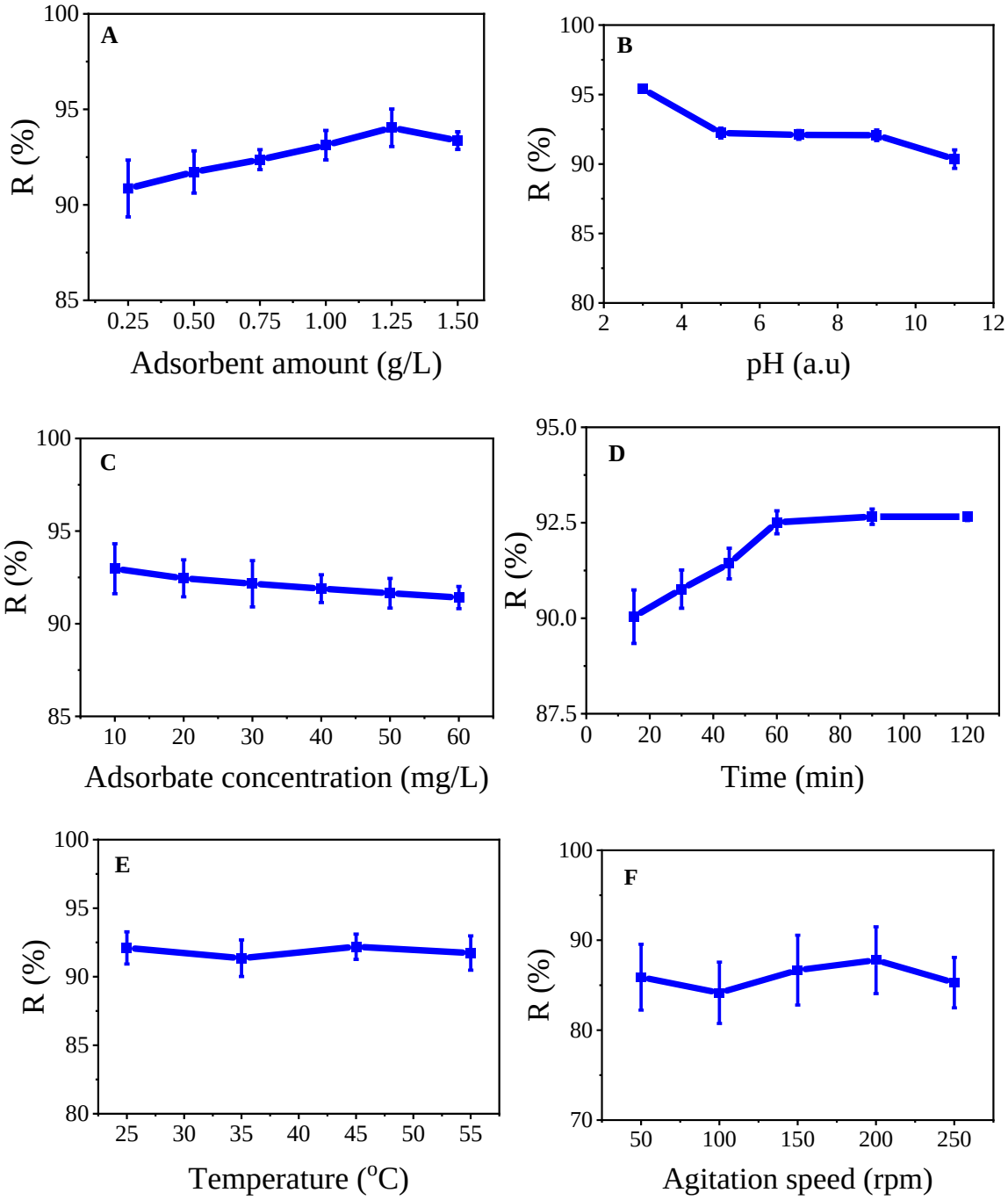

Figure 22. Effect of A) adsorbent amount B) pH, C) adsorbate concentration, D) contact time, E) temperature and F) agitation speed on removal efficiency of fluoride by CNAH-0.05

4.4.2 Kinetics, Isotherm and Thermodynamic Study of the Adsorption of Fluoride

The kinetic models such as PFO and PSO were employed to investigate the performance of fluoride removal from aqueous solution over a time range of 15 to 120 min, and the results are presented in Figure 23A and Table 11.

Table 11. Results from fitting PFO and PSO kinetic models to fluoride adsorption onto CNAH-0.05

Models	Constants	Values
PFO	q_e (mg/g)	92
	K_1 (min^{-1})	0.25
	R^2	0.999
PSO	q_e (mg/g)	92.97
	K_2 (min^{-1})	0.02
	R^2	0.999

CAVS software was employed to nonlinearly fit the models. As evidenced from the results, fluoride adsorption was fitted by the PFO and PSO kinetic models (R^2 = 0.999). The results suggested that the removal mechanism was controlled by both physisorption and chemisorption processes (Ho and McKay, 1998).

The isotherm experimental results obtained over the range of 10 to 60 mg/L concentration are given in Table 12 and Figure 23B.

Table 12. Results of equilibrium isotherm models fitted to fluoride adsorption data of CNAH-0.05

Models	Parameters	Values
Freundlich	K_f	10.36
	N	1.13
	R^2	0.999
Langmuir	q_{max}	238.27
	K_L	0.044
	R^2	0.999
Temkin	K_T	1.77
	B_T	137.75
	R^2	0.902

Isotherm models like Freundlich, Temkin and Langmuir were employed to determine the effect of initial concentration on the adsorption process. CAVS software was used for fitting the experimental results to these models. The maximum adsorption capacity of CNAH-0.05 LDH was 238.27 mg/g according to Langmuir mode. The best-fitted model provided the maximum adsorption capacity greater than the experimental result which indicated that the tested adsorbent can hold more quantity of F^- from the solution. According to the R^2 values recorded in Table 12, Freundlich and Langmuir models were found to fit the results better (Figure 23A). Thus, the adsorption can be explained in terms of the two models. This implied that multilayer (physical) as well as monolayer (chemical) adsorption phenomena can be observed between CNAH-0.05 and fluoride ions. Based on the dimensionless equilibrium parameter (K_L) of the Langmuir model values of less than unity indicated fluoride ions adsorption by CNAH-0.05 is a favorable process (Langmuir, 1918).

The effect of temperature on the adsorption of fluoride onto CNAH-0.05 was studied using van't Hoff fitting with CAVS software and the results were presented in Table 13.

Table 13. The thermodynamics data obtained from van't Hoff fitting for adsorption of fluoride onto CNAH-0.05

k_c (dimensionless)	T (°C)	ΔG (KJ/mol)	ΔH (KJ/mol)	ΔS (J/mol)
9.16	25	-5.49	-0.22	17.48
8.48	35	-5.48		
9.28	45	-5.89		
8.82	55	-5.94		

The equilibrium constant (k_c), enthalpy change (ΔH) and entropy change (ΔS) were obtained at different temperatures. The thermodynamic study revealed that the adsorption process was spontaneous. The ΔH value is negative, indicated that the adsorption process was exothermic and released heat. The positive ΔS value indicated that the entropy of the system increased during the adsorption process. The values of ΔG are negative, indicated that the adsorption process was spontaneous and thermodynamically favorable.

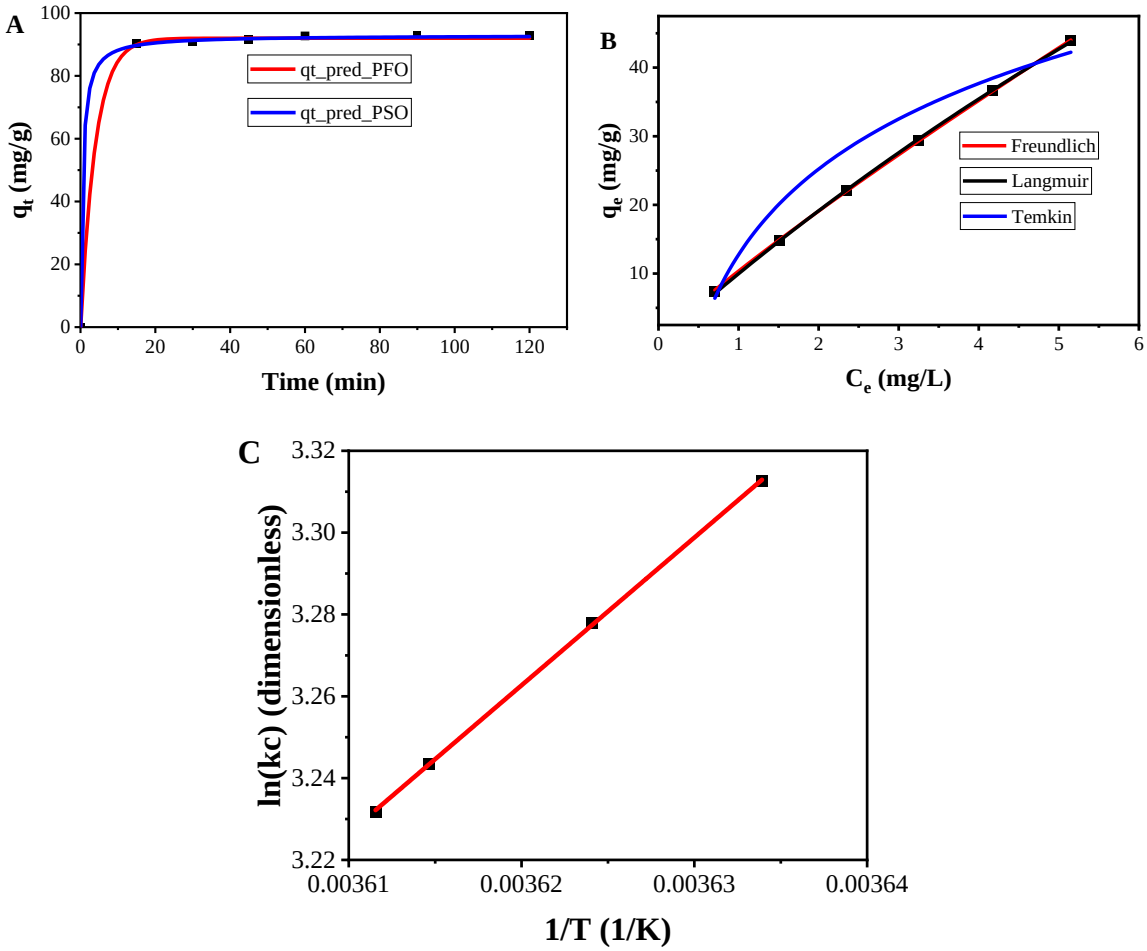

Figure 23. Graph showing A) kinetic models, B) isotherm models and C) van't Hoff plot fitted to the adsorption of fluoride by CNAH-0.05

4.5 Co-existing Ions Influence on F^- Removal Effectiveness of LDHs

The influence of Cl^-, NO_3^- and SO_4^{2-} anions at 5, 10 and 20 mg/L concentrations on the defluoridation performance of the synthesized LDHs were investigated using CNAH-0.05 LDH at F^- concentration of 20 mg/L and the result is presented in Figure 24. The data showed that NO_3^- has less effect on the fluoride adsorption performance of Ce^{4+}-doped Ni-Al LDH when present at low concentrations. This result parallels previous findings of F^- removal (Zhou *et al*., 2018). This may be justified by the possible chemical reaction of the AlF_x complexes, the precipitation of CeF_4 and its complexes being involved in the removal process. This implied that F^- has a stronger affinity for CNAH-0.05 adsorbent than NO_3^- (Wei *et al*., 2020).

However, even though Cl^- and SO_4^{2-} significantly affect the fluoride adsorption performance, the effect of SO_4^{2-} was more pronounced. This was due to competitive adsorption on the active sites available on the surface of the adsorbent during the adsorption process. The higher charge density of sulfate ions leads to a stronger repulsive force against the negatively charged fluoride ion and attraction against positively charged adsorbent, hindering their adsorption and allowing sulfate ions to be preferentially adsorbed. The SO_4^{2-} in the solution can also progressively reside in the active adsorption sites on the adsorbent surface, making the adsorbent unable to take up much of the fluoride ion (He *et al*., 2019; Tao *et al*., 2020). Therefore, the influence of these ions on defluoridation might be due to their relatively higher affinity toward LDH. As reported in a previous study, indeed LDH showed a preference for interlayer anions in the order CO_3^{2-}>> F^-/SO_4^{2-} > Cl^- > NO_3^- (Cavani *et al*., 1991; Hibino, 2018).

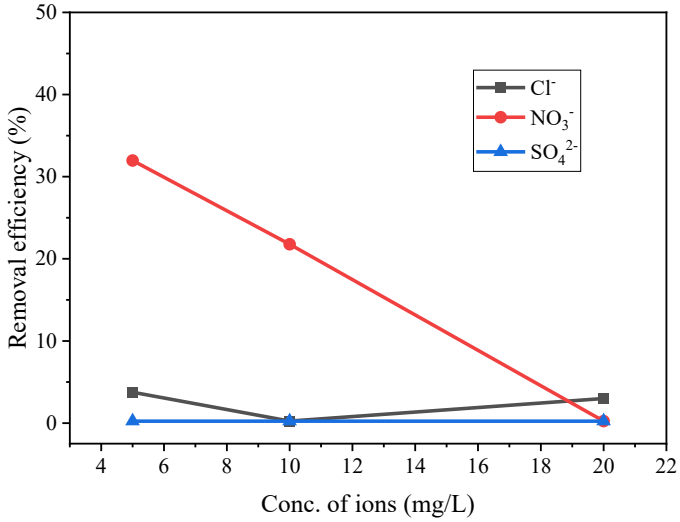

Figure 24. The influence of SO_4^{2-}, Cl^- and NO_3^- on the adsorption of fluoride by CNAH-0.05

4.6 Reusability of the Synthesized LDHs in Fluoride Adsorption

We used 0.1 M NaOH solution as a desorption agent to regenerate CNAH-0.05 after fluoride adsorption from aqueous solution. Then CNAH-0.05 was soaked in a mixture of 2 M NaOH and 1 M $NaHCO_3$ to fully recover the LDH structure. We performed a series of adsorption and desorption experiments with the doped LDH, and the obtained results are indicated in Figure 25. These results demonstrated that CNAH-0.05 was reused up to four times without significant loss of adsorption capacity. This was because the Ce^{4+} dopant enhanced the reusability of the adsorbent and resulted in fluoride removal efficiencies of 92.96%, 84.5%,

78.71%, and 70.76% for the first four cycles. Therefore, Ce^{4+} doped Ni-Al LDH showed enhanced regeneration performance.

The regeneration performance of LDHs is a crucial factor in their practical applications for removing fluoride from aqueous solutions. The study by (Tao *et al*., 2020) investigated the regeneration performance of Ce-AlOOH towards fluoride adsorption with 2% and 3% oxalic acid solutions. They found that Ce-AlOOH and Ce-$AlOOH_{oa}$ exhibited good regeneration performance with an average removal efficiency of 76 and 70%, respectively after four consecutive regeneration cycles.

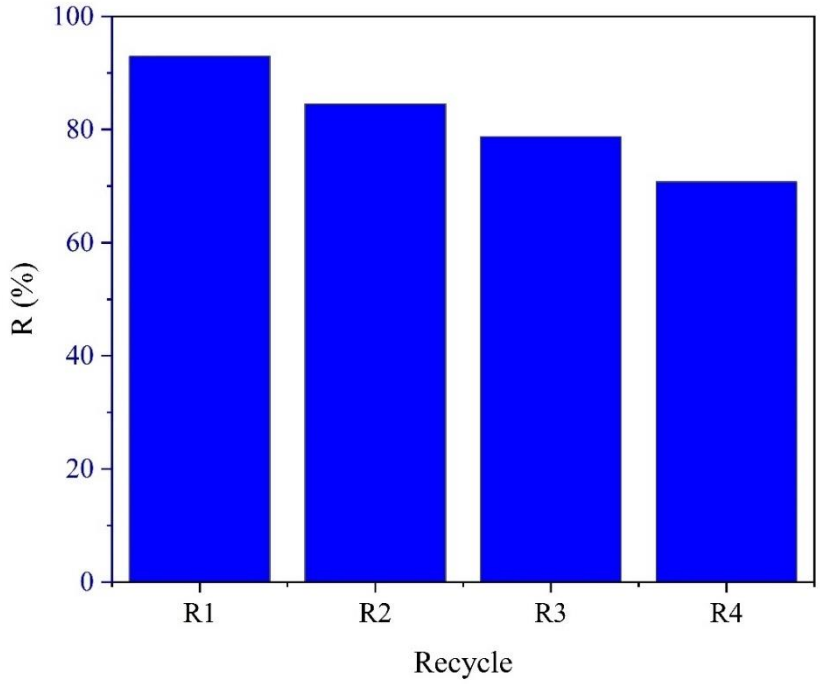

Figure 25. Recyclability of CNAH-0.05 for the adsorption of fluoride

4.7 Fluoride Adsorption by Mn^{2+} Doped Ni-Al LDOs

4.7.1 Fluoride Adsorption Performance of MNAOs

In this study, the fluoride adsorption performances of MNAOs were investigated. The capacity and efficiency of adsorbing fluoride ions were evaluated using different doping levels of Mn^{2+} in the LDO structure. The obtained data (Table 14) presented the fluoride adsorption performance of the MNAOs, represented by the adsorption capacity (q_e) in milligrams per gram (mg/g) and the removal efficiency (R) in percentage (%) at an initial F^-

concentration of 10 ppm, an adsorbent amount of 0.2 g/L, pH 7, temperature of 25 ^{o}C and an agitation speed of 150 rpm.

The results of the study indicated a notable enhancement in fluoride adsorption performance upon the introduction of Mn^{2+} dopant into the Ni-Al LDO structure. As the Mn^{2+} doping level increased from 0 to 20%, both the capacity and efficiency of adsorption showed a consistent improvement.

Regarding the adsorption capacity, the highest value was observed for the MNAO-0.2 sample, which exhibited a q_e of 30.75 mg/g. This suggested that the presence of Mn^{2+} in the LDO structure enhanced the surface reactivity and increased the active sites available for fluoride adsorption. These findings align with previous studies that have reported the beneficial role of metal dopants in promoting the capacity of adsorption in different adsorbents (Li *et al*., 2019).

Similarly, the removal efficiency of fluoride ions also displayed an increasing trend with higher Mn^{2+} doping levels. The MNAO-0.2 exhibited the highest removal efficiency of 61.50%, indicating its superior ability to extract fluoride ions from aqueous solutions. This enhancement can be ascribed to the synergistic interplay between Mn^{2+} dopant and Ni-Al LDO matrix, which enhanced the affinity and selectivity of the adsorbent towards fluoride ions (Luo *et al*., 2019).

Moreover, the observed improvements in both adsorption capacity and removal efficiency can be attributed to several factors. Primarily, the incorporation of Mn^{2+} ions might alter the structural and surface properties of the LDO, resulting in the creation of additional active sites and increased surface area as observed from BET analysis, which facilitated the adsorption process. Secondly, Mn^{2+} dopants might have introduced new chemical interactions, such as coordination bonds or ion exchange mechanisms, between the adsorbent and fluoride ions, thereby enhancing the adsorption performance (Li *et al*., 2019; Zhou *et al*., 2018).

Therefore, this study highlights the enhanced fluoride adsorption performance of Mn^{2+}-doped Ni-Al layered double oxides. These findings underscore the potential of MNAOs as promising adsorbents for removing fluoride ions from water sources. Further investigations

of parameters that influence the adsorption of fluoride were carried out using the MNAO-0.2 adsorbent.

Table 14. Fluoride adsorption performance of MNAOs

Adsorbent	q_e, mg/g	R, %
NAO	28.80	57.61
MNAO-0.05	29.42	58.84
MNAO-0.1	30.40	60.79
MNAO-0.2	30.75	61.50

4.7.2 Influence of Different Parameters on the Adsorption of Fluoride by MNAO-0.2

Effect of pH: A series of experiments were conducted to examine the impact of pH on the adsorption of fluoride ions by MNAO-0.2 fixing dose at 0.25 g/L, initial concentration at 10 ppm, temperature at 25 ^{o}C, agitation at 150 rpm and time at 60 min. The pH levels tested were 3, 5, 7, 9, and 11. The adsorption capacities at these pH values were determined to be 33.74, 21.64, 14.04, 10.47, and 2.24 mg/g, respectively (Figure 26A). These results indicated that the capacity of adsorption decreased with increasing pH. The adsorbing efficiencies were also calculated based on the concentrations of fluoride ion in the solution at the start and end of adsorption. The removal efficiencies at pH 3, 5, 7, 9, and 11 were found to be 84.35, 54.11, 35.11, 26.18, and 5.61%, respectively (Figure 26A). These values indicated that the removal efficiency decreased as the pH of the solution increased.

The observed trend can be explained by the influence of pH on the surface charge of MNAO-0.2 and the speciation of fluoride ions in solution. At lower pH values, the surface of MNAO-0.2 tends to have a positive charge, which facilitated the adsorption of F^- due to electrostatic attraction. With increasing pH, the charge on the surface of the adsorbent becomes less positive, leading to reduced adsorption efficiency (Eniola *et al*., 2020). Moreover, the speciation of fluoride ions in solution is pH-dependent, with different forms of fluoride ions present at different pH values. At lower pH levels, the concentration of the more adsorbable form of fluoride ions, F^-, might be higher, resulting in greater adsorption efficiency. However, as the pH increased, the proportion of the less adsorbable forms of fluoride ions, HF, might increase, leading to lower adsorption efficiency (Richards *et al*., 2010).

The findings of this study were consistent with previous research on the impacts of pH on F^- adsorption using different adsorbents. For instance, Zhou *et al*., (2018) reported a direct decrease in F^- adsorption efficiency as pH increased from 3 to 6 using layered Al-Zr-La Tri-metal hydroxide. Similarly, Yang *et al*. (2022) found that when pH decreased, adsorption increased as a result of the gradually increasing positive charges on the surface of the lanthanum-modified zeolite, which can draw fluoride for adsorption.

Effect of Initial Concentration: In this study, the adsorption capabilities of MNAO were evaluated for fluoride removal from aqueous solutions at various initial fluoride concentrations. The initial fluoride concentrations tested were 10, 20, 30, 40, 50, and 60 ppm. The results indicated that the removing efficiencies of fluoride ions by MNAO were 73.38, 61.12, 63.98, 49.05, 41.5, and 34.12% for the respective initial fluoride concentrations (Figure 26B).

Furthermore, the adsorption capacities of MNAO for fluoride ions were determined to be 29.35 mg/g, 48.9 mg/g, 76.77 mg/g, 78.48 mg/g, 83 mg/g, and 81.9 mg/g, respectively, for the corresponding initial fluoride concentrations (Figure 26B). These findings indicated that the efficiency and capacity of adsorption of fluoride ions by MNAO are influenced by the initial fluoride concentration. Higher initial fluoride concentrations generally result in higher adsorption capacities but may lead to slightly lower removal efficiencies.

The observed trend in fluoride removal can be attributed to the availability of adsorption sites on the MNAO surface. At lower initial fluoride ion concentrations, there are more available adsorption sites on the MNAO surface that are not occupied. This allows for a higher percentage of fluoride ions to be removed from the solution. As the initial concentration of fluoride increases, these available sites become progressively filled. This leads to a lower removal efficiency of fluoride. However, it's important to note that even though the percentage removal decreases, the adsorption capacity per unit mass of the adsorbent can increase with higher initial concentrations (Eniola *et al*., 2020; Gök, 2020).

Effect of Dose: In this study, the impact of the amount of MNAO adsorbent on the adsorption of fluoride ions was examined. The adsorbent doses tested were 0.25, 0.5, 0.75, 1.0, 1.25, and 1.5 g/L. The adsorption capacities at these doses were determined to be 77.33,

50.11, 33.17, 25.78, 21.67, and 18.6 mg/g, respectively (Figure 26C). The removal efficiencies of fluoride ions were also calculated based on the concentrations of fluoride in the solution at the beginning and end of the adsorption process. The removal efficacies at the adsorbent doses of 0.25, 0.5, 0.75, 1.0, 1.25, and 1.5 g/L were found to be 64.44, 83.52, 82.92, 85.93, 90.31, and 93.02%, respectively (Figure 26C). These results indicate that adsorption capacities decrease while removal efficiencies increase with increasing amounts of MNAO adsorbent.

The observed trend can be described by the availability of more adsorption sites with increasing adsorbent dose. At higher adsorbent doses, a greater surface area of the MNAO is exposed to the fluoride ions in the aqueous solution, supplying more active sites for the adsorption. Consequently, more fluoride ions can be captured and removed from the solution, resulting in higher adsorption efficiencies. Moreover, the increased adsorption efficiency can also be attributed to increased collision frequency between fluoride ions and the adsorbent surface at higher adsorbent doses. With a higher concentration of adsorbent, there are more chances for fluoride ions to come into contact with the active sites on the Mn^{2+}-doped Ni-Al LDO, leading to enhanced adsorption performance (Mullick and Neogi, 2019).

As the adsorbent amount increases, more surface area becomes available for adsorption. Initially, this can lead to an increase in the adsorption capacity as more active sites are exposed for adsorbing fluoride ions. However, as the adsorbent dose continues to increase, the active sites may become saturated, limiting further adsorption and causing mass transfer resistance. This saturation effect can result in a decrease in adsorption capacity. Again, at higher adsorbent doses, the adsorbent particles may have a greater tendency to aggregate or clump together. This can create diffusion limitations, reducing the accessibility of the fluoride ions to the active sites at the adsorbent surface. As a result, the adsorption capacity may decrease, while the removal efficiency can still be high due to the overall contact between the adsorbent and the solution (Mullick and Neogi, 2019).

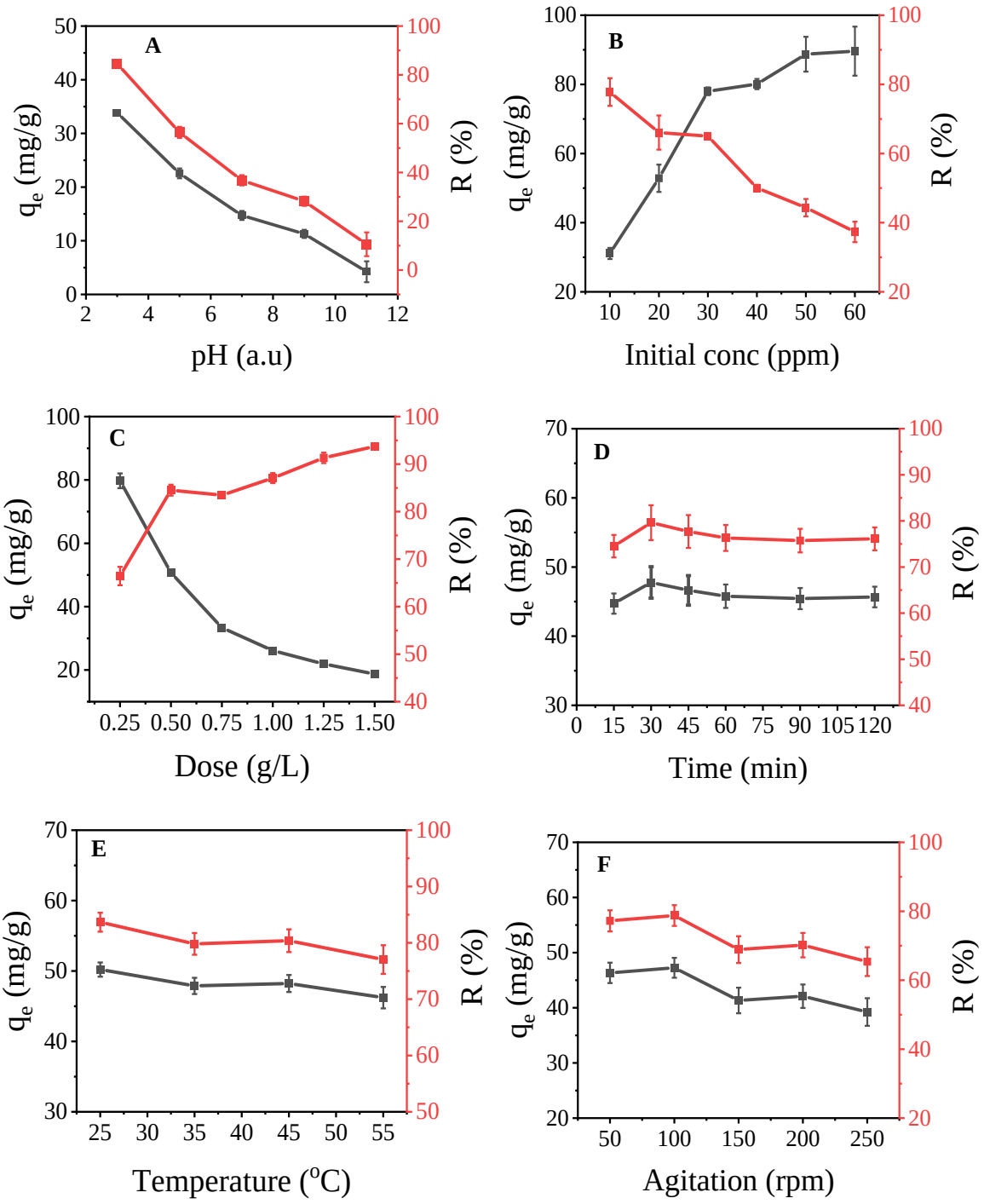

Figure 26. Effect of A) pH, B) initial concentration, C) dose, D) contact time, E) temperature and F) agitation speed on fluoride adsorption by MNAO-0.2

Contact time: The impact of contact time on adsorbing fluoride onto MNAO was examined by altering the duration of contact from 15 to 120 minutes while keeping the initial fluoride amount at 30 mg/L, pH at 3 and temperature at 25 °C. The adsorption capacity of MNAO exhibited a significant augmentation with increasing contact time and reached equilibrium after 30 minutes (Figure 26D). Within the first 30 minutes, approximately 75.43% of the

fluoride adsorption could be accomplished. The adsorption process certainly slows down in the subsequent time frame. A comparable investigation was reported by Yu *et al*. (2015).

Temperature: The impact of temperature on the adsorption process of fluoride onto MNAO was investigated in this study. The capacities and efficiencies of adsorption were evaluated at different temperatures, spanning from 25 to 55 °C. The findings showed that fluoride adsorbing capacity of the adsorbent decreased as the temperature increased. Specifically, at 25 °C, an adsorbing capacity of 49.31 mg/g was achieved, which decreased to 46.86, 47.12, and 44.66 mg/g at 35, 45, and 55 °C, respectively (Figure 26E). Similarly, the removal efficiencies exhibited a similar trend, with higher temperatures resulting in decreased removal efficiencies. At 25 °C, a removal efficiency of 82.18% was achieved, which decreased to 78.10, 78.53, and 74.44% at 35, 45, and 55 °C, respectively (Figure 25E). These findings indicated that the adsorption of fluoride onto MNAO is temperature-dependent, with higher temperatures leading to reduced adsorption capacities and removal efficiencies. A similar previous study was reported by Mullick and Neogi (Mullick and Neogi, 2019).

Effect of Agitation Speed: The influence of agitation speed on fluoride adsorption by the synthesized LDO was investigated in this study. The adsorption capacities and removal efficiencies were evaluated at agitation speeds of 50, 100, 150, 200, and 250 rpm. The results indicated that the agitation speed influenced both the capacity and efficiency of the adsorption of fluoride ions.

The adsorption capacity of fluoride ions showed some variation with changing agitation speeds. At 50 rpm, a capacity of 44.45 mg/g adsorption was observed, which increased slightly to 45.45 mg/g at 100 rpm. However, beyond 100 rpm, the adsorption capacity started to decrease. The values obtained were 38.98, 39.95, and 36.74 mg/g at agitation speeds of 150, 200, and 250 rpm, respectively (Figure 26F).

Similarly, the removal efficiencies followed a similar trend. At lower agitation speeds, higher removal efficiencies were observed. At 50 rpm, a removal efficiency of 74.08% was achieved, which increased to 75.75% at 100 rpm. However, as the agitation speed further increased, the removal efficiency gradually decreased. The values obtained were 64.97%, 66.58%, and 61.23% at agitation speeds of 150, 200, and 250 rpm, respectively (Figure 26F).

These results suggest that there is an optimal agitation speed for the adsorption of fluoride by MNAO. At lower agitation speeds, the adsorbent particles have more contact time with fluoride ions, leading to higher adsorption capacities and removal efficiencies. However, at higher agitation speeds, the agitation-induced turbulence might hinder the adsorption process, resulting in decreased adsorption capacities and removal efficiencies (Mondal and Roy, 2016).

4.7.3 Studies on Fluoride Adsorption Kinetics, Isotherms and Thermodynamic

The results obtained from the experiments were fitted to both the PFO and PSO kinetic models. The corresponding parameters were determined to examine the adsorption mechanism and identify rate-controlling steps. Table 15 presented the values of q_e, k_1, k_2, and the correlation coefficients (R^2) for both models.

Table 15. Values of parameters of kinetics and isotherm models fitted to fluoride adsorption onto MNAO-0.2

Types of models		Parameters and their values					
Kinetics models	PFO	q_e (mg/g)	44.29	K_1	0.24	R^2	0.9992
	PSO	q_e (mg/g)	44.41	K_2	0.08	R^2	0.9987
Isotherm models	Freundlich	K_f	29.02	N	3.25	R^2	0.80
	Langmuir	q_{max} (mg/g)	98.41	K_L	0.18	R^2	0.903
	Temkin	K_T	1.85	B_T	119.36	R^2	0.87

Table 15 and Figure 27A show that both models fit the experimental data well, as indicated by the high values of R^2. However, the values of q_e obtained from both models are very close to each other and to the experimental value, suggesting that both models can adequately describe the equilibrium adsorption of fluoride onto MNAO. This suggests that the process is controlled by a combination of mass transfer and chemical reaction mechanisms (Liu *et al*., 2019; Oladoja *et al*., 2015).

The adsorption of fluoride from aqueous solutions by MNAOs was investigated at different amounts of initial concentration (10, 20, 30, 40, 50 and 60 mg/L). The equilibrium results were fitted to three isotherm models such as Freundlich, Langmuir and Temkin. The

Langmuir model showed the best fit to the experimental results, with better correlation coefficients (R^2 = 0.903) (Table 15 and Figure 27B). The Langmuir model proposed that the adsorption process was monolayer or uniform (Vigdorowitsch *et al*., 2021). The model also implies that the adsorption occurred on a finite number of identical sites with uniform energy (Ayawei *et al*., 2017). The Langmuir model yielded a remarkable maximum adsorption capacity (q_m) of 98.41 mg/g, surpassing the values reported for other metal-based adsorbents (Yu et al., 2015). The Freundlich and Temkin models did not fit well with the data, indicating that the adsorption process is not heterogeneous. The Temkin model gave a high value for the heat of adsorption (B_T), suggesting that the adsorption was strongly exothermic (Nimibofa *et al*., 2017). This agrees with findings obtained from the effect of temperature study.

Thermodynamic parameters obtained from van't Hoff fitting were used to analyze the adsorption of fluoride onto MNAO (Figure 27C). The equilibrium constant (K_c) was determined at various temperatures altering from 25 to 55 °C. The values of K_c ranged from 9.22 at 25 °C to 5.82 at 55 °C, indicating a decrease in the equilibrium constant with increasing temperature (Table 16).

Table 16. Values of thermodynamic parameters from van't Hoff plot of fluoride adsorption onto MNAO-0.2

Kc	T (°C)	ΔG (KJ mol^{-1})	ΔH (KJ mol^{-1})	ΔS (J mol^{-1})
9.22	25	-5.51	-11.02	-18.73
7.13	35	-5.03		
7.32	45	-5.26		
5.82	55	-4.81		

This showed that the adsorption capacity of MNAO-0.2 decreased as the temperature increased, which is typical for a physical adsorption process. Negative values of Gibbs free energy change (ΔG) indicate that the adsorption process is spontaneous. On the other hand, negative values of enthalpy change (ΔH) suggest that the adsorption process is exothermic. The negative value of entropy change (ΔS) indicates that the randomness or disorder of the system decreases in the course of the adsorption, which is consistent with the formation of a more ordered surface complex between fluoride and MNAO-0.2 (Mullick and Neogi, 2019).

Generally, these thermodynamic parameters provide insights into the spontaneity, energetics, and randomness of the fluoride adsorption onto MNAO-0.2.

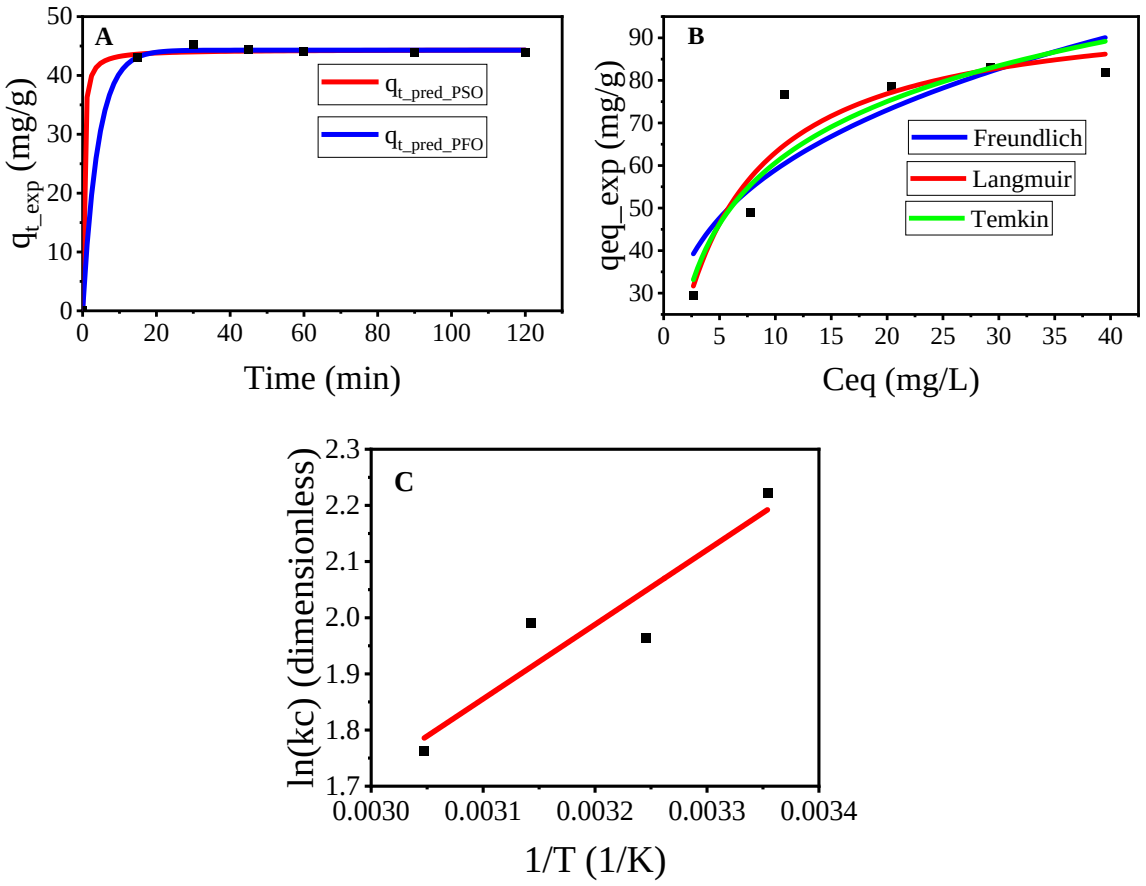

Figure 27. Graph of A) kinetic models, B) isotherm models and C) van't Hoff plot fitted to fluoride adsorption by MNAO-0.2

4.7.4 Influence of Coexisting Ions

The influence of coexisting ions, namely Cl^-, SO_4^{2-} and NO_3^-, on the adsorption of fluoride (F^-) by MNAO-0.2 was studied. The experiment involved varying concentrations of the coexisting ions at 10, 20, and 30 ppm while maintaining a concentration of F^- at 30 mg/L. The findings showed that the presence of SO_4^{2-} led to removal efficiencies of 70.33, 64.19 and 57.59% for F^- at the respective ion concentrations of 10 ppm, 20 ppm, and 30 ppm. Similarly, in the presence of NO_3^-, removal efficiencies of 61.47, 60.88 and 50.54% were observed. When Cl^- was present, the removal efficiencies for F^- were 60.42, 52.03 and 44.70% at the corresponding ion concentrations (Figure 28). These findings demonstrate that the coexistence of ions can significantly affect the adsorption of fluoride, with varying degrees of influence observed depending on the specific ion present (Luo *et al.*, 2019).

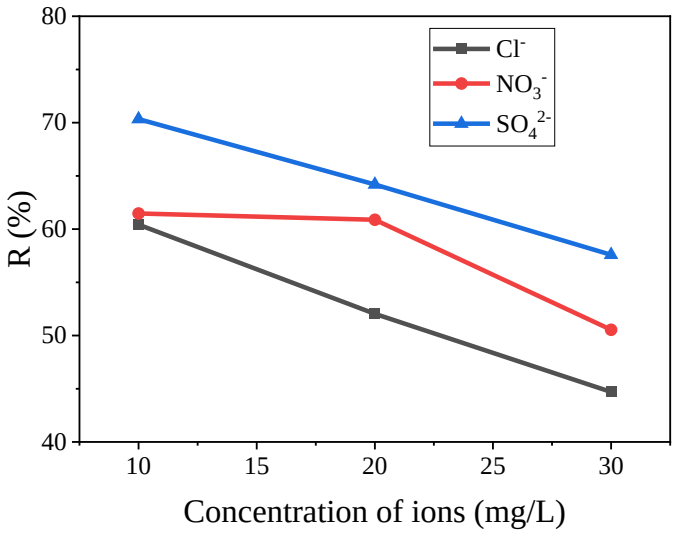

Figure 28. Effect of coexisting ions on fluoride adsorption by MNAO-0.2

4.7.5 Reusability Performance of MNAO-0.2

In this study, the reusability of MNAO-0.2 as an adsorbent for removing fluoride ions from aqueous solutions was investigated. The adsorption performance of the material was evaluated over five consecutive regeneration cycles. The initial fluoride concentration in the aqueous solution was maintained at 30 mg/L, and a 0.5 g/L dosage of the adsorbent was used.

The results demonstrated that the MNAO-0.2 exhibited promising re-usability, with an average fluoride removal efficacy of 80.71% over the five regeneration cycles. The efficiency of fluoride removal gradually decreased with each cycle, with removal percentages of 85.86, 83.12, 79.56, 78.17 and 73.82% for the first, second, third, fourth, and fifth cycles, respectively (Figure 29).

The obtained results indicate that the MNAO-0.2 can be effectively employed for fluoride removal from aqueous solutions, even after multiple regeneration cycles. The gradual decrease in removal efficacy observed with each cycle suggested some minor loss of adsorption capacity over time. However, the material still retained a considerable ability to adsorb fluoride ions, highlighting its potential as a reusable adsorbent for fluoride removal applications.

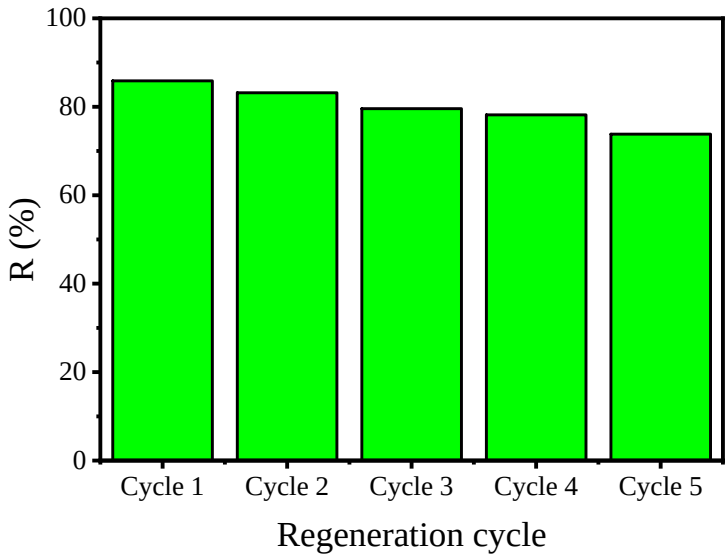

Figure 29. Reusability of MNAO-0.2 for fluoride removal over five regeneration cycles

4.8 Fluoride Adsorption by Ce^{4+} Doped Ni-Al LDOs

4.8.1 Fluoride Adsorption Performance of CNAOs

In this study, the fluoride adsorption performances of CNAOs were investigated. The capacity and efficiency of adsorbing fluoride ions were evaluated using different doping levels of Ce^{4+} in the LDO structure. The obtained data (Table 17) presented the fluoride adsorption performance of the CNAOs, represented by the adsorption capacity (q_e) in milligrams per gram (mg/g) and the removal efficiency (R) in percentage (%) at an initial F^- concentration of 10 ppm, an adsorbent amount of 0.2 g/L, pH 7, the temperature of 25 ^oC and an agitation speed of 150 rpm.

The results of the study indicated a notable enhancement in fluoride adsorption performance upon the introduction of Ce^{4+} dopant into the Ni-Al LDO structure. As the Ce^{4+} doping level increased from 0 to 20%, both the capacity and efficiency of adsorption showed a consistent improvement. Regarding the adsorption capacity, the highest value was observed for the CNAO-0.2 sample, which exhibited a q_e of 28.48 mg/g. This suggested that the presence of Ce^{4+} in the LDO structure enhanced the surface reactivity and increased the active sites available for fluoride adsorption. These findings align with previous studies that have reported the beneficial role of metal dopants in promoting the capacity of adsorption in different adsorbents (Li *et al*., 2019). Similarly, the removal efficiency of fluoride ions also

displayed an increasing trend with higher Ce^{4+} doping levels. The CNAO-0.2 LDH exhibited the highest removal efficiency of 71.19%, indicating its superior ability to extract fluoride ions from aqueous solutions. This enhancement can be ascribed to the synergistic interplay between Ce^{4+} dopant and Ni-Al LDO matrix, which enhanced the affinity and selectivity of the adsorbent towards fluoride ions (Luo *et al*., 2019).

Moreover, the observed improvements in both adsorption capacity and removal efficiency might be attributed to several factors. Primarily, the incorporation of Ce^{4+} ions might alter the structural and surface properties of the LDO, resulting in the creation of additional active sites and increased surface area, which facilitated the adsorption process. Secondly, Ce^{4+} dopants might have introduced new chemical interactions, such as coordination bonds or ion exchange mechanisms, between the adsorbent and fluoride ions, thereby enhancing the adsorption performance (Li *et al*., 2019; Zhou *et al*., 2018).

Therefore, this study highlighted the enhanced fluoride adsorption performance of CNAO LDOs. The incorporation of Ce^{4+} dopants at various levels resulted in significant improvements in adsorption capacity and removal efficiency. These findings underscored the potential of CNAOs as promising adsorbents for removing fluoride ions from water sources. Further investigations of parameters that influence the adsorption of fluoride were carried out using the CNAO-0.2 adsorbent.

Table 17. Fluoride adsorption performance of CNAOs

Adsorbent	q_e, mg/g	R, %
NAO	23.03	57.57
CNAO-0.05	27.06	67.64
CNAO-0.1	26.55	66.37
CNAO-0.2	28.48	71.19

4.8.2 Evaluation of Factors Influencing Fluoride Adsorption

Effect of pH: In this study, the adsorption capacity and efficacy of fluoride were investigated by evaluating the performance of CNAO-0.2 at various pH levels of 3, 5, 7, 9 and 11 (Figure 30A). The experiment was carried out by slowly mixing 0.25 g/L adsorbent and 10 ppm

initial F^- concentration agitating at 100 rpm for 45 min at 25 ^oC. The results revealed a clear trend in the fluoride adsorption efficiency of CNAO-0.2 with changing pH. At a lower pH value of 3, CNAO-0.2 demonstrated a high adsorption capacity of 27.06 mg/g, indicating its strong affinity for fluoride ions. However, as the pH increased, the adsorption capacity of CNAO-0.2 decreased significantly. The adsorption capacity dropped to 2.6 mg/g at pH 11, suggesting a reduced ability of CNAO-0.2 to effectively adsorb fluoride ions. Similarly, the removal efficiency exhibited a downward trend with increasing pH. At pH 3, CNAO-0.2 achieved a removal efficiency of 67.64%, indicating its excellent performance in removing fluoride from the solution.

However, as the pH increased to 11, the removal efficiency decreased significantly to 6.49%, highlighting a diminished effectiveness of CNAO-0.2 in removing fluoride ions under alkaline conditions. This decrease in efficiency can be credited to the changing surface charge of CNAO-0.2 and the speciation of fluoride ions with varying pH values. At lower pH, the surface of CNAO-0.2 tends to be positively charged, favoring the electrostatic interaction and adsorption of fluoride ions. However, at higher pH, the surface charge became more negative, leading to repulsion between the negatively charged CNAO-0.2 surface and fluoride ions, resulting in decreased adsorption efficacy (Richards *et al*., 2010).

Effect of Dose: Another crucial factor is the impact of varying adsorbent amounts on fluoride adsorption using CNAO-0.2. Six different concentrations of the adsorbent were employed, namely 0.25, 0.5, 0.75, 1.0, 1.25 and 1.5 g/L (Figure 30B). In terms of adsorption capacity, the highest value was observed at the lowest adsorbent concentration, with a recorded capacity of 57.20 mg/g. As the adsorbent amount increased gradually, the adsorption capacity experienced a significant decline reaching a capacity of 19.13 mg/g at 1.5 g/L. The experimental reduction in adsorption capacity might be ascribed to the limited accessibility of active sites on the CNAO-0.2 surface as its amount increased due to aggregation (Mullick and Neogi, 2019). However, the highest removal efficiency, about 95%, was achieved at an adsorbent concentration of 1.0 g/L. After reaching this highest peak the removal efficiency remained constant.

Agitation speed: The consequence of agitation speed on the adsorption of fluoride ions using CNAO-0.2 was also investigated. The experiment aimed to evaluate how varying agitation speeds influenced the adsorption capacity and efficiency of fluoride ions onto the

synthesized LDO. At an agitation speed of 50 rpm, the adsorption capacity was measured as 29.56 mg/g, while at 100 rpm, it increased to 31.94 mg/g (Figure 30C). Further increase in agitation speed to 150 rpm resulted in a slight decrease in adsorption capacity to 31.20 mg/g. At 200 rpm and 250 rpm, the adsorption capacities were measured as 31.10 mg g^{-1} and 30.58 mg g^{-1}, respectively. Similarly, the removal efficiency of fluoride ions demonstrated a similar pattern. At 50 rpm, the removal efficiency was 73.90%, which increased to 79.85% at 100 rpm. At 150 rpm, the removal efficiency slightly decreased to 78.01%. At 200 rpm and 250 rpm, the removal efficiencies were measured as 77.76 and 76.45%, respectively. These findings might be ascribed to the accessibility of active sites on the surface of CNAO, mass transfer limitations, and the level of agitation-induced mixing. Lower agitation speeds may result in slower diffusion of fluoride ions to the active sites, leading to relatively lower adsorption efficiencies. Conversely, higher agitation speeds enhance the diffusion process, thereby improving the adsorption efficiencies. It is worth noting that excessive agitation can potentially cause desorption of adsorbed fluoride ions from the surface of CNAO-0.2 which may be due to attrition of the adsorbent and mechanical impacts at high agitation speed. This detachment can subsequently reduce the overall adsorption efficiency, as observed at the highest agitation speed of 250 rpm (Yagub *et al*., 2012).

Effect of Coexisting Ions: The effect of coexisting ions which are commonly found in drinking water, namely SO_4^{2-}, NO_3^-, and Cl^-, on the adsorption of F^- by Ce^{4+}-doped Ni-Al LDO was also studied in the present work. The removal efficiencies of F^- were investigated at different concentrations of these coexisting ions, namely 5, 10, and 20 ppm, in the presence of 20 mg/L F^- (Figure 30C). The results showed that the presence of coexisting ions influenced the removal efficiency of F^-. In the presence of SO_4^{2-} ions at concentrations of 5, 10, and 20 ppm, removal efficiencies of 74.3, 75.72 and 76.18% were obtained, respectively. Similarly, in the presence of NO_3^- ions at concentrations of 5, 10, and 20 ppm, removal efficiencies of 73.90, 73.50 and 69.03% were obtained, respectively. Finally, in the presence of Cl^- ions at concentrations of 5, 10, and 20 ppm, removal efficiencies of 73, 71.08 and 66.97% were obtained, respectively. These results indicated that the coexisting ions can slightly affect the removal efficiency of fluoride, with varying degrees of influence depending on the specific ion. Ce^{4+} can interact differently with various anions depending on the solution's pH. The pH influences the speciation of the anions and the availability of Ce^{4+} for interaction (Kong *et al*., 2019).

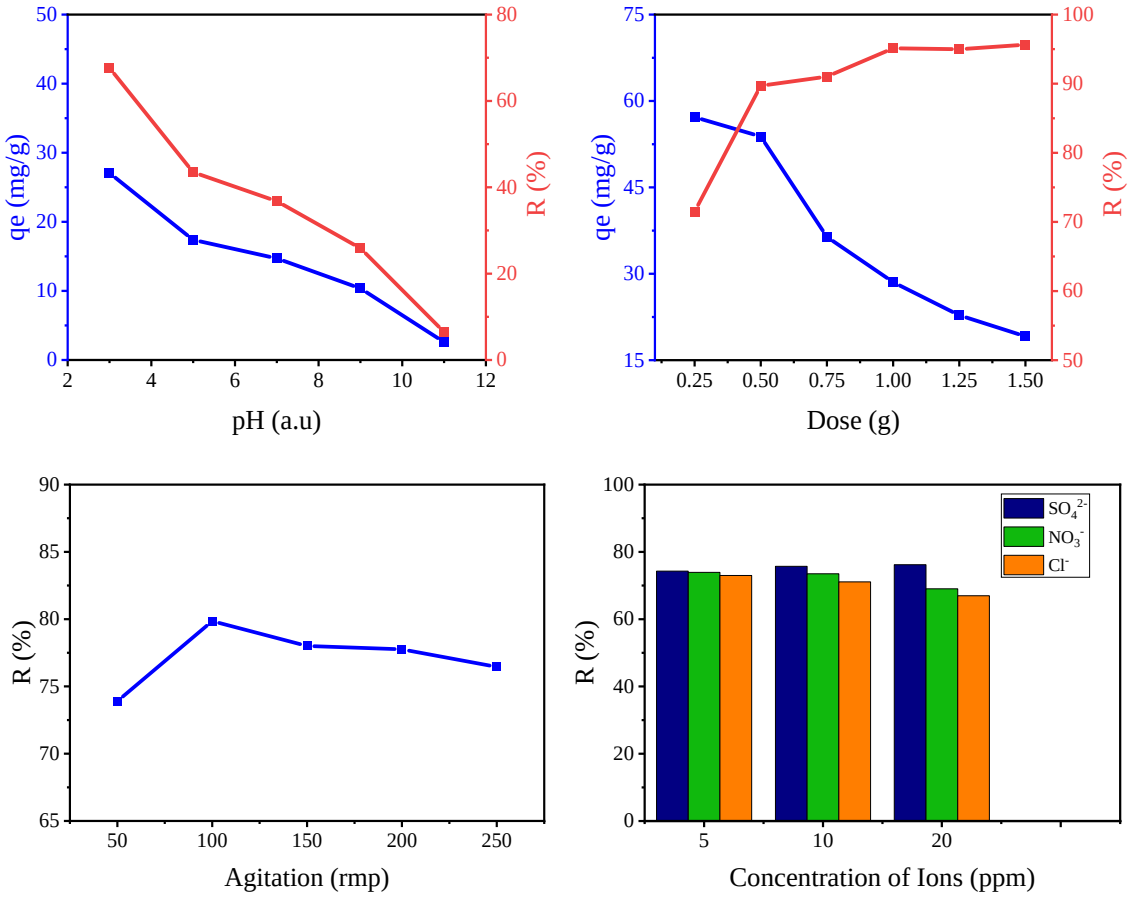

Figure 30. Graphs indicating influence of A) pH, B) Dose, C) Agitation and D) coexisting ions on fluoride adsorption performance of CNAO-0.2

4.8.3 Investigation of Fluoride Adsorption Kinetics

The adsorption kinetics of fluoride onto CNAO-0.2 was examined by varying the contact time (15 30, 45, 60, 90 and 120 min) at initial F^- concentration of 20 mg L^{-1}, pH of 3 and temperature of 25 °C. To analyze the kinetics of the adsorption process, nonlinear pseudo-first order (PFO) and pseudo-second order (PSO), were employed (Table 18 and Figure 31A). The results suggested that both methods (PFO and PSO) can predict the experimental data reasonably well.

For PFO model, q_e was determined to be 30.37 mg/g. Furthermore, the rate constant (K_1) associated with the PFO model was found to be 0.22, indicating the speed at which the adsorption process occurs faster than that of PSO (Table 18). The goodness of fit for this model was assessed using R^2, yielding an impressive value of 0.99. This high R^2 value

suggested that PFO model effectively described the adsorption kinetics of F^- onto CNAO-0.2.

Similarly, q_e obtained from the PSO model was determined to be 30.54 mg/g, indicating a slight increase compared to the PFO model (Table 18). The rate constant (K_2) associated with the PSO model was found to be 0.07, suggesting a relatively slower adsorption process compared to the PFO model. The PSO model's goodness of fit was evaluated using the R^2, which yielded a value of 0.99, indicating a strong correlation between the model and the experimental data (Figure 31A). In conclusion, the results demonstrated that both models were able to describe the adsorption process effectively, as evidenced by high R^2 values. This means that the process is influenced by both mass transfer and chemical reaction that takes place between the adsorbent and adsorbate (Liu *et al*., 2019).

Table 18. Outputs of kinetics models fitted to results from adsorption of fluoride onto CNAO-0.2

Types of models	Parameters and values					
PFO	q_e (mg/g)	30.37	K_1 (1/min)	0.22	R^2	0.99
PSO	q_e (mg/g)	30.54	K_2 (g/mg min)	0.07	R^2	0.99

4.8.4 Isotherms of Fluoride Adsorption

The adsorption behavior of fluoride onto CNAO-0.2 was investigated by examining the adsorption isotherms at various initial F^- concentrations of 10, 20, 30, 40, 50 and 60 ppm. The data was analyzed using different nonlinear isotherm models: Freundlich, Langmuir and Temkin (Table 19 and Figure 31B). The results suggested that the Freundlich model was the best-fitting model, as it has the highest R^2 value.

Table 19. Outputs of isotherm models fitted to results from adsorption of fluoride onto CNAO-0.2

Types of models	Parameters and values					
Freundlich	K_f ((mg/g) $(L/mg)^{1/n}$)	17.75	N (dimension-less)	2.08	R^2	0.999
Langmuir	q_{max} (mg/g)	132	K_L (L/mg)	0.07	R^2	0.970
Temkin	K_T (J/mg)	0.92	B_T (L/mg)	92.9	R^2	0.962

The high R^2 values obtained indicated a satisfactory match of the experimental data to Freundlich model. From the Freundlich isotherm model, the obtained parameters were K_f = 17.75 and N = 2.08, with a high coefficient of determination (R^2) of 0.999 (Table 19) suggested that F^- adsorption onto CNAO-0.2 was favorable and followed a heterogeneous process (Vigdorowitsch *et al*., 2021).

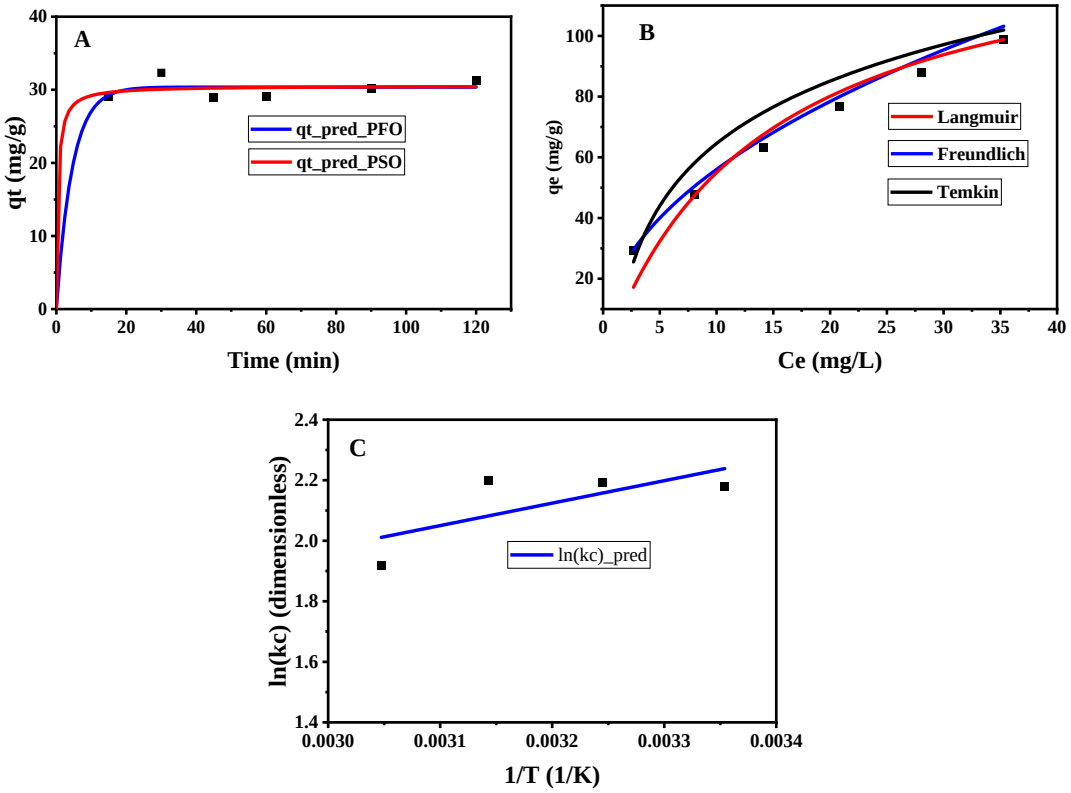

Figure 31. Graphs of A) kinetics, B) isotherms and C) van't Hoff fitted to fluoride adsorption by CNAO-0.2

4.8.5 Thermodynamics of Adsorption of Fluoride

The consequence of temperature on the adsorption of fluoride onto CNAO-0.2 was investigated in this study. The thermodynamic parameters, including the Gibbs free energy change (ΔG), dimensionless equilibrium constant (Kc), enthalpy change (ΔH) and entropy change (ΔS), were estimated using van't Hoff fitting based on the equilibrium constants obtained from the adsorption experiments (Figure 31C). The data at different temperatures are summarized in Table 20.

Table 20. Thermodynamic outputs of fluoride adsorption onto CNAO-0.2 at various temperatures

Kc (dimensionless)	T (°C)	ΔG (KJ/mol)	ΔH (KJ/mol)	ΔS (J/mol)
8.59	25	-5.33	-5.46	0.13
8.97	35	-5.62		
9.01	45	-5.81		
6.81	55	-5.23		

The ΔG with negative values indicated that F^- adsorption onto CNAO-0.2 is spontaneous at the studied temperatures. The magnitude of ΔG suggested the thermodynamic favorability of the adsorption and that CNAO-0.2 has a high affinity for fluoride ions. The negative ΔH values indicated the adsorption process is exothermic, implying that the adsorption is driven by heat release. The positive ΔS values suggested an increase in the randomness of the system during the adsorption course, possibly due to the rearrangement of F^- or changes in the adsorbent's surface as it interacts with F^- (Bering et al., 1972).

4.8.6 Investigation of Regeneration and Reusability

A series of regeneration cycles were conducted to evaluate the reusability performance of CNAO-0.2 nanomaterial for adsorbing fluoride from aqueous solutions. The experimental setup involved using 0.5 g L^{-1} of CNAO-0.2 nanomaterial as adsorbent and an initial fluoride amount of 20 mg L^{-1}. The removing efficiencies for the first six regeneration cycles were determined to be 89.39, 88.33, 87.02, 85.23, 83.39, 78.9 and 75.71%, respectively (Figure 32). A similar regeneration study was previously reported by Sarma et al. (Sarma and Rashid, 2018)

These results indicated that CNAO-0.2 nanomaterial possessed excellent regeneration capabilities, allowing for repeated usage without significant loss in adsorption efficiency. The high removal efficiencies obtained in the subsequent cycles suggested that the nanomaterial maintained its adsorption capacity even after multiple regeneration cycles. This finding was of great significance for practical applications, as it highlighted the potential of CNAO-0.2 nanomaterial as a cost-effective and sustainable adsorbent for F^- removing from aqueous solutions.

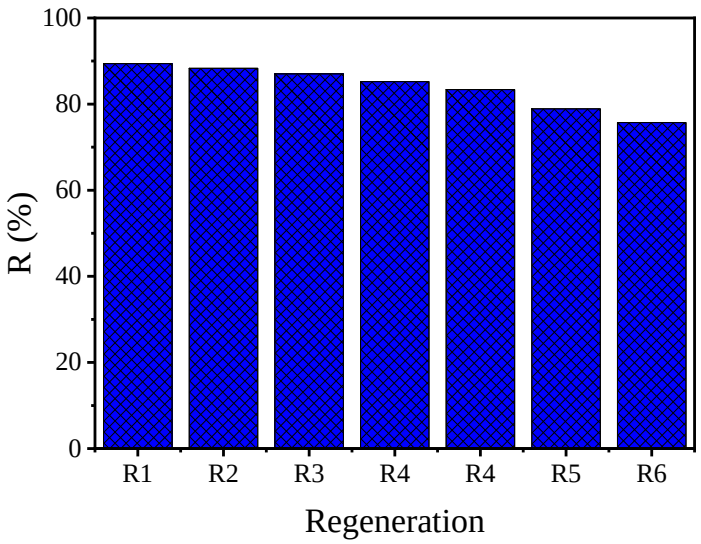

Figure 32. Graph showing reusability performance of CNAO-0.2 for fluoride adsorption

4.9 Expected Mechanisms in Fluoride Adsorption-Post-Adsorption Characterizations

There are a number of potential mechanisms that could account for the adsorption process based on the ATR FT-IR and XRD analysis of the used adsorbent (Figure 33). The observed changes in the FT-IR spectrum and peak intensity of XRD patterns following the fluoride adsorption by CNAH-0.05 LDH can potentially indicate that there is a change that can aid in proposing the mechanisms. La-doped Li/Al LDH showed similar outcomes (Cai *et al*., 2018b). A few methods, including surface complexation, ion exchange and hydrogen bonding, may be proposed based on the results of ATR-IR and XRD to aid the mechanisms of fluoride ion adsorption onto CNAH-0.05 LDH.

The disappearance of OH^- (3391 cm^{-1}) and H_2O (1620 cm^{-1}) peaks suggested that surface complexation reactions may occurred during the adsorption process. The F^- likely formed complexes with surface hydroxyl groups (OH^-) present on the LDH surface, such as HF or H_2O-F. These surface hydroxyl groups might act as binding sites for fluoride, leading to the formation of surface complexes. The formation of fluoride surface complexes might be described by the Lewis acid-base interaction, where the F^- ions acted as Lewis bases and the surface hydroxyl groups acted as Lewis acids. This interaction involved the donation of electron pairs from fluoride ions to vacant sites on the LDH surface, resulted in the formation of stable surface complexes. Additionally, F^- can form surface complexes with Ce^{4+} as $Ce^{4+} + 2F^- \rightarrow CeF_2^{2+}$. This formation was deduced from the absence of a peak at 992 cm^{-1}

attributed to vibration of Ce-O-Ce in FT-IR (Figure 33A). The formation of the CeF_2^{2+} complex reduced the amount of free F^- in the solution, contributing to the defluoridation process (Kong *et al*., 2019). Similarly, from the XRD pattern, changes in peak intensity of LDH upon F^- adsorption were observed particularly for the (003), (110), and (113) peaks, leading to intensified peaks (Figure 33B). This implied, that when F^- ions occupy space between the LDH layers (interlayer space), it might cause an expansion in the d-spacing (distance between layers) corresponding to the (003) reflection. This can lead to an increase in the intensity of the (003) peak (Mullick and Neogi, 2019; Sarma and Rashid, 2018).

Another possible mechanism was ion exchange, where the fluoride ions replaced other anions (such as hydroxide or carbonate ions) present in the LDH on the surface or in the interlayer. The absence of FT-IR peaks corresponding to OH^- and CO_3^{2-} (1357 cm^{-1}) in the spectrum indicated the release of these ions upon the adsorption of fluoride. This suggested that the fluoride ions were exchanged with other anions present on the LDH surface or in the interlayer. The CNAH-0.05 LDH possessed a layered structure with interlayer anions, such as CO_3^{2-} and OH^- ions. The fluoride ions might potentially replace these interlayer anions through an ion exchange mechanism. During the adsorption process, the fluoride ions might exchange places with the CO_3^{2-} and OH^- ions in the interlayer spaces of the LDH. This ion exchange process occurred due to the difference in affinity between F^- and other ions for the LDH surface (Liu *et al*., 2019).

The absence of IR peaks associated with OH^- in the spectrum of LDH might also suggest the involvement of hydrogen bonding in the adsorption mechanism. Fluoride ions might form hydrogen bonds with the hydroxyl groups on the LDH surface. This type of interaction might contribute to the adsorption of F^- and the subsequent changes observed in the ATR-IR spectrum (Ren *et al*., 2021).

The presence of Ce^{4+} ions in the LDH structure possibly might have a role in the adsorption mechanism. The F^- might undergo ligand exchange reactions with the Ce^{4+} ions, forming Ce-F complexes. This interaction might be responsible for the changes observed in the ATR-IR spectrum, indicating the existence of fluoride on LDH surface after adsorption (Kong et al., 2019). From the XRD investigation, the (110) and (113) reflections might have also been affected by the adsorption process. The changes in these peaks could be related to distortions

within the metal cation layers as result of F^- adsorption (Mullick and Neogi, 2019; Sarma and Rashid, 2018).

The layered structure of CNAH-0.05 nanosheets provided a large surface area for fluoride adsorption. The mechanism might involve the interaction between F^- and the active sites of the LDH surface (Ren *et al*., 2021).

LDH surface sites + $F^- \rightarrow$ LDH-F (Surface adsorption)

The incorporation of Ce^{4+} ions into the LDH lattice enhanced the surface reactivity and increased the binding sites for fluoride ions.

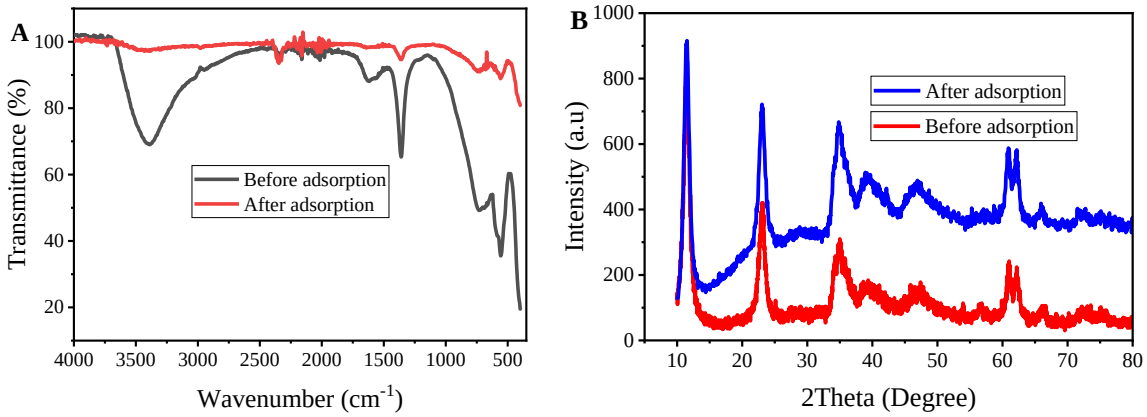

Figure 33. A) ATR FT-IR and B) XRD of CNAH-0.05 before and after adsorption of fluoride

The adsorption of F^- onto CNAO-0.2 is a complex process that involves multiple factors, including the electrostatic interaction between the positively charged ions (Ni^{2+}, Al^{3+} and Ce^{4+}) and the negatively charged F^- ions, the formation of complexes between positive ions and F^-, and the memory-effect/reconstruction of LDO to LDH (Cai *et al*., 2018a; He *et al*., 2019).

The electrostatic interaction between F^- ions and CNAO-0.2 was indeed the primary driving force for adsorption. The positively charged metal cations (Ce^{4+}, Ni^{2+} and Al^{3+}) in the LDO structure create an electrostatic field that pulls in the negatively charged fluoride ions (F^-) from the solution. The strength of this interaction depends on the pH of the solution. At low pH, the surface of the LDO is protonated, which increases the positive charge of the surface and strengthens the interaction. As the pH increases, the surface of LDO becomes deprotonated, which reduces their positive charge and weakens the electrostatic interaction with F^- (Cai *et al*., 2018a; He *et al*., 2019).

The formation of complexes between CNAO-0.2 and F^- was another important mechanism in the adsorption of F^- onto CNAO-0.2. The complexes were formed when a ligand, such as F^-, shares an electron pair with a metal ion, such as Ce^{4+} and Al^{3+}. The formation of complexes was favored at low pH, where the positive ions were more likely to be hydrated. Hydrated ions have a larger radius than anhydrous ions. This means that the hydrated cations are more likely to be able to form complexes with F^- ions. These complexes can help to hold the F^- ions onto the surface of the material (He *et al*., 2019). The complex formation can be explained in terms of Lewis acid-base interaction between positive ions of CNAO-0.2 and F^-. This was because Ce^{4+} is a Lewis acid, which has an empty orbital that can accept electron pairs, whereas F^- is a Lewis base, which means it has a lone pair of electrons that it can donate.

The reconstruction of the CNAO-0.2 into a hydrotalcite-like structure during adsorption might also contributed to the high adsorption capacity. Fluoride ions were strongly adsorbed and intercalated into the interlayers of the reconstructed hydrotalcite-like sheets, enhancing the overall adsorption capacity (Kong *et al*., 2019).

ATR FT-IR study provided evidence to support the proposed mechanisms for F^- adsorption by CNAO-0.2 as the emergence of intensified peaks between 2400 to 1500 cm^{-1}, and a new peak at around 616 cm^{-1} in the exhausted material (Figure 34).

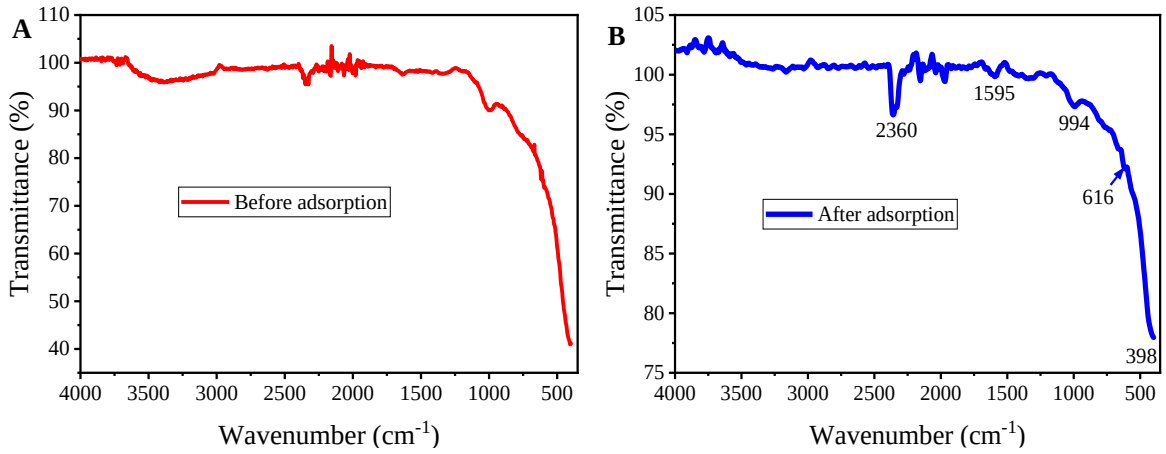

Figure 34. ATR-IR CNAO-0.2 A) before F^- adsorption and B) after F^- adsorption

The presence of intensified peaks in the spectrum of the exhausted material compared to the pristine material indicated changes in the chemical environment of the material. These

changes might be due to the interaction between the F^- ions and the surface of the CNAO-0.2. Additionally, the presence of new peaks suggested the formation of new chemical species as a result of the adsorption process (Cai *et al.*, 2018a; He *et al.*, 2019).

4.10 CO_2 Capture from Simulated Flue Gas by Mn^{2+} Doped Ni-Al LDOs

4.10.1 CO_2 Adsorption Performance and Breakthrough Curves of MNAOs

The breakthrough curve was employed to compare the CO_2 adsorption capacities of MNAOs. The breakthrough curve was plotted from the outlet CO_2 concentration versus time, measured utilizing the experimental setup shown in Figure 5. Figure 35 shows that MNAO-0.2 has a higher adsorption capacity than the others, as it took a longer time to reach the breakthrough point. The breakthrough point is when the outlet percentage reaches 10% of the inlet percentage (13%) and this occurred at around 13 min for MNAO-0.2. After the breakthrough point, the outlet concentration kept increasing until it reached a maximum value of 90% of the inlet at 28 min. This is the saturation point, which indicates that the adsorbent is almost fully saturated. The service time, which is the difference between the saturation time and the breakthrough time, reflected the duration of effective adsorption. This might be ascribed to the surface area of MNAO-0.2 presented in Table 5.

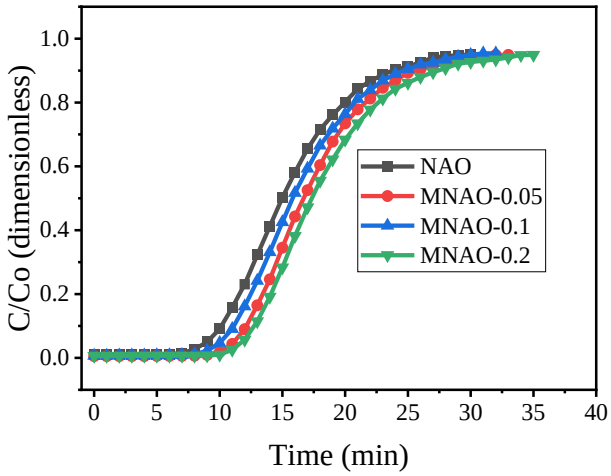

Figure 35. Breakthrough curves of CO_2 adsorption on MNAOs at 20 mL/min flow rate of CO_2, 31 ^oC, 14.15 psi, and 10 cm packed-bed height

The data in Table 21 further supported this observation. The adsorption performance of MNAO-0.2 was higher than the others, as indicated by the values of breakthrough capacity

(q_b), saturation capacity (q_s), and equilibrium capacity (q_e). q_b (mmol/g) represented the amount of CO_2 adsorbed by the adsorbent at the beginning of a breakthrough. MNAO-0.2 has a higher q_b value of 7.45 mmol/g, showing that it has initially adsorbed a larger quantity of CO_2. q_s (mmol/g) represented the maximum amount of CO_2 that can be adsorbed by the adsorbent. MNAO-0.2 has also a higher q_s value of 10.69 mmol/g compared to others, demonstrating that it has a higher overall CO_2 adsorption performance. q_e (mmol/g) represented the amount of CO_2 adsorbed by the adsorbent at equilibrium. MNAO-0.2 again outperformed the rest in terms of CO_2 adsorption performance, with a q_e value of 10.93 mmol/g. MNAO-0.2's better performance might be ascribed to its high BET surface area (Table 5). Similar investigations were previously reported in the literature (Bhatta *et al*., 2016; Raganati *et al*., 2019; Yang *et al*., 2019).

Therefore, the data indicated that MNAO-0.2 exhibited better CO_2 adsorption performance and was considered in investigating other parameters. Furthermore, MNAO-0.2 has a longer breakthrough time, suggesting its potential for effective CO_2 capture applications. In addition to the most common contributing factors such as surface entrapments and metal-CO_2 interactions, oxygen vacancies and redox pairs (Mn^{2+}/Mn^{3+}) are likely key contributors to the enhanced CO_2 capture by MNAO-0.2 where oxygen vacancies acted as adsorption sites, while redox pairs facilitated CO_2 binding (Wang *et al*., 2022; Xu *et al*., 2021; Zhang *et al*., 2020).

Table 21. CO_2 adsorption efficiencies of MNAOs

Adsorbents	q_b (mmol/g)	q_s (mmol/g)	q_e (mmol/g)	Column efficiency (%)
NAO	2.48	5.99	6.16	41.40
MNAO-0.05	6.49	9.81	10.0	66.16
MNAO-0.1	5.47	8.90	9.07	61.46
MNAO-0.2	7.45	10.69	10.93	69.69

4.10.2 Breakthrough Curve Fitted with Fixed-Bed Models

The CO_2 adsorption capacity of MNAO-0.2 was investigated in this study. The breakthrough curve of CO_2 adsorption was also analyzed using three different fixed-bed models. The models used are Bohart-Adams, Clark, and Yoon-Nelson. The experimental data was fitted

with these models using CAVS software, which considered the operational parameters of the packed column adsorption process, such as the CO_2 inlet concentration, the flow rate, the column dimensions, the adsorbent mass, and the porosity (Figure 36).

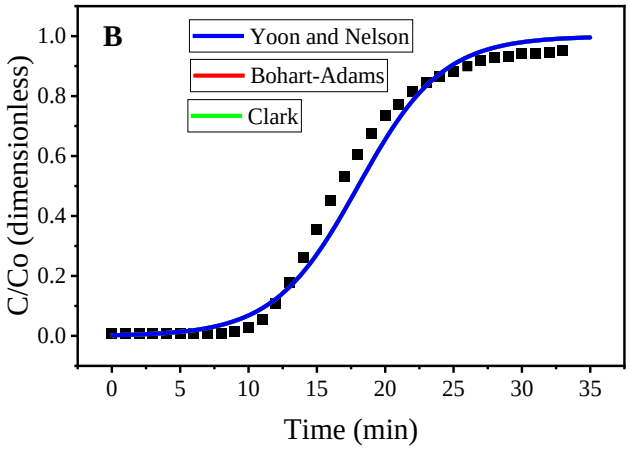

Figure 36. Graph showing the fixed-bed models fitted to the best performed (MNAO-0.2)

Table 22 shows the values of the parameters and the coefficient of determination (R^2) for each model.

Table 22. Fixed-bed models fitted with the CO_2 adsorbed onto MNAO-0.2

Fixed-bed Models	Parameters	Values
Bohart-Adams	kab (mL/(mg.min))	0.025
	Nab (mg/mL)	0.23
	R^2	0.990
Clark	rck (1/min)	0.32
	Ack (dimensionless)	346.20
	R^2	0.990
Yoon and Nelson	tal (min)	18.01
	kyn (1/min)	0.32
	R^2	0.990

According to the results in Table 22, all the models had a similar R^2 value of 0.990, indicating a good fit of models to the experimental results. The maximum amount of CO_2 that can be adsorbed per unit mass of adsorbent (saturation capacity, Nab) of MNAO-0.2 suggested that it has a higher adsorption capacity for CO_2. The rate of adsorption per unit time of MNAO-

0.2 was generally lower, implying lower adsorption kinetics for CO_2. The higher dimensionless parameter (a measure of the affinity between the adsorbent and the adsorbate) of Clark model indicated a stronger affinity of MNAO-0.2 for CO_2. The breakthrough time (the time when the outlet percentage of CO_2 reaches 50% of the inlet percentage) was longer as to the Yoon-Nelson model, reflecting that the adsorbent can saturate more CO_2. Therefore, the agreement between experimental data and model fitting further solidified that the material is promising for CO_2 capture (Patel, 2019).

4.10.3 ATR FT-IR of CO_2 Adsorbed onto MNAO-0.2

ATR FT-IR spectroscopy was used to explore the CO_2 adsorbed onto MNAO-0.2. ATR FT-IR is a technique that uses ATR crystal to measure the IR spectra of thin layers of adsorbed molecules on a solid surface. The IR spectra can provide information about the chemical bonds, functional groups, and molecular vibrations of the adsorbed species (Mudunkotuwa et al., 2014).

According to the results from Figure 37, the ATR FT-IR spectra of CO_2 adsorbed onto MNAO-0.2 showed different features from the un-adsorbed one that indicated the presence of different types of CO_2 species on the surface of LDO. The IR spectra showed four peaks at 2327, 1600, 1109 and 620 cm^{-1}. As stated in the literature (Hammerli *et al*., 2021; Qin *et al*., 2021), the new peak at 2327 cm^{-1} corresponds to linearly adsorbed CO_2 on the metal sites of the adsorbent, such as Ni, Mn, or Al. The peak at 1600 cm^{-1}, which is stronger after CO_2 capture compared to before, indicated the presence of bidentate carbonate species. These species likely formed from the reaction of CO_2 with metal oxides or surface hydroxyl groups on the adsorbent. These hydroxyl groups were likely introduced by ambient humidity in the column. The increased intensity of the peak at 1109 cm^{-1} after CO_2 adsorption suggested the formation of monodentate carbonate species. The new peak at 620 cm^{-1} is related to bulk carbonate species, which are formed by the diffusion of CO_2 into the lattice of the adsorbent where the carbonate is bonded to more than a single metal. This species is considered more stable than bidentate carbonates, which can be removed by heating to high temperatures (Hammerli *et al*., 2021; Qin *et al*., 2021).

The presence of CO_2 species, indicated by intensified and newly appeared peaks in ATR FT-IR spectra taken after the adsorption test, suggested that the LDO has a high CO_2 adsorption

capacity. The doping of Mn^{2+} might enhance CO_2 adsorption by creating more oxygen vacancies and basic sites on the surface of the LDO at different degrees (Cavani *et al*., 1991; Mudunkotuwa *et al*., 2014; Qin *et al*., 2021). Doping LDO with Mn^{2+} introduced foreign cations (Mn^{2+}) into the lattice structure, creating a charge imbalance as Mn^{2+} has a larger ionic radius than Ni^{2+}. This size difference can cause distortions in the LDO lattice, affecting the overall charge distribution. To compensate for this charge imbalance, lattice oxygen can be removed or migrated, by forming oxygen vacancies. The presence of oxygen vacancies might act as favorable sites for CO_2 adsorption, providing electron density for CO_2 activation. Additionally, migrating oxygen ions, when reaching the surface, might act as surface basic sites due to their negative charge, potentially interacting with and attracting CO_2 molecules (Aziz *et al*., 2020; Garcés-Polo *et al*., 2018; Zhu *et al*., 2020).

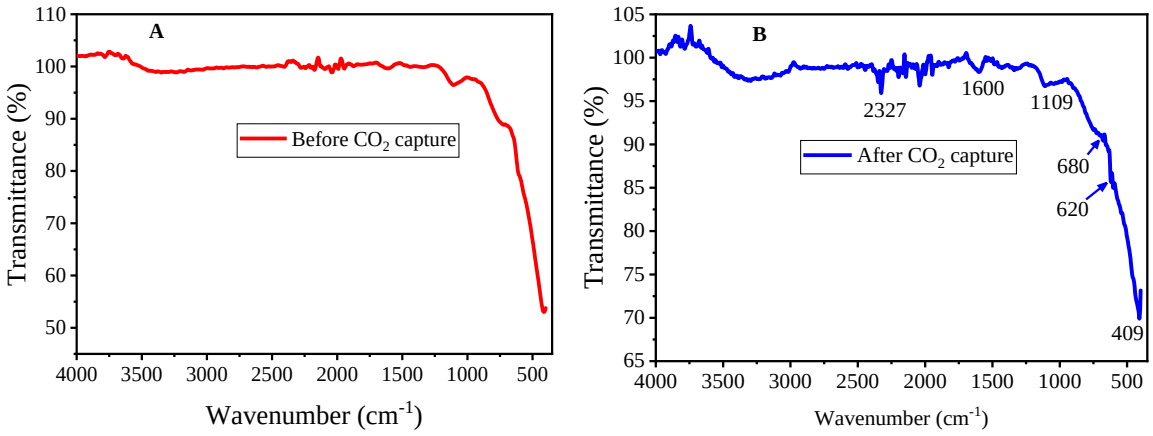

Figure 37. ATR FT-IR of MNAO-0.2 before and after adsorbing CO_2

4.10.4 Impact of Temperature on Regeneration of CO_2 Saturated MNAO-0.2

The regeneration efficiency of the material was studied at different temperatures as presented in Table 23 in terms of the impact of regeneration temperature on the CO_2 saturation capacity of MNAO-0.2.

Table 23. CO_2 saturation capacities of MNAO-0.2 after regeneration at different temperatures

Adsorbent	Temperature (°C)	CO_2 saturation capacity (mmol/g)
MNAO-0.2	200	4.38
	300	5.32
	400	9.72

The CO_2 saturation capacity of MNAO-0.2 increased from 4.38 mmol/g at 200 °C to 9.72 mmol/g at 400 °C regeneration temperature. The results indicated that the saturation capacity of the LDO increased with regeneration temperature, likely due to the higher regeneration temperature removing more surface contaminants and exposing more active sites (Hack *et al.*, 2022). This can also be assured from Figure 38 which indicated that the saturation time increased with increasing regeneration temperature. Based on these findings, the repeated regeneration performances of MNAO-0.2 were studied at 400 °C.

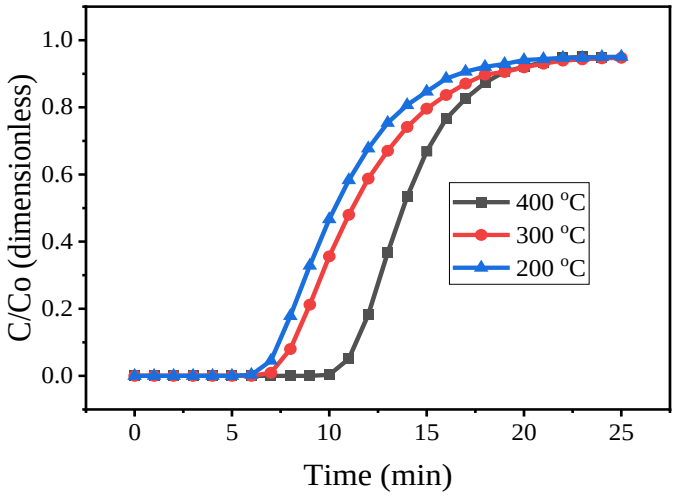

Figure 38. Effect of temperature on regeneration of CO_2-captured MNAO-0.2

4.10.5 Regeneration and Reusability Performance of MNAO-0.2

Table 24 shows the CO_2 saturation capacities of exhausted MNAO-0.2 after multiple regeneration cycles at 400 °C.

Table 24. CO_2 saturation capacities of MNAO-0.2 after multiple regeneration cycles at 400 °C

Adsorbent	Regeneration cycle, R	CO_2 saturation capacity (mmol/g)
MNAO-0.2	R_1	9.65
	R_2	6.77
	R_3	4.69
	R_4	2.77

The CO_2 saturation capacity of MNAO-0.2 decreased from 9.65 mmol/g to 2.77 mmol/g after four regeneration cycles. The results indicated that the saturation capacity of the material decreased with increasing number of regeneration cycles, likely due to damage caused by the regeneration process, which reduced the number of available adsorption sites (Bustillos *et al*., 2020). Similarly, Figure 39 showed that the saturation time decreased with increasing regeneration cycles. Despite the decrease in saturation capacity, MNAO-0.2 still exhibited promising CO_2 capture performance and is therefore a promising material for large-scale CO_2 capture applications.

It is important to note that the regeneration process is a crucial factor in the long-term performance of CO_2 capture materials. It provided information on the cost of materials effectiveness and sustainability. The regeneration process must be able to remove all of the adsorbed CO_2 without damaging the material (Kurlov *et al*., 2020). The results of this study suggested that MNAO-0.2 is stable under multiple (four) regeneration cycles.

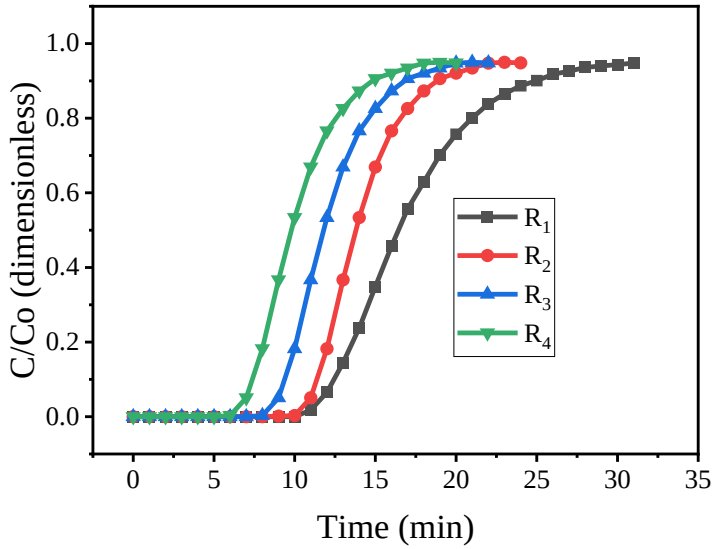

Figure 39. Multiple regeneration performance of CO_2-captured MNAO-0.2 at 400 ^oC

4.11 CO_2 Capture by Ce^{4+} Doped Ni-Al LDOs

4.11.1 CO_2 Adsorption Performance and Breakthrough Curves of CNAOs

The breakthrough curves (Figure 40) were employed to compare the CO_2 adsorption capacities of the different CNAOs. The curves are plotted from the outlet CO_2 concentration versus time. The data were generated using the experimental setup shown in Figure 5.

Among the studied materials, CNAO-0.2 exhibited the most favorable performance. Its breakthrough point occurred at around 17 min, significantly later than other CNAOs. This suggested that CNAO-0.2 can capture CO_2 for a longer duration before saturation. Furthermore, the curve showed a steeper rise in the outlet concentration after the breakthrough point, indicating a rapid saturation compared to other CNAOs. This observation aligned with the shorter service time (difference between saturation and breakthrough times) observed for CNAO-0.2. After the breakthrough point, the outlet concentration kept increasing until it reached a maximum value of 90% of the inlet at 30 min. This is the saturation point, which indicates that the adsorbent is almost fully saturated.

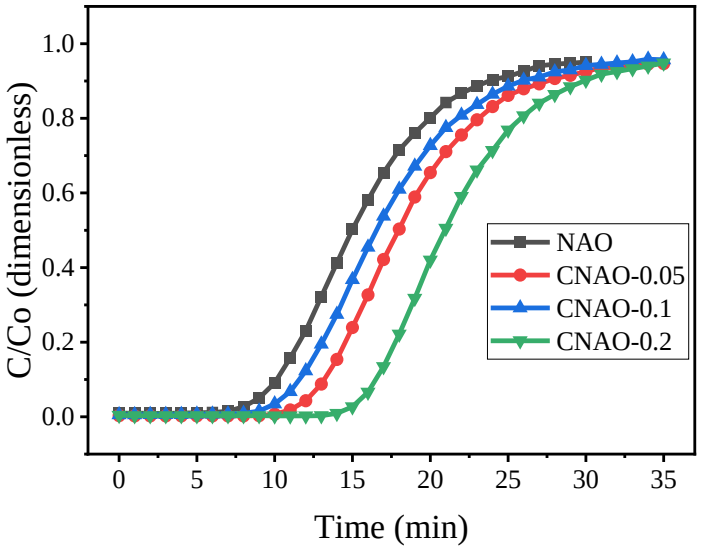

Figure 40. Breakthrough curves of CO_2 adsorption on CNAOs at 20 mL/min flow rate of CO_2, 31 ^oC, 14.15 psi, and 10 cm packed-bed height

Table 25 further corroborates the findings from the breakthrough curves. The Table presented key performance metrics. CNAO-0.2 has the highest q_b value (11.45 mmol/g), indicating its superior ability to capture CO_2 initially. CNAO-0.2 again demonstrated the highest q_s value (14.09 mmol/g), highlighting its overall superior CO_2 adsorption performance. CNAO-0.2 maintains its lead with the highest qe value (14.16 mmol/g). CNAO-0.2 exhibited the highest column efficiency (81.26%), indicating that it utilized the packed bed more effectively for CO_2 capture.

Table 25. CO_2 adsorption efficiencies of CNAO-0.2

Adsorbents	q_b (mmol/g)	q_s (mmol/g)	q_e (mmol/g)	Column efficiency (%)
NAO	2.48	5.99	6.16	41.40
CNAO-0.05	7.52	11.16	11.4	67.38
CNAO-0.1	6.42	9.65	9.98	66.53
CNAO-0.2	11.45	14.09	14.21	81.26

The combined analysis of the breakthrough curves and quantitative data showed that CNAO-0.2 is the most promising candidate for CO_2 capture among the studied materials. Its superior performance can be attributed to various factors, such as the presence of pores and cavities within the material's structure allowing for CO_2 molecules to be physically trapped (Figure 18), specific interactions between the metal cations within CNAO-0.2 and CO_2 molecules enhance the adsorption process and these additional factors, particularly prevalent in CNAO-0.2, play a crucial role. The BET characterization of CNAO-0.2 also showed a high surface area (Table 5). Oxygen vacancies act as additional adsorption sites, while redox pairs (Ce^{4+}/Ce^{3+}) facilitate stronger binding of CO_2 molecules (Wang *et al*., 2022; Xu *et al*., 2021; Zhang *et al*., 2020).

4.11.2 Breakthrough Curve Fitted with Fixed-Bed Models

This study investigated the CO_2 adsorption capacity and selectivity of a novel material, CNAO-0.2. The breakthrough curve, which depicts the change in CO_2 concentration at the outlet of the adsorption column over time, was analyzed using three different fixed-bed models: Bohart-Adams, Clark, and Yoon-Nelson.

The experimental data was fitted to each model using CAVS software, considering relevant operational parameters like inlet CO_2 concentration, flow rate, column dimensions, adsorbent mass, and porosity. All three models exhibited a high coefficient of determination (R^2) of 0.991, indicating a good fit to the experimental data (Figure 41 and Table 26). This agreement between the models and the experimental data strengthens the claim that CNAO-0.2 is promising for CO_2 capture.

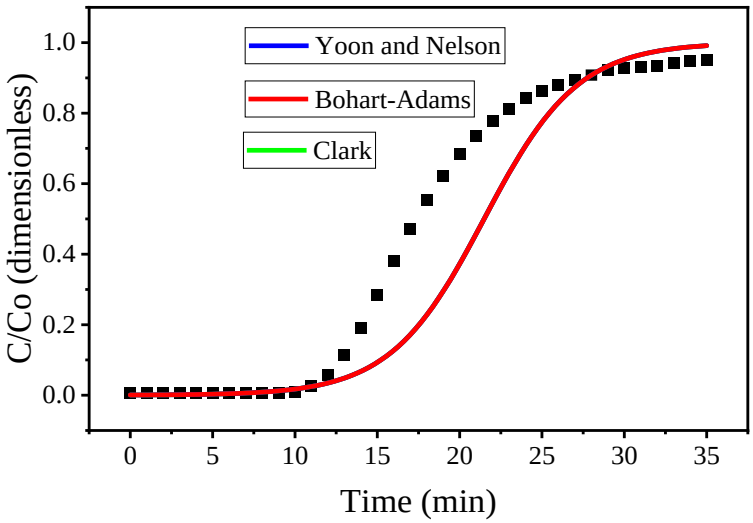

Figure 41. Fixed-bed models fitted to the best-performed CNAOs in CO_2 capturing (CNAO-0.2)

While all models displayed a good fit, analyzing the specific parameters from each model provided further insights. k_{ab} (mL/(mg.min)) parameter of Bohart-Adams model represents the mass transfer coefficient, indicating the rate at which CO_2 molecules move from the bulk fluid to the adsorbent surface. A value of 0.025 mL/(mg.min) suggested a moderate rate of mass transfer for CNAO-0.2. The Nab (mg/mL) parameter represents the maximum CO_2 adsorption capacity per unit mass of adsorbent, also known as the saturation capacity. The value of 0.24 mg/mL indicated a relatively high CO_2 adsorption capacity for CNAO-0.2 (Hu *et al.*, 2021; Patel, 2019).

The rck (1/min) parameter of Clark model represents the rate constant for the chemical reaction between CO_2 molecules and the adsorbent surface. A value of 0.33 1/min suggested a moderate rate of adsorption for CNAO-0.2. The Ack (dimensionless) parameter reflects the affinity between the adsorbent and the adsorbate (CO_2). A high value of 457.62 indicated a strong affinity of CNAO-0.2 for CO_2, suggesting favorable interactions between the material and the target gas molecules (Patel, 2019; Rafati *et al.*, 2019).

The tal (min) parameter of Yoon-Nelson represents the time to reach 50% breakthrough, reflecting the exhaustion rate of the adsorbent. A value of 18.50 min suggested a longer breakthrough time compared to other models, indicating that CNAO-0.2 can saturate more CO_2 before reaching half of the inlet concentration at the outlet. Similar to rck in the Clark model, kyn (1/min) parameter represents the rate constant for the adsorption process. A value

of 0.33 1/min aligned with the rate constant observed in the Clark model (Patel, 2019; Rafati *et al*., 2019).

Table 26. Fixed-bed models fitted with the CO_2 adsorbed onto CNAO-0.2

Fixed-bed Models	Parameters	Values
Bohart-Adams	kab (mL/(mg.min))	0.025
	Nab (mg/mL)	0.24
	R^2	0.991
Clark	rck (1/min)	0.33
	Ack (dimensionless)	457.62
	R^2	0.991
Yoon and Nelson	tal (min)	18.50
	kyn (1/min)	0.33
	R^2	0.991

The utilization of fixed-bed models provided valuable insights into the CO_2 adsorption performance of CNAO-0.2. While all three models showed a good fit to the experimental data, analyzing the specific parameters revealed a high CO_2 adsorption capacity, moderate rate of adsorption, and strong affinity between the material and CO_2. These findings further strengthen the potential of CNAO-0.2 as an effective adsorbent for CO_2 capture applications.

4.11.3 ATR FT-IR of CO_2 Adsorbed onto CNAO-0.2

ATR FT-IR was employed to investigate the nature of CO_2 adsorbed onto CNAO-0.2. This technique is particularly useful for analyzing thin layers of adsorbed molecules on solid surfaces, providing valuable insights into their chemical bonds, functional groups, and vibrational modes (Mudunkotuwa et al., 2014). The ATR FT-IR spectra of CO_2-adsorbed CNAO-0.2 (Figure 42) displayed distinct features compared to the un-adsorbed material, indicating the presence of various CO_2 species interacting with the LDO surface. Four distinct peaks were observed at 2345 cm^{-1}, 1599 cm^{-1}, 1109 cm^{-1}, and 614 cm^{-1}.

The peak at 2345 cm^{-1} corresponds to CO_2 molecules linearly adsorbed directly onto metal sites (Ni, Ce, or Al) of the LDO, as reported in the literature (Hammerli *et al*., 2021; Qin *et*

al., 2021). This suggested a direct interaction between CO_2 and the metal cations on the LDO surface. The peak at 1599 cm^{-1} is attributed to bidentate carbonate species. These species form through the reaction of CO_2 with surface hydroxyl groups or metal oxides present on the LDO, likely influenced by ambient humidity within the adsorption column (Yoshikawa *et al*., 2014). The peak at 1109 cm^{-1} is ascribed to monodentate carbonate species, which are generally considered more stable than their bidentate counterparts. These monodentate carbonates can be removed at higher temperatures (Hammerli *et al*., 2021; Qin *et al*., 2021). The presence of a peak at 614 cm^{-1} indicates the formation of bulk carbonate species. These species arise from the diffusion of CO_2 molecules into the LDO's crystal lattice, where the carbonate ion bonds to multiple metal cations (Hammerli *et al*., 2021; Qin *et al*., 2021).

The observation of these diverse CO_2 species, evidenced by the newly emerged peaks in the post-adsorption ATR FT-IR spectra, strongly suggested the high CO_2 adsorption capacity of the CNAO-0.2 material. Furthermore, the incorporation of Ce^{4+} might play a crucial role in enhancing CO_2 adsorption through the creation of oxygen vacancies and surface basic sites on the LDO surface, as reported in various studies (Hammerli *et al*., 2021; Qin *et al*., 2021).

Doping the LDO with Ce^{4+} introduced foreign cations into its lattice structure, disrupting the charge balance. To compensate for this imbalance, some lattice oxygen atoms are either removed or migrate, resulting in the formation of oxygen vacancies. Notably, Ce^{4+}, due to its higher positive charge, is more likely to create a higher number of oxygen vacancies compared to other dopants. These oxygen vacancies can act as favorable sites for CO_2 adsorption by providing electron density that facilitates CO_2 activation (Aziz *et al*., 2020; Garcés-Polo *et al*., 2018; Zhu *et al*., 2020). Additionally, the migration of oxygen ions toward the LDO surface creates negatively charged basic sites due to their inherent negative charge. These basic sites can potentially interact with and attract CO_2 molecules, further contributing to the overall CO_2 adsorption capacity of the Ce^{4+}-doped LDO (Aziz *et al*., 2020; Garcés-Polo *et al*., 2018; Zhu *et al*., 2020).

Overall, ATR FT-IR spectroscopy provided valuable insights into the various CO_2 species adsorbed onto the CNAO-0.2. The observed peaks suggested the presence of linearly adsorbed CO_2, bidentate and monodentate carbonates, and bulk carbonate species, indicating the material's high CO_2 adsorption capacity. The doping of Ce^{4+} is believed to enhance this

capacity by creating oxygen vacancies and basic sites on the LDO surface, offering potential avenues for further development of efficient CO_2 capture materials.

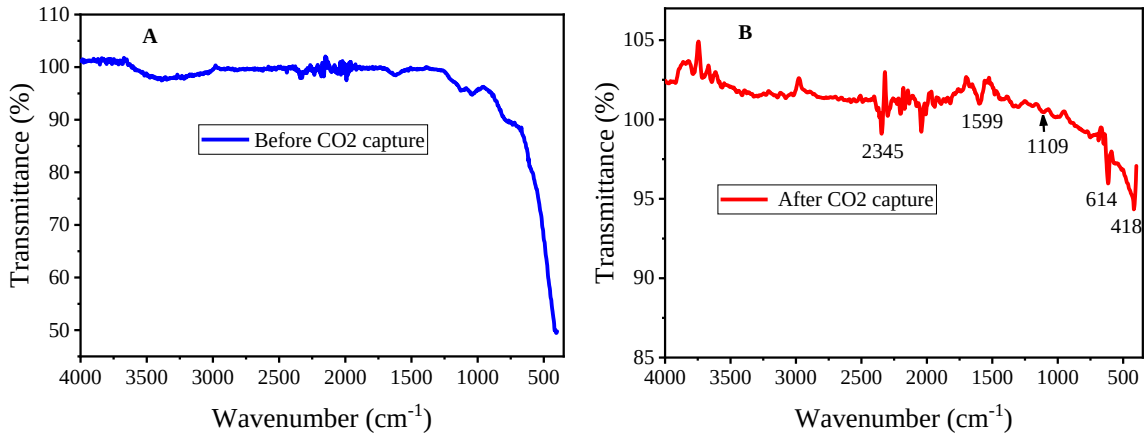

Figure 42. ATR FT-IR of CNAO-0.2 A) before and B) after adsorbing CO_2

4.11.4 Effect of Regeneration Temperature on CO_2 Capture Performance of CNAO-0.2

This section explored the impact of regeneration temperature on the CO_2 capture capacity of the synthesized LDO, CNAO-0.2. Table 27 summarizes the findings.

Table 27. CO_2 saturation capacities of CNAO-0.2 after regeneration at different temperatures

Adsorbent	Temperature (°C)	CO_2 saturation capacity (mmol/g)
CNAO-0.2	200	6.96
	300	8.74
	400	12.87

As evident from Table 26, similar to MNAO-0.2, the CO_2 saturation capacity of CNAO-0.2 significantly increased with increasing regeneration temperature. The capacity rose from 6.96 mmol/g at 200 °C to 12.87 mmol/g at 400 °C, representing an increase of almost 85%.

This observed trend can be attributed to two potential mechanisms: (1) Higher regeneration temperatures likely promote the removal of surface contaminants adsorbed onto the LDO during the CO_2 capture cycle. These contaminants can block active sites, hindering CO_2 adsorption in subsequent cycles. By removing them at higher temperatures, more active sites

become available for CO_2 capture, leading to an increased saturation capacity. (2) The elevated temperatures might also cause structural changes within the LDO, potentially leading to the expansion of pores or the creation of new ones. This can improve the accessibility of CO_2 molecules to the active sites within the LDO, further contributing to the observed increase in CO_2 saturation capacity (Hack *et al*., 2022).

Figure 43 also supports these findings by demonstrating an increase in saturation time with increasing regeneration temperature. This suggested that at higher temperatures, the LDO requires more time to reach its maximum CO_2 adsorption capacity, potentially due to the improved accessibility of active sites discussed earlier. Based on these observations, subsequent studies on the repeated regeneration performance of CNAO-0.2 were conducted at a regeneration temperature of 400 °C. This choice was made to maximize the material's CO_2 capture capacity in subsequent cycles.

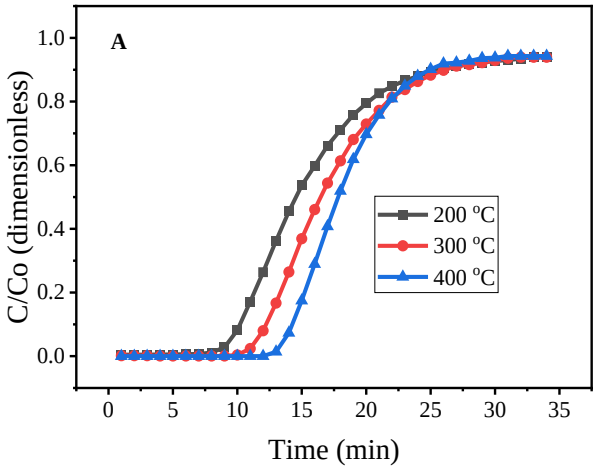

Figure 43. Effect of temperature on regeneration of CO_2-captured CNAO-0.2

4.11.5 Regeneration and Reusability Performance of CNAO-0.2

Table 28 summarizes the CO_2 capture performance of CNAO-0.2 after undergoing multiple regeneration cycles at 400 °C. The data revealed a gradual decrease in the material's CO_2 saturation capacity. This observed decline can be attributed to potential damage incurred during the regeneration process, which likely reduces the number of available adsorption sites on the material's surface (Bustillos *et al*., 2020).

Table 28. CO_2 saturation capacities of CNAO-0.2 after multiple regeneration cycles at 400 ^oC

Adsorbent	Regeneration cycle, R	CO_2 saturation capacity (mmol/g)
CNAO-0.2	R_1	12.58
	R_2	10.51
	R_3	7.96
	R_4	5.87

This phenomenon was further supported by Figure 44, which showed a corresponding decrease in the saturation time (the time required to reach maximum adsorption capacity) with increasing regeneration cycles. Despite the decrease in saturation capacity, CNAO-0.2 still exhibited noteworthy CO_2 capture performance and also showed better regeneration performance than MNAO-0.2, suggesting its potential for large-scale applications. However, it is crucial to acknowledge the regeneration process as a critical factor influencing the long-term viability of CO_2 capture materials.

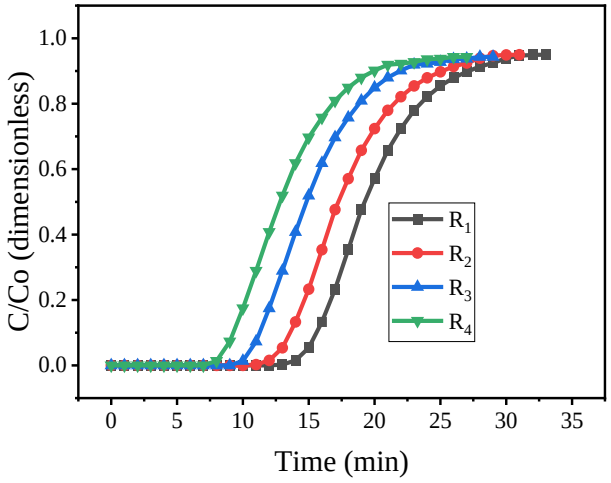

Figure 44. Multiple regeneration performance of CO_2-captured CNAO-0.2 at 400 ^oC

4.12 Impact of Operating Conditions on CO_2 Capture by MNAO-0.2 and CNAO-0.2

This study investigated the influence of various operating conditions on the CO_2 capture performance of MNAO-0.2 and CNAO-0.2 LDOs. The findings highlighted the influences of simulated gas flow rate, adsorbent amount, and packed-bed length in the CO_2 capture process.

Effect of flow rate: The study evaluated the CO_2 capture capacities of MNAO-0.2 and CNAO-0.2 at different simulated flue gas flow rates (10, 20, and 40 mL/min). A clear trend emerged, indicating a decrease in CO_2 saturation capacity with increasing flow rate (Figure 45 A and B). This observation can be attributed to the reduced contact time between the CO_2 molecules and the adsorbent surface at higher flow rates. Consequently, the CO_2 molecules have less time to interact and be adsorbed by the LDOs, leading to a faster breakthrough point in the adsorption process (Chowdhury *et al*., 2013).

Effect of adsorbent amount: The impact of varying the amount of MNAO-0.2 and CNAO-0.2 (100, 200, and 300 mg) on CO_2 capture was also examined (Figure 45 C and D). The results revealed a significant increase in CO_2 saturation capacity with an increase in adsorbent amount. For example, MNAO-0.2 and CNAO-0.2 exhibited the highest capacities of 13.90 and 16.47 mmol/g, respectively, at the highest adsorbent loading (300 mg). This observed rise can be explained by the increased availability of active sites on the LDOs for CO_2 adsorption as the amount of adsorbent material increases.

Effect of packed-bed length: This study further explored the effect of packed-bed length on the CO_2 capture performance of the LDOs. Packed-bed lengths of 5 cm and 10 cm were employed (Figure 45 E and F). The results demonstrated a significant increase in CO_2 adsorption capacity with increasing packed-bed length. For instance, the capacities for MNAO-0.2 and CNAO-0.2 increased from 7.85 and 8.36 mmol/g at 5 cm to 10.69 and 14.09 mmol/g at 10 cm, respectively. This enhancement can be attributed to the reduced mass transfer resistance within the column. A longer packed bed allows for a more even distribution of the adsorbent material, enabling CO_2 molecules to interact with a larger surface area and promoting higher CO_2 capture efficiency (Chowdhury *et al*., 2013).

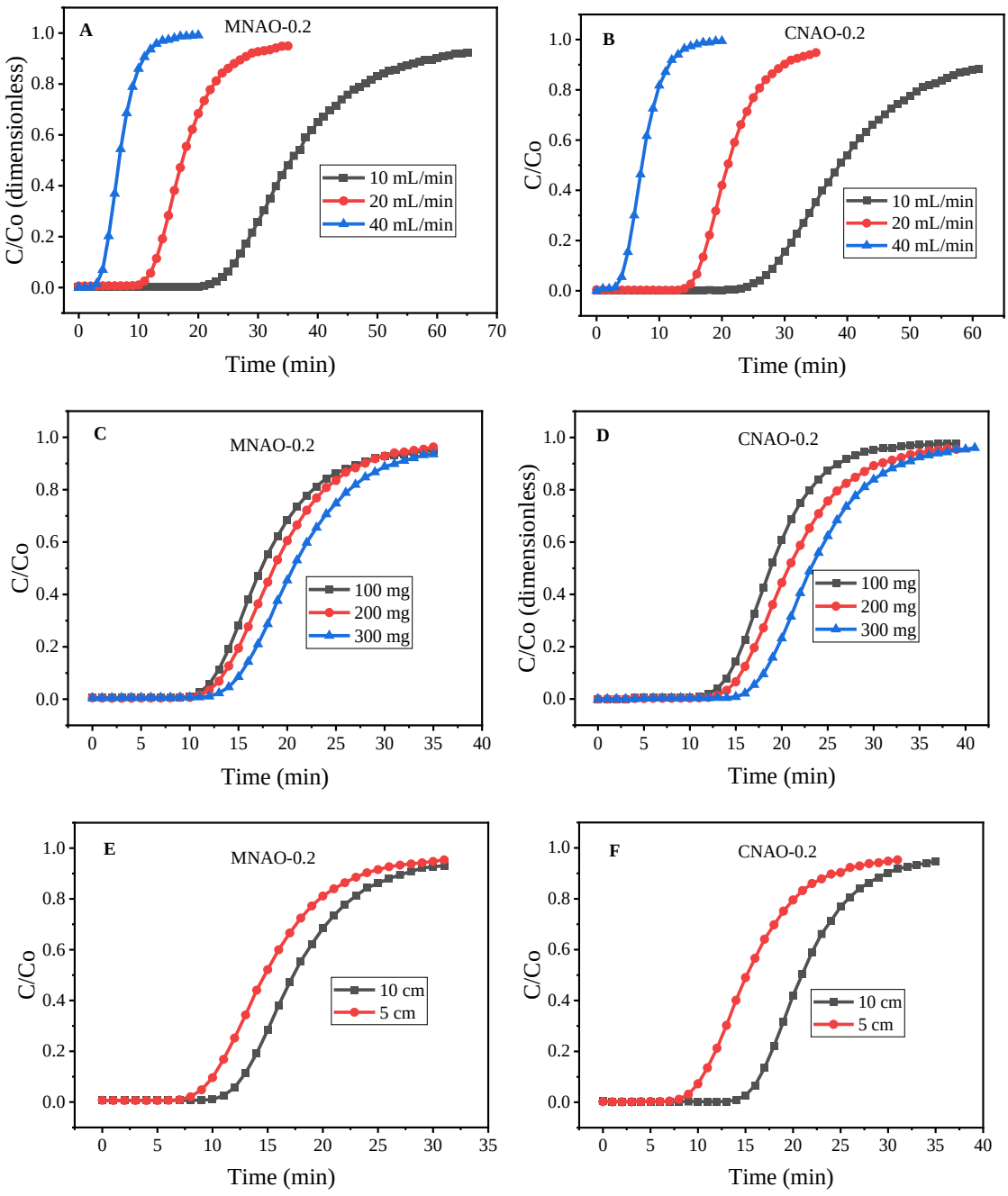

Figure 45. Effects of the flow rate (A, B), adsorbent amount (C, D) and packed-bed length (E, F) on CO_2 capture by MNAO-0.2 and CNAO-0.2

4.13 CO_2 Adsorption Mechanisms

CO_2 adsorption on the synthesized LDOs is a surface-mediated process that involves acid-base interactions. The acidic CO_2 molecules react with basic sites on the LDOs, such as O^{2-} (strong), and metal-O (medium), and the cations to form various surface complexes. The complexes can be classified into three main categories: bidentate carbonate, mono-dentate

carbonate, and bulk carbonate. These complexes can be identified by their characteristic peaks in the ATR FT-IR spectra (Figures 37 and 42) (Gao *et al.*, 2013; Smoláková *et al.*, 2017; Wang *et al.*, 2022).

The formation of these complexes depends on the composition, and structure of the mixed oxides. The doping of metal ions, such as Ce^{4+} or Mn^{2+}, can create more oxygen vacancies and basic sites on the surface of the LDOs, enhancing the CO_2 adsorption potential and stability. The CO_2 adsorption on LDOs is reversible and can be regenerated by heating or purging with an inert gas (Wang *et al*., 2022).

The mechanisms of CO_2 adsorption on LDOs can be explained by the following hypothetical reactions:

i) Monodentate carbonate: $CO_2 + M\text{-}O \rightarrow O\text{-}M\text{-}OCO$, where M is a metal site such as Ni, Ce, Mn, or Al. This reaction occurs at low temperatures and is reversible by heating or purging with an inert gas (Kumar and Saxena, 2014).

ii) Bidentate carbonate: $CO_2 + MO \rightarrow M\text{-}OOCO$. This is stable up to 240 °C. Additionally, $CO_2 + 2OH^- \rightarrow CO_3^{2-} + H_2O$, where OH^- is a surface hydroxyl group, possibly due to some residual water vapor being present in the column due to the ambient humidity (Kumar and Saxena, 2014; Qin *et al*., 2021; Yoshikawa *et al*., 2014).

iii) Bulk carbonate: $CO_2 + MO \rightarrow M\text{-}O\text{-}CO_2$. This is more stable than bidentate carbonate. This can also be expressed as $CO_2 + O^{2-} \rightarrow CO_3^{2-}$, where O^{2-} is lattice oxygen. It involves the diffusion of CO_2 into the bulk of the LDOs in which the carbonate is bonded to more than one metal. It can be decomposed at a temperature of more than 340 °C (Kumar and Saxena, 2014; Lwin and Abdullah, 2009; Yoshikawa *et al*., 2014).

4.14 Comparison with Previous Studies

In Table 29, we compared the CO_2 adsorption capacities of CNAO-0.2 (14.09 mmol/g) and MNAO-0.2 (10.69 mmol/g) with previous studies those reported over the last fifteen years. Our results showed that the CO_2 adsorption capacities of CNAO-0.2 and MNAO-0.2 are

promising compared to the literature. The CO_2 adsorption capacities reported in the reviewed papers ranged from 0.46 to 12.27 mmol/g.

Table 29. Comparison of CO_2 adsorption onto CNAO-0.2 and MNAO-0.2 with previous studies

Adsorbents	Experimental conditions			CO_2 adsorption capacity (mmol/g)	References
	Inlet CO_2 concentration, %	Temp, ^oC	System		
C-700	12.5	30	Purpose-built fixed-bed adsorption	0.676	(Goel et al., 2016)
Ni-Al-CO_3 DH	15	50	Micromeritics 3Flex	0.87	(Shang et al., 2019)
Mg_3Al-DOC12-MC		300	CO_2-TPD experiments	0.85	(Wang et al., 2022)
Modified silica capsules	10	75	Packed bed flow reactor	4.45 to 7.93	(Qi et al., 2011)
K_2CO_3-promoted Mg-Al LDH/MWNT composite	10	300	Fixed-bed reactor	1.12	(Bhatta et al., 2016)
Mg_3Fe_1	10	200	TGA	0.462	(Wang et al., 2010)
CNT(APTS)	15	50	Packed-bed column	2.45	(Su et al., 2011)
Mg−Al−CO_3 hydrotalcite	25	240	TGA	9.27	(Kim et al., 2016)
Zeolite 13X	20	25	Volumetric	6.9	(Garshasbi et al., 2017)
Cu-BTC	15	25	Isotherm (IGA)	12.7	(Liang et al., 2009)
CNAO-0.2	13	31	Packed-bed column	14.40	This study
MNAO-0.2	13	31	Packed-bed column	10.69	This study

Our findings indicated that the synthesized LDOs from their LDHs are promising nanomaterials for capturing CO_2 from flue gas. Even though the Ce^{4+}-doped Ni-Al LDO showed better performance than the Mn^{2+}-doped, both showed good performance when compared to previous reports. CO_2 saturation capacities were found to be 14.09 and 10.69 mmol/g for Ce^{4+}-doped and Mn^{2+}-doped Ni-Al LDOs, respectively. These findings were

supported by examining the experimental studies using fixed-bed models. Further, the influence of various operating conditions on the CO_2 capture process was explored. Simulated flue gas flow rate, adsorbent amount and packed-bed length were found to affect the CO_2 capturing process. The results showed that the CO_2 saturation capacity of the LDOs increased with increasing adsorbent amount and packed-bed length and decreased with increasing flow rate. Moreover, the effect of temperature on the regeneration process was also investigated, and results indicated that the performance of the exhausted adsorbent increased with increasing temperature.

CHAPTER 5

CONCLUSIONS AND RECOMMENDATIONS

In this study, Mn^{2+} and Ce^{4+} doped Ni-Al LDHs and LDOs were successfully synthesized using the co-precipitation method. Their potential applications for CO_2 capture from simulated flue gas and fluoride removal from aqueous solutions were investigated utilizing approaches that mimicked real-world applications: packed-bed column experiments for CO_2 capture and batch experiments for fluoride removal. Characterization techniques confirmed the formation of nanosheet structures with high surface areas, ideal for efficient adsorption. The XRD analysis showed that the intended LDHs with hydrotalcite-like crystal structures were obtained, which was further supported by the HRTEM analysis. The morphological analysis by SEM and HRTEM confirmed that both material types, LDHs and LDOs, have sheet-like shapes. XPS analysis showed the presence of the intended elements with their oxidation states in the synthesized MNAHs, MNAOs, CNAHs and CNAOs. The BET analysis showed that the LDOs have greater surface areas than their precursor LDHs, CNAO-0.2 having a greater surface area of 189 m^2/g.

The findings revealed significant promise for both LDHs and LDOs in these applications. They displayed good performance in removing fluoride ions from aqueous solutions. LDOs displayed remarkable performance in capturing CO_2 from simulated flue gas. The analysis revealed some key differences in the performance of the materials. CNAO-0.2 displayed the highest CO_2 capture capacity (14.09 mmol/g) due to its enhanced surface area and stronger CO_2 adsorption affinity. Whereas, LDHs demonstrated superior fluoride removal (238.27 mg/g) compared to LDOs, attributed to their inherent ability to participate in ion exchange, a mechanism which is absent in LDOs. Overall, the findings of this study support the use of Mn^{2+} and Ce^{4+}-doped Ni-Al LDHs and LDOs as efficient and promising materials for CO_2 capturing from flue gas and fluoride removal in water treatment applications.

Based on these findings, we recommend some avenues for future exploration. In the case of CO_2 capture, it is recommended to evaluate the materials' performance under diverse operating conditions, such as temperature, pressure, and gas composition, is crucial for real-world application. In the case of F^- adsorption, we highly recommend further experiments

utilizing water samples directly collected from fluoride-polluted lakes, rivers, and factory effluents to validate their performance in real-world scenarios. Furthermore, it is recommended to explore other dopants that might provide opportunities to further improve the materials' CO_2 capture and fluoride removal capabilities. Finally, it is recommended to use centrifugal separation for industrial-scale F^- adsorption to isolate nanomaterial from real water samples, while ultrafiltration might be necessary for very small particle sizes.

REFERENCES

Abasi, C. Y., *et al.* (2018). Synthesis, Characterisation of Ternary layered Double Hydroxides (LDH) for Sorption Kinetics and Thermodynamics of Cd^{2+}. *International Journal of Environmental Studies, 76*(3), 441-455. https://doi.org/10.-1080/00207233.2018.1517936

Ahmed, A. A. A., *et al.* (2012). Thermal, Optical and Dielectric Properties of Zn–Al Layered Double Hydroxide. *Applied Clay Science, 56,* 68-76.

Al Mesfer, M. K. and Danish, M. (2018). Breakthrough Adsorption Study of Activated Carbons for CO_2 Separation from Flue Gas. *Journal of Environmental Chemical Engineering, 6*(4), 4514-4524.

Albuquerque, D. W. S., *et al.* (2016). Evaluation of the Behavior of Hydrotalcite Like-Materials for CO_2 Capture. *Applied Mechanics and Materials, 830,* 3-10. https://doi.org/10.4028/www.scientific.net/AMM.830.3

Ali, B., *et al.* (2020). Competitive Adsorption of Binary Dye from Aqueous Solutions Using Calcined Layered Double Hydroxides. *International Journal of Environmental Analytical Chemistry, 102*(14), 3207-3226. https://doi.org/10.1080/03067319.2020.-1766035

Ali, H. and Khan, E. (2017). Environmental Chemistry in the Twenty-first Century. *Environmental Chemistry Letters, 15*(2), 329-346.

Almoisheer, N., *et al.* (2019). Adsorption and Anion Exchange Insight of Indigo Carmine onto CuAl-LDH/SWCNTs Nanocomposite: Kinetic, Thermodynamic and Isotherm Analysis. *RSC Advances, 9*(1), 560-568. https://doi.org/10.1039/c8ra09562k

Amiri, M., *et al.* (2017). Optimization of CO_2 Capture Process from Simulated Flue Gas by Dry Regenerable Alkali Metal Carbonate Based Adsorbent Using Response Surface Methodology. *Energy & Fuels, 31*(5), 5286-5296. https://doi.org/10.1021/acs.-energyfuels.6b03303

Anandan, S., *et al.* (2013). Sonochemical Synthesis of Manganese (II) Hydroxide for Supercapacitor Applications. *Materials Research Bulletin, 48*(9), 3357-3361.

Anderson, K., *et al.* (2023). Controversies of Carbon Dioxide Removal. *Nature Reviews Earth & Environment*. https://doi.org/10.1038/s43017-023-00493-y

Ang, Y. Q., *et al.* (2023). Carbon Reduction Technology Pathways for Existing Buildings in Eight Cities. *Nature Communications*, *14*(1), 1689. https://doi.org/10.1038/s41467-023-37131-6

Aponte, Á. G., *et al.* (2020). Cerium Oxide Nanoparticles for Color Removal of Indigo Carmine And Methylene Blue Solutions. *AIMS Materials Science*, *7*(4), 468-485.

Ashekuzzaman, S. M. and Jiang, J.-Q. (2014). Study on the Sorption–desorption–regeneration Performance of Ca-, Mg- and CaMg-based Layered Double Hydroxides for Removing Phosphate from Water. *Chemical Engineering Journal*, *246*, 97-105. https://doi.org/10.1016/j.cej.2014.02.061

Asouhidou, D. D., *et al.* (2012). Adsorption of Reactive Dyes from Aqueous Solutions by Layered Double Hydroxides. *Journal of Chemical Technology & Biotechnology*, *87*(4), 575-582.

Ayawei, N., *et al.* (2015). Synthesis, Characterization and Application of Mg/Al Layered Double Hydroxide for the Degradation of Congo Red in Aqueous Solution. *Open Journal of Physical Chemistry*, *05*(03), 56-70. https://doi.org/10.4236/ojpc.2015.-53007

Ayawei, N., *et al.* (2017). Modelling and Interpretation of Adsorption Isotherms. *Journal of Chemistry*, *2017*.

Aziz, M. A. A., *et al.* (2020). Understanding the Role of Surface Basic Sites of Catalysts in CO_2 Activation in Dry Reforming of Methane: A Short Review. In *Catalysis Science & Technology* (Vol. 10, pp. 35-45): The Royal Society of Chemistry.

Baig, N. and Sajid, M. (2017). Applications of Layered Double Hydroxides Based Electrochemical Sensors for Determination of Environmental Pollutants: A Review. *Trends in Environmental Analytical Chemistry*, *16*, 1-15. https://doi.org/https://-doi.org/10.1016/j.teac.2017.10.003

Baig, N., *et al.* (2019). Recent Trends in Nanomaterial-modified Electrodes for Electroanalytical Applications. *TrAC Trends in Analytical Chemistry*, *111*, 47-61. https://doi.org/10.1016/j.trac.2018.11.044

Balseiro-Romero, M. and Baveye, P. C. (2018). Book Review: Soil Pollution: A Hidden Danger Beneath Our Feet. In: Frontiers Media SA.

Banerjee, S. and Gautam, P. K. (2016). Layered Double Hydroxides Nanomaterials for Water Remediation. In *Nanomaterials for Wastewater Remediation* (pp. 161-188). https://doi.org/10.1016/b978-0-12-804609-8.00008-x

Basu, D., *et al.* (2014). Advances in Layered Double Hydroxide (LDH)-based Elastomer Composites. *Progress in Polymer Science, 39*(3), 594-626. https://doi.org/10.1016/-j.progpolymsci.2013.07.011

Benhiti, R., *et al.* (2020). Synthesis, Characterization, and Comparative Study of MgAl-LDHs Prepared by Standard Coprecipitation and Urea Hydrolysis Methods for Phosphate Removal. *Environmental Science and Pollution Research, 27*(36), 45767-45774. https://doi.org/10.1007/s11356-020-10444-5

Bering, B., *et al.* (1972). On Thermodynamics of Adsorption in Micropores. *Journal of Colloid and Interface Science*, *38*(1), 185-194.

Bhatta, L. K. G., *et al.* (2016). Layered Double Hydroxides/Multiwalled Carbon Nanotubes-based Composite for High-temperature CO_2 Adsorption. *Energy & Fuels*, *30*(5), 4244-4250.

Bhattacharyya, K. (2015). Ni/Ti Layered Double Hydroxide: Synthesis, Characterization and Application as a Photocatalyst for Visible Light Degradation of Aqueous Methylene Blue. *Dalton Transactions (Cambridge, England: 2003)*, *44*(15), 6809-6824.

Bo, L., *et al.* (2016). Adsorptive Removal of Fluoride Using Hierarchical Flower-like Calcined Mg–Al Layered Double Hydroxides. *Environmental Progress & Sustainable Energy*, *35*(5), 1420-1429.

Bustillos, S., *et al.* (2020). Implementation of Ion Exchange Processes for Carbon Dioxide Mineralization Using Industrial Waste Streams. *Frontiers in Energy Research, 8*, 610392.

Cabrera-Munguia, D. A., *et al.* (2020). Tuning the Basic Properties of ZnAl Hydrotalcites Modified with Ce Applied to Transesterification of Soybean Oil. *Catalysis Letters, 150*(7), 1957-1969. https://doi.org/10.1007/s10562-020-03099-x

Cai, J., *et al.* (2018a). Enhanced Defluoridation Using Novel Millisphere Nanocomposite of La-Doped Li-Al Layered Double Hydroxides Supported by Polymeric Anion

Exchanger. *Scientific Reports, 8*(1), 11741. https://doi.org/10.1038/s41598-018-29497-1

Cai, J., *et al.* (2018b). Enhanced Fluoride Removal by La-doped Li/Al Layered Double Hydroxides. *Journal of Colloid and Interface Science 509*, 353-359. https://doi.org/-10.1016/j.jcis.2017.09.038

Cavani, F., *et al.* (1991). Hydrotalcite-type Anionic Clays: Preparation, Properties and Applications. *Catalysis Today*, *11*(2), 173-301.

Chaillot, D., *et al.* (2021). Layered Double Hydroxides and LDH-derived Materials in Chosen Environmental Applications: A Review. *Environmental Science and Pollution Research*, *28*(19), 24375-24405.

Chatterjee, S. K. (2010). *X-ray Diffraction: Its Theory and Applications*. PHI Learning Pvt. Ltd.

Chen, Y., *et al.* (2020). Mitigation of Arctic Permafrost Carbon Loss Through Stratospheric Aerosol Geoengineering. *Nature Communications*, *11*(1), 2430. https://doi.org/-10.1038/s41467-020-16357-8

Chowdhury, Z. Z., *et al.* (2013). Breakthrough Curve Analysis for Column Dynamics Sorption of Mn(II) Ions from Wastewater by Using Mangostana Garcinia Peel-Based Granular-activated Carbon. *Journal of Chemistry*, *2013*, 1-8. https://doi.org/10.-1155/2013/959761

Chubar, N., *et al.* (2017). Layered Double Hydroxides as the Next Generation Inorganic Anion Exchangers: Synthetic Methods Versus Applicability. *Advances in Colloid and Interface Science*, *245*, 62-80.

Clark, I., *et al.* (2019). Continuous Synthesis of $Zn_2Al–CO_3$ Layered Double Hydroxides: A Comparison of Bench, Pilot and Industrial Scale Syntheses. *Reaction Chemistry & Engineering*, *4*(4), 663-666. https://doi.org/10.1039/c8re00241j

Clause, O., *et al.* (1991). Preparation and Thermal Reactivity of Nickel/Chromium and Nickel/Aluminium Hydrotalcite-type Precursors. *Applied Catalysis*, *73*(2), 217-236.

Clause, O., *et al.* (1992). Preparation and Characterization of Nickel-Aluminum Mixed Oxides Obtained by Thermal Decomposition of Hydrotalcite-type Precursors. *Journal of Catalysis*, *133*(1), 231-246.

Colonna, S., *et al.* (2018). CO_2 Adsorption and Desorption Properties of Calcined Layered Double Hydroxides. *Journal of Thermal Analysis and Calorimetry, 133*(2), 869-879. https://doi.org/10.1007/s10973-018-7152-8

Crini, G., *et al.* (2018). Conventional and non-conventional adsorbents for wastewater treatment. *Environmental Chemistry Letters, 17*(1), 195-213. https://doi.org/10.-1007/s10311-018-0786-8

Dada, A. O., *et al.* (2021). Two–three Parameters Isotherm Modeling, Kinetics with Statistical Validity, Desorption and Thermodynamic Studies of Adsorption of Cu(II) Ions onto Zerovalent Iron Nanoparticles. *Scientific Reports*, *11*(1), 1-15.

Daniel, S. and Thomas, S. (2020). Layered Double Hydroxides: Fundamentals to Applications. In *Layered Double Hydroxide Polymer Nanocomposites* (pp. 1-76). Elsevier.

Das, S., *et al.* (2018). Kinetics, Isotherm, and Thermodynamic Study for Ultrafast Adsorption of Azo Dye by an Efficient Sorbent: Ternary Mg/(Al + Fe) Layered Double Hydroxides. *ACS Omega*, *3*(3), 2532-2545.

Daud, M., *et al.* (2019). A Review on the Recent Advances, Challenges and Future Aspect of Layered Double Hydroxides (LDH)– Containing Hybrids as Promising Adsorbents for Dyes Removal. *Journal of Molecular Liquids*, *288*. https://doi.org/-10.1016/j.molliq.2019.110989

Demelash, H., *et al.* (2019). Fluoride Concentration in Ground Water and Prevalence of Dental Fluorosis in Ethiopian Rift Valley: Systematic Review and Meta-analysis. *BMC Public Health*, *19*(1), 1-9.

Dessalegne, M., *et al.* (2016). Layered Double Hydroxide and Its Calcined Product for Fluoride Removal from Groundwater of Ethiopian Rift Valley. *Water, Air, & Soil Pollution*, *227*(10), 381. https://doi.org/10.1007/s11270-016-3079-5

do Nascimento, L. A., *et al.* (2022). NiAlCe Mixed Oxides Obtained from Layered Double Hydroxides Applied to Anisole Hydrodeoxygenation. *Catalysis Today, 394*, 282-294.

dos Santos, R. M. M., *et al.* (2013). Removal of Acid Green 68: 1 from Aqueous Solutions by Calcined and Uncalcined Layered Double Hydroxides. *Applied Clay Science*, *80*, 189-195.

El-Bery, H. M., *et al.* (2022). High Adsorption Capacity of Phenol and Methylene Blue Using Activated Carbon Derived from Lignocellulosic Agriculture Wastes. *Scientific Reports, 12*(1), 1-17.

El Rouby, W. M., *et al.* (2020). Efficient Water Decontamination Using Layered Double Hydroxide Beads Nanocomposites. *Environmental Science and Pollution Research, 27*, 18985-19003.

Elhalil, A., *et al.* (2016). Defluoridation of Groundwater by Calcined Mg/Al Layered Double Hydroxide. *Emerging Contaminants, 2*(1), 42-48. https://doi.org/10.1016/j.emcon.-2016.03.002

Eniola, J. O., *et al.* (2020). Synthesis and Characterization of $CuFe_2O_4$/NiMgAl-LDH Composite for the Efficient Removal of Oxytetracycline Antibiotic. *Journal of Saudi Chemical Society*, *24*(1), 139-150. https://doi.org/10.1016/j.jscs.2019.11.001

Evans, D. G. and Slade, R. C. (2006). Structural Aspects of Layered Double Hydroxides. *Layered double hydroxides*, 1-87.

Falkowski, V., *et al.* (2018). Synthesis and Characterization of the New Manganese Hydroxide Chloride, γ-Mn(OH)Cl. *European Journal of Inorganic Chemistry*, *2018*(42), 4630-4637.

Farooq, M., *et al.* (2020). CO_2 Capture Through Electro-Conductive Adsorbent Using Physical Adsorption System for Sustainable Development. *Environmental Geochemistry and Health, 42*, 1507-1515.

Forano, C., *et al.* (2013). Layered Double Hydroxides (LDH). In *Developments in Clay Science* (Vol. 5, pp. 745-782). Elsevier.

Gabrielli, P., *et al.* (2020). The Role of Carbon Capture and Utilization, Carbon Capture and Storage, and Biomass to Enable a Net-Zero-CO_2 Emissions Chemical Industry. *Industrial & Engineering Chemistry Research*, *59*(15), 7033-7045. https://doi.org/-10.1021/acs.iecr.9b06579

Gabrovska, M., *et al.* (2016). Ni–Al Layered Double Hydroxides as Precursors of Ceramic Pigments. Proceedings of the III Advanced Ceramics and Applications Conference,

Gao, Y., *et al.* (2022). Manganese Modified Activated Alumina through Impregnation for Enhanced Adsorption Capacity of Fluoride Ions. *Water, 14*(17), 2673.

Gao, Y., *et al.* (2013). Comprehensive investigation of CO 2 adsorption on Mg–Al–CO_3 LDH-derived Mixed Metal Oxides. *Journal of Materials Chemistry A*, *1*(41), 12782-12790.

Gao, Z., *et al.* (2021). Synthesis of Ce-doped NiAl LDH/RGO Composite as an Efficient Photocatalyst for Photocatalytic Degradation of Ciprofloxacin. *Journal of Environmental Chemical Engineering*, *9*(4), 105405.

Garcés-Polo, S. I., *et al.* (2018). Adsorption of CO_2 on Mixed Oxides Derived from Hydrotalcites at Several Temperatures and High Pressures. *Chemical Engineering Journal, 332*, 24-32. https://doi.org/10.1016/j.cej.2017.09.056

Garshasbi, V., *et al.* (2017). Equilibrium CO_2 Adsorption on Zeolite 13X Prepared from Natural Clays. *Applied Surface Science*, *393*, 225-233. https://doi.org/https://-doi.org/10.1016/j.apsusc.2016.09.161

George, G. and Saravanakumar, M. P. (2018). Facile Synthesis of Carbon-coated Layered Double Hydroxide and Its Comparative Characterisation with Zn–Al LDH: Application on Crystal Violet and Malachite Green Dye Adsorption—Isotherm, Kinetics and Box-Behnken Design. *Environmental Science and Pollution Research, 25*(30), 30236-30254.

Gevers, B. R., *et al.* (2019). Comparison of Nano-structured Transition Metal Modified Tri-metal MgMAl–LDHs (M = Fe, Zn, Cu, Ni, Co) Prepared Using Co-precipitation. *RSC Advances, 9*(48), 28262-28275. https://doi.org/10.1039/c9ra05452a

Ghosh, A. K., *et al.* (2012). Effect of Long-term Application of Treated Sewage Water on Heavy Metal Accumulation in Vegetables Grown in Northern India. *Environmental Monitoring and Assessment, 184*(2), 1025-1036.

Goel, C., *et al.* (2016). Novel Nitrogen Enriched Porous Carbon Adsorbents for CO_2 Capture: Breakthrough Adsorption Study. *Journal of Environmental Chemical Engineering, 4*(1), 346-356.

Goh, K.-H., *et al.* (2008). Application of Layered Double Hydroxides for Removal of Oxyanions: A Review. *Water Research, 42*(6-7), 1343-1368.

Gök, A. (2020). Enhanced Adsorption of Nicotinic Acid by Different Types of Mg/Al Layered Double Hydroxides: Synthesis, Equilibrium, Kinetics, and Thermodynamics. *Journal of Dispersion Science and Technology*, *41*(5), 779-786.

Grosu, E. F. (2018). Layered Double Hydroxides Nanomaterials in Biomedicine and (Bio) Sensing Design. *Biomedical Journal of Scientific & Technical Research*, *2*(4). https://doi.org/10.26717/bjstr.2018.02.000786

Guo, X., *et al.* (2018). Superb Adsorption of Organic Dyes from Aqueous Solution on Hierarchically Porous Composites Constructed by ZnAl-LDH/$Al(OH)_3$ Nanosheets. *Microporous and Mesoporous Materials*, *259*, 123-133. https://doi.org/10.1016/j.micromeso.2017.10.003

Hack, J., *et al.* (2022). Review on CO_2 Capture Using Amine-functionalized Materials. *ACS Omega*, *7*(44), 39520-39530.

Hadi, S., *et al.* (2021). Adsorption of 4-Chlorophenol by Magnetized Activated Carbon from Pomegranate Husk Using Dual Stage Chemical Activation. *Chemosphere*, *270*, 128623.

Hammerli, J., *et al.* (2021). Measuring in situ CO_2 and H_2O in Apatite via ATR-FTIR. *Contributions to Mineralogy and Petrology*, *176*, 1-20.

Hanif, A., *et al.* (2019). Exfoliated Ni-Al LDH 2D Nanosheets for Intermediate Temperature CO_2 Capture. *Journal of Hazardous Materials*, *374*, 365-371.

Haseena, M., *et al.* (2017). Water Pollution and Human Health. *Environ Risk Assess Remediat*, *1*(3), 16-19.

He, S., *et al.* (2017). Layered Double Hydroxides: Structure–Property Relationships. *Handbook of Solid State Chemistry*, 541-569.

He, Y., *et al.* (2019). Enhanced Fluoride Removal from Water by Rare Earth (La and Ce) Modified Alumina: Adsorption Isotherms, Kinetics, Thermodynamics and Mechanism. *Science of The Total Environment*, *688*, 184-198. https://doi.org/https://doi.org/10.1016/j.scitotenv.2019.06.175

Hibino, T. (2018). Anion Selectivity of Layered Double Hydroxides: Effects of Crystallinity and Charge Density. *European Journal of Inorganic Chemistry*, *2018*(6), 722-730.

Ho, Y. S. and McKay, G. (1998). A Comparison of Chemisorption Kinetic Models Applied to Pollutant Removal on Various Sorbents. *Process Safety and Environmental Protection*, *76*(4), 332-340.

Hu, Q., *et al.* (2021). Deeper Insights into the Bohart–Adams Model in a Fixed-Bed Column. *The Journal of Physical Chemistry B*, *125*(30), 8494-8501. https://doi.org/10.1021/-acs.jpcb.1c03378

Ichou, A. A., *et al.* (2020). Adsorption of Pb(II) from Aqueous Solutions onto MgFeAl-CO_3 LDH: Thermodynamic And Kinetic Studies. *Desalination and Water Treatment*, *178*, 193-202. https://doi.org/10.5004/dwt.2020.24952

Jabeen, M., *et al.* (2017). Synthesis of Ni/Co/Al-Layered Triple Hydroxide@ Brominated Graphene Hybrid on Nickel Foam as Electrode Material for High-performance Supercapacitors. *RSC Advances*, *7*(74), 46553-46565.

Jamil, S., *et al.* (2019). Layered Double Hydroxides (LDHs) Synthesis and Applications. *Progress in Chemistry*, *31(2 /3)*(2/3), 394-412. https://doi.org/10.7536/PC180505

Jawad, A., *et al.* (2019). Selective Removal of Heavy Metals by Hydrotalcites as Adsorbents in Diverse Wastewater: Different Intercalated Anions with Different Mechanisms. *Journal of Cleaner Production*, *211*, 1112-1126. https://doi.org/10.1016/j.jclepro.-2018.11.234

Jiang, Z., *et al.* (2020). Low-temperature Synthesis of Carbonate-intercalated Ni_xFe-Layered Double Hydroxides for Enhanced Adsorption Properties. *Applied Surface Science*, *531*, 147281.

Jitianu, M., *et al.* (2013). Nanosized Ni–Al Layered Double Hydroxides—Structural Characterization. *Materials Research Bulletin*, *48*(5), 1864-1873.

Karami, Z., *et al.* (2019). Curing Epoxy with Mg-Al LDH Nanoplatelets Intercalated with Carbonate Ion. *Progress in Organic Coatings*, *136*, 105278.

Kedesdy, H. and Drukalsky, A. (1954). X-Ray Diffraction Studies of the Solid State Reaction in the NiO-ZnO System. *Journal of the American Chemical Society*, *76*(23), 5941-5946.

Keller, J. U. and Staudt, R. (2005). *Gas Adsorption Equilibria: Experimental Methods and Adsorptive Isotherms*. Springer Science & Business Media.

Kim, M.-J., *et al.* (2020). Effect of Surface Properties Controlled by Ce Addition on CO_2 Methanation Over Ni/Ce/Al_2O_3 Catalyst. *International Journal of Hydrogen Energy*, *45*(46), 24595-24603.

Kim, S., *et al.* (2016). High-temperature CO_2 Sorption on Hydrotalcite Having a High Mg/Al Molar Ratio. *ACS Applied Materials and Interfaces*, *8*(9), 5763-5767.

Klemkaite, K., *et al.* (2011). Synthesis and Characterization of Layered Double Hydroxides with Different Cations (Mg, Co, Ni, Al), Decomposition and Reformation of Mixed Metal Oxides to Layered Structures. *Open Chemistry*, *9*(2), 275-282. https://doi.org/-10.2478/s11532-011-0007-9

Kong, L., *et al.* (2019). Synchronous Phosphate and Fluoride Removal from Water by 3D Rice-like Lanthanum-doped La@MgAl Nanocomposites. *Chemical Engineering Journal, 371*, 893-902. https://doi.org/https://doi.org/10.1016/j.cej.2019.04.116

Kumar, A., *et al.* (2022). An Overview of Wind Energy Development and Policy Initiatives in India. *Clean Technologies and Environmental Policy*, *24*(5), 1337-1358. https://doi.org/10.1007/s10098-021-02248-z

Kumar, S. and Saxena, S. K. (2014). A Comparative Study of CO_2 Sorption Properties for Different Oxides. *Materials for Renewable and Sustainable Energy*, *3*, 1-15.

Kurlov, A., *et al.* (2020). Na_2CO_3-modified CaO-based CO_2 Sorbents: The Effects of Structure and Morphology on CO_2 Uptake. *Physical Chemistry Chemical Physics*, *22*(42), 24697-24703.

Lai, J. Y., *et al.* (2021). A Review of CO_2 Adsorbents Performance for Different Carbon Capture Technology Processes Conditions. *Greenhouse Gases: Science and Technology, 11*(5), 1076-1117. https://doi.org/10.1002/ghg.2112

Laipan, M., *et al.* (2020). Functionalized Layered Double Hydroxides for Innovative Applications. *Materials Horizons*, *7*(3), 715-745. https://doi.org/10.1039/c9mh-01494b

Landrigan, P. J. and Fuller, R. (2012). Environmental Pollution: An Enormous and Invisible Burden on Health Systems in Low-and Middle-income Counties. *World Hosp Health Serv*, *50*(4), 35.

Langmuir, I. (1918). The Adsorption of Gases on Plane Surfaces of Glass, Mica and Platinum. *Journal of the American Chemical Society*, *40*(9), 1361-1403.

Lawrence, M. G., *et al.* (2018). Evaluating Climate Geoengineering Proposals in the Context of the Paris Agreement Temperature Goals. *Nature Communications*, *9*(1), 3734. https://doi.org/10.1038/s41467-018-05938-3

Lee, H., *et al.* (2023). Climate Change 2023: Synthesis Report. Contribution of Working Groups I, II and III to the Sixth Assessment Report of the Intergovernmental Panel on Climate Change.

Lei, C., *et al.* (2017). Superb Adsorption Capacity of Hierarchical Calcined Ni/Mg/Al Layered Double Hydroxides for Congo Red and Cr(VI) Ions. *Journal of Hazardous Materials*, *321*, 801-811.

Li, L., *et al.* (2018). Controllable Preparation of 2D Nickel Aluminum Layered Double Hydroxide Nanoplates for High-performance Supercapacitors. *Journal of Materials Science: Materials in Electronics*, *29*, 17493-17502.

Li, L., *et al.* (2017). Ultrathin Petal-like NiAl Layered Double Oxide/Sulfide Composites as an Advanced Electrode for High-performance Asymmetric Supercapacitors. *Journal of Materials Chemistry A*, *5*(37), 19687-19696. https://doi.org/10.1039/c7ta06119f

Li, S., *et al.* (2019). Enhanced Arsenate Removal from Aqueous Solution by Mn-doped MgAl-Layered Double Hydroxides. *Environ Sci Pollut Res Int*, *26*(12), 12014-12024. https://doi.org/10.1007/s11356-019-04667-4

Liang, Z., *et al.* (2009). CO_2 Adsorption-Based Separation by Metal Organic Framework (Cu-BTC) versus Zeolite (13X). *Energy & Fuels*, *23*(5), 2785-2789. https://doi.org/-10.1021/ef800938e

Liao, Y. (2006). Practical Electron Microscopy and Database. *An Online Book*.

Lin, C.-H., *et al.* (2017). Synthesis and Optical Properties of Mg-Al Layered Double Hydroxides Precursor Powders. *AIP ADVANCES*, *7*(12), 125005.

Lin, J., *et al.* (2018). Preparation of a Novel CeO_2/SiO_2 Adsorbent and Its Adsorption Behavior for Fluoride Ion. *Adsorption Science & Technology*, *36*(1-2), 743-761.

Liu, J., *et al.* (2019). Removal of Fluoride and Hardness by Layered Double Hydroxides: Property and Mechanism. *International Journal of Environmental Science and Technology*, *17*(2), 673-682. https://doi.org/10.1007/s13762-019-02457-6

Liu, Y., *et al.* (2014). Synthesis, Characterization and Application of Amino-functionalized Multi-walled Carbon Nanotubes for Effective Fast Removal of Methyl Orange from Aqueous Solution. *RSC Advances*, *4*(98), 55162-55172.

López-Luna, J., *et al.* (2019). Linear and Nonlinear Kinetic and Isotherm Adsorption Models for Arsenic Removal by Manganese Ferrite Nanoparticles. *SN Applied Sciences*, *1*(8), 1-19.

Lu, H., *et al.* (2018). Enhanced Adsorption Performance of Aspartic Acid Intercalated Mg-Zn-Fe-LDH Materials for Arsenite. *Dalton Transactions*, *47*(14), 4994-5004. https://doi.org/10.1039/C8DT00199E

Luo, S., *et al.* (2019). Synthesis of Calcined La-doped Layered Double Hydroxides and Application on Simultaneously Removal of Arsenate and Fluoride. *Journal of Solid State Chemistry*, *275*, 197-205. https://doi.org/10.1016/j.jssc.2019.04.017

Lv, Z., *et al.* (2018). Highly Efficient Removal of As (V) by Using NiAl Layered Double Oxide Composites. *Applied Surface Science*, *448*, 599-608.

Lwin, Y. and Abdullah, F. (2009). High Temperature Adsorption of Carbon Dioxide on Cu–Al Hydrotalcite-derived Mixed Oxides: Kinetics and Equilibria by Thermogravimetry. *Journal of Thermal Analysis and Calorimetry*, *97*, 885-889.

Machingauta, C. (2013). *Synthesis, Characterization and Application of Two-dimensional Layered Metal Hydroxides for Environmental Remediation Purposes*. Marquette University.

Mahjoubi, F. Z., *et al.* (2017). Zn–Al Layered Double Hydroxides Intercalated with Carbonate, Nitrate, Chloride and Sulphate Ions: Synthesis, Characterisation and Dye Removal Properties. *Journal of Taibah University for Science*, *11*(1), 90-100.

Mallakpour, S. and Behranvand, V. (2020). Layered Double Hydroxide Polymer Nanocomposites for Water Purification. In *Layered Double Hydroxide Polymer Nanocomposites* (pp. 781-803). https://doi.org/10.1016/b978-0-08-101903-0.00019-2

Mesfer, M. K. A., *et al.* (2020). Continuous Fixed Bed CO_2 Adsorption: Breakthrough, Column Efficiency, Mass Transfer Zone. *Processes*, *8*(10). https://doi.org/10.3390/-pr8101233

Milanovic, N. (2016). *Synthesis, Structural and Magnetic Properties of Layered Double Hydroxides*

Mir, Z. M., *et al.* (2020). Recent Advances on the Application of Layered Double Hydroxides in Concrete—A Review. *Materials*, *13*(6), 1426.

Mishra, G., *et al.* (2018). Layered Double Hydroxides: A Brief Review from Fundamentals to Application as Evolving Biomaterials. *Applied Clay Science*, *153*, 172-186. https://doi.org/10.1016/j.clay.2017.12.021

Mondal, N. K. and Roy, S. (2016). Optimization Study of Adsorption Parameters for Removal of Phenol on Gastropod Shell Dust Using Response Surface Methodology. *Clean Technologies and Environmental Policy*, *18*, 429-447.

Monzó, F., *et al.* (2019). Synthesis and Characterization of New Layered Double Hydroxide-Polyolefin Film Nanocomposites with Special Optical Properties. *Materials*, *12*(21), 3580.

Mudunkotuwa, I. A., *et al.* (2014). ATR-FTIR Spectroscopy as a Tool to Probe Surface Adsorption on Nanoparticles at the Liquid–Solid Interface in Environmentally and Biologically Relevant Media. *Analyst*, *139*(5), 870-881.

Mullick, A. and Neogi, S. (2019). Ultrasound Assisted Synthesis of Mg-Mn-Zr Impregnated Activated Carbon for Effective Fluoride Adsorption from Water. *Ultrason Sonochem*, *50*, 126-137. https://doi.org/10.1016/j.ultsonch.2018.09.010

Naseem, S., *et al.* (2019). Comparison of Transition Metal (Fe, Co, Ni, Cu, and Zn) Containing Tri-metal Layered Double Hydroxides (LDHs) Prepared by Urea Hydrolysis. *RSC Advances*, *9*(6), 3030-3040. https://doi.org/10.1039/c8ra10165e

Nazir, M. A., *et al.* (2020). Surface induced growth of ZIF-67 at Co-layered double hydroxide: Removal of methylene blue and methyl orange from water. *Applied Clay Science*, *190*, 105564. https://doi.org/https://doi.org/10.1016/j.clay.2020.105564

Ng, K. C., *et al.* (2017). A Universal Isotherm Model to Capture Adsorption Uptake and Energy Distribution of Porous Heterogeneous Surface. *Scientific Reports*, *7*(1), 1-11.

Ng, K. T. and Hercules, D. M. (1976). Studies of Nickel-Tungsten-Alumina Catalysts by X-Ray Photoelectron Spectroscopy. *The Journal of Physical Chemistry*, *80*(19), 2094-2102.

Nimibofa, A., *et al.* (2017). Comparative Sorption Studies of Dyes and Metal Ions by Ni/Al-Layered Double Hydroxide. *Int J Mater Chem*, *7*(3), 25-35.

Ochedi, F. O., *et al.* (2021). Carbon Dioxide Capture Using Liquid Absorption Methods: A Review. *Environmental Chemistry Letters*, *19*, 77-109.

Oladoja, N., *et al.* (2015). Characterization of Granular Matrix Supported Nano Magnesium Oxide as an Adsorbent for Defluoridation of Groundwater. *Chemical Engineering Journal, 281*, 632-643.

Osman, A. I., *et al.* (2020). Recent Advances in Carbon Capture Storage and Utilisation Technologies: A Review. *Environmental Chemistry Letters, 19*(2), 797-849. https://doi.org/10.1007/s10311-020-01133-3

Otgonjargal, E., *et al.* (2017). Removal of Chromium from Aqueous Solution by Thermally Treated Mgal Layered Double Hydroxide. *Annals of Civil and Environmental Engineering, 1*(1), 001-008. https://doi.org/10.29328/journal.acee.1001001

Ouyang, Y., *et al.* (2021). Preparation of ZnNiAl-LDHs Microspheres and Their Adsorption Behavior and Mechanism on U (VI). *Scientific Reports, 11*(1), 1-15.

Özdemir, Ç. S. and Onay, M. (2018). Determination of Parameters in Fixed Bed with Industrial Waste Used as Adsorbent. *Journal of Physical Chemistry and Functional Materials, 1*(1), 27-35.

Palupi, F. H. and Abeng, A. T. (2023). The Invisible Threat: Investigating the Effects of Air Pollution on Human Health and the Environment. *West Science Interdisciplinary Studies, 1*(06), 280-290.

Pan, Z., *et al.* (2020). Layered Double Hydroxide Derived NiAl-Oxide Hollow Nanospheres for Selective Transfer Hydrogenation with Improved Stability. *Journal of Materials Chemistry A, 8*(44), 23376-23384.

Patel, H. (2019). Fixed-Bed Column Adsorption Study: A Comprehensive Review. *Applied Water Science, 9*(3). https://doi.org/10.1007/s13201-019-0927-7

Pavel, O. D., *et al.* (2020). Layered Double Hydroxide. In *New Frontiers in Nanochemistry: Concepts, Theories, and Trends* (pp. 265-274). Apple Academic Press.

Podgorski, J. and Berg, M. (2022). Global Analysis and Prediction of Fluoride in Groundwater. *Nature Communications, 13*(1), 4232.

Prasad, C., *et al.* (2018). Magnetic Fe_3O_4 Based Layered Double Hydroxides (LDHs) nanocomposites (Fe_3O_4/LDHs): Recent Review of Progress in Synthesis, Properties and Applications. *Journal of Nanostructure in Chemistry, 8*(4), 393-412. https://doi.org/10.1007/s40097-018-0289-y

Prevot, V., *et al.* (2020). Confined Growth of NiAl-Layered Double Hydroxide Nanoparticles within Alginate Gel: Influence on Electrochemical Properties. *Front Chem*, *8*, 561975. https://doi.org/10.3389/fchem.2020.561975

Qi, G., *et al.* (2011). High Efficiency Nanocomposite Sorbents for CO_2 Capture Based on Amine-functionalized Mesoporous Capsules. *Energy & Environmental Science*, *4*(2), 444-452.

Qin, D., *et al.* (2021). In-Situ FTIR Study of CO_2 Adsorption and Methanation Mechanism Over Bimetallic Catalyst at Low Temperature. *Catalysis Letters*, 1-12.

Rafati, L., *et al.* (2019). Fixed Bed Adsorption Column Studies and Models for Removal of Ibuprofen from Aqueous Solution by Strong Adsorbent Nano-clay Composite. *J Environ Health Sci Eng*, *17*(2), 753-765. https://doi.org/10.1007/s40201-019-00392-9

Raganati, F., *et al.* (2019). Kinetic Study and Breakthrough Analysis of the Hybrid Physical/Chemical CO_2 Adsorption/Desorption Behavior of a Magnetite-based Sorbent. *Chemical Engineering Journal*, *372*, 526-535. https://doi.org/10.1016/j.cej-.2019.04.165

Raganati, F., *et al.* (2021). Adsorption of Carbon Dioxide for Post-combustion Capture: A Review. *Energy & Fuels*, *35*(16), 12845-12868. https://doi.org/10.1021/acs.-energyfuels.1c01618

Rahmanian, O., *et al.* (2018). Synthesis and Characterization of Citrate Intercalated Layered Double Hydroxide as a Green Adsorbent for Ni^{2+} and Pb^{2+} removal. *Environmental Science and Pollution Research*, *25*(36), 36267-36277.

Rathee, G., *et al.* (2019). A New Biocompatible Ternary Layered Double Hydroxide Adsorbent for Ultrafast Removal of Anionic Organic Dyes. *Scientific Reports*, *9*(1), 1-14.

Rathee, G., *et al.* (2020a). Calcined Layered Double Hydroxides: Catalysts for Xanthene, 1,4-Dihydropyridine, and Polyhydroquinoline Derivative Synthesis. *ACS Omega*, *5*(25), 15673-15680. https://doi.org/10.1021/acsomega.0c01901

Rathee, G., *et al.* (2020b). Simultaneous Elimination of Dyes and Antibiotic with a Hydrothermally Generated NiAlTi Layered Double Hydroxide Adsorbent. *ACS Omega*, *5*(5), 2368-2377.

Razzaq, I., *et al.* (2023). Reduction in Energy Consumption and CO_2 Emissions by Retrofitting an Existing Building to a Net Zero Energy Building for the Implementation of SDGs 7 and 13. *Frontiers in Environmental Science, 10*, 1028793.

Reddy, M. S. B., *et al.* (2021). Carbon Dioxide Adsorption Based on Porous Materials. *RSC Advances*, *11*(21), 12658-12681.

Ren, C., *et al.* (2021). Enhanced Fluoride Uptake by Layered Double Hydroxides Under Alkaline Conditions: Solid-state NMR Evidence of the Role of Surface> MgOH Sites. *Environmental Science & Technology*, *55*(22), 15082-15089.

Richards, L. A., *et al.* (2010). Impact of pH on the Removal of Fluoride, Nitrate and Boron by Nanofiltration/Reverse Osmosis. *Desalination*, *261*(3), 331-337.

Sabouni, R., *et al.* (2013). Mathematical Modeling and Experimental Breakthrough Curves of Carbon Dioxide Adsorption on Metal Organic Framework CPM-5. *Environmental Science & Technology*, *47*(16), 9372-9380.

Santamaría, L., *et al.* (2023). Layered Double Hydroxides for CO_2 Adsorption at Moderate Temperatures: Synthesis and Amelioration Strategies. *Chemical Engineering Journal*, *455*, 140551. https://doi.org/https://doi.org/10.1016/j.cej.2022.140551

Sarma, G. K. and Rashid, M. H. (2018). Synthesis of Mg/Al Layered Double Hydroxides for Adsorptive Removal of Fluoride from Water: A Mechanistic and Kinetic Study. *Journal of Chemical & Engineering Data*, *63*(8), 2957-2965.

Sato, T., *et al.* (1988). Synthesis of Hydrotalcite-like Compounds and Their Physico-chemical Properties. *Reactivity of Solids*, *5*(2-3), 219-228.

Shah, H. A., *et al.* (2020). Surface and Groundwater Pollution: The Invisible, Creeping Threat to Human Health. *Civil and Environmental Engineering*, *16*(1), 157-169.

Shang, S., *et al.* (2019). Novel M (Mg/Ni/Cu)-Al-CO_3 Layered Double Hydroxides Synthesized by Aqueous Miscible Organic Solvent Treatment (AMOST) Method for CO_2 Capture. *Journal of Hazardous Materials*, *373*, 285-293.

Sharifi-Bonab, M., *et al.* (2020). Synthesis of CoZnAl-Layered Double Hydroxide/Graphene Oxide Nanocomposite for the Removal of Methylene Blue: Kinetic, Thermodynamic, and Isotherm Studies. *Environmental Progress & Sustainable Energy*, *39*(2), e13316.

Sharma, S. and Maréchal, F. (2019). Carbon Dioxide Capture from Internal Combustion Engine Exhaust Using Temperature Swing Adsorption. *Frontiers in Energy Research, 7*, 143.

Sheng, T., *et al.* (2019). Adsorption of Phosphorus by Using Magnetic Mg–Al-, Zn–Al- and Mg–Fe-Layered Double Hydroxides: Comparison Studies and Adsorption Mechanism. *Environmental Science and Pollution Research, 26*(7), 7102-7114.

Shukla, P. R., *et al.* (2022). Climate Change 2022: Mitigation of Climate Change. *Contribution of Working Group III to the Sixth Assessment Report of the Intergovernmental Panel on Climate Change*, *10*, 9781009157926.

Sideris, P. J., *et al.* (2008). Mg/Al Ordering in Layered Double Hydroxides Revealed by Multinuclear NMR Spectroscopy. *Science, 321*(5885), 113-117.

Smalenskaite, A., *et al.* (2017). A Comparative Study of Co-precipitation and Sol-gel Synthetic Approaches to Fabricate Cerium-substituted Mg-Al Layered Double Hydroxides with Luminescence Properties. *Applied Clay Science, 143*, 175-183. https://doi.org/10.1016/j.clay.2017.03.036

Smoláková, L., *et al.* (2017). Determination of Basic Sites in Mg–Al Mixed Oxides by Combination of TPD-CO_2 and CO_2 Adsorption Calorimetry: When the Same Basic Sites are Reported from Both Techniques? *Journal of Thermal Analysis and Calorimetry*, *127*, 1921-1929.

Sokol, D., *et al.* (2019a). Dielectric Properties of Bi-substituted LDHs Synthesized by Co-precipitation and Sol-gel Methods. *Materials Science-Poland*, *37*(2), 190-195. https://doi.org/10.2478/msp-2019-0035

Sokol, D., *et al.* (2019b). Sonication Accelerated Formation of Mg-Al-phosphate Layered Double Hydroxide via Sol-Gel Prepared Mixed Metal Oxides. *Sci Rep, 9*(1), 10419. https://doi.org/10.1038/s41598-019-46910-5

Solovov, V., *et al.* (2018). Synthesis of Ni(II)-Ti(IV) Layered Double Hydroxides Using Coprecipitation at High Supersaturation Method. *ARPN Journal of Engineering and Applied Sciences*, *13*(24), 9652-9656.

Sturchio, M. A. and Knapp, A. K. (2023). Ecovoltaic Principles for a More Sustainable, Ecologically Informed Solar Energy Future. *Nature Ecology & Evolution*, *7*(11), 1746-1749. https://doi.org/10.1038/s41559-023-02174-x

Su, F., *et al.* (2011). Adsorption, Desorption, and Thermodynamic Studies of CO_2 with High-amine-loaded Multiwalled Carbon Nanotubes. *Langmuir*, *27*(13), 8090-8098.

Sun, Y., *et al.* (2014). Atomically-thick Two-dimensional Crystals: Electronic Structure Regulation and Energy Device Construction. *Chem Soc Rev*, *43*(2), 530-546.

Tabana, L., *et al.* (2020). Adsorption of Phenol from Wastewater Using Calcined Magnesium-Zinc-Aluminium Layered Double Hydroxide Clay. *Sustainability*, *12*(10), 4273.

Tan, B. J., *et al.* (1991). XPS Studies of Solvated Metal Atom Dispersed (SMAD) Catalysts. Evidence for Layered Cobalt-Manganese Particles on Alumina and Silica. *Journal of the American Chemical Society*, *113*(3), 855-861.

Tang, N., *et al.* (2018). New Insights into CO_2 Adsorption on Layered Double Hydroxide (LDH)-Based Nanomaterials. *Nanoscale Research Letters*, *13*(1), 55. https://doi.org/10.1186/s11671-018-2471-z

Tang, X., *et al.* (2023). Structure–Performance Correlation Guided Cerium-Based Metal–Organic Frameworks: Superior Adsorbents for Fluoride Removal in Water. *Chemosphere*, *312*, 137335.

Tao, W., *et al.* (2020). Removal of Fluoride from Wastewater Solution Using Ce-AlOOH with Oxalic Acid as Modification. *Journal of Hazardous Materials*, *384*, 121373.

Tian, X., *et al.* (2017). Nano-Geomaterials for Water Treatment.

Tiwari, D., *et al.* (2017). Dynamic CO_2 Capture by Carbon Adsorbents: Kinetics, Isotherm and Thermodynamic Studies. *Separation and Purification Technology*, *181*, 107-122.

Tokudome, Y., *et al.* (2016). Layered Double Hydroxide Nanoclusters: Aqueous, Concentrated, Stable, and Catalytically Active Colloids toward Green Chemistry. *ACS Nano*, *10*(5), 5550-5559. https://doi.org/10.1021/acsnano.6b02110

Trana, H. N., *et al.* (2019). Adsorption Mechanism of Hexavalent Chromium onto Layered Double Hydroxides-based Adsorbents: A Systematic In-depth Review. *Journal of Hazardous Materials*, *373*, 258–270. https://doi.org/10.1016/j.jhazmat.2019.03.018

UNICEF (2024). Access to drinking water - UNICEF DATA, accessed on 25 June 2024.

Valeikiene, L., *et al.* (2019). Transition Metal Substitution Effects in Sol-gel Derived $Mg_{3-x}M_x/Al_1$ (M= Mn, Co, Ni, Cu, Zn) Layered Double Hydroxides. *Materials Chemistry and Physics*, *237*, 121863.

Valeikiene, L., *et al.* (2020). On the Reconstruction Peculiarities of Sol–gel Derived $Mg_{2-x}M_x/Al_1$ (M= Ca, Sr, Ba) Layered Double Hydroxides. *Crystals*, *10*(6), 470.

Velu, S., *et al.* (1997). New Hydrotalcite-like Anionic Clays Containing Zr^{4+} in the Layers. *Chemical Communications* (21), 2107-2108. https://doi.org/10.1039/A704752E

Vigdorowitsch, M., *et al.* (2021). Freundlich Isotherm: An Adsorption Model Complete Framework. *Applied Sciences*, *11*(17), 8078.

Walters, R. (2014). Air Pollution and Invisible Violence. In *Invisible Crimes and Social Harms* (pp. 142-160). Springer.

Wang, B., *et al.* (2022). Basic Intensity Regulation of Layered Double Oxide for CO_2 Adsorption Process at Medium Temperature in Coal Gasification. *Chemical Engineering Journal*, *446*, 136842.

Wang, G., *et al.* (2021). Ternary NiFeMn Layered Metal Oxide (LDO) Compounds for Capacitive Deionization Defluoridation: The Unique Role of Mn. *Separation and Purification Technology*, *254*, 117667.

Wang, N., *et al.* (2014). One-pot Synthesis of Ordered Mesoporous NiCeAl Oxide Catalysts and a Study of Their Performance in Methane Dry Reforming. *ChemCatChem*, *6*(5), 1470-1480.

Wang, P., *et al.* (2023). Recent Advance of Layered Double Hydroxides Materials: Structure, Properties, Synthesis, Modification and Applications of Wastewater Treatment. *Journal of Environmental Chemical Engineering*, *11*(6), 111191. https://doi.org/https://doi.org/10.1016/j.jece.2023.111191

Wang, Q., *et al.* (2010). The Effect of Trivalent Cations on the Performance of Mg-M-CO_3 Layered Double Hydroxides for High-Temperature CO_2 Capture. *ChemSusChem*, *3*(8), 965-973.

Wang, S., *et al.* (2019a). Facile Preparation of Ni–Mn Layered Double Hydroxide Nanosheets/Carbon for Supercapacitor. *Journal of Materials Science: Materials in Electronics*, *30*(8), 7524-7533. https://doi.org/10.1007/s10854-019-01066-w

Wang, X., *et al.* (2019b). In Situ Fabrication of Flaky-like NiMn-Layered Double Hydroxides as Efficient Catalyst for Li-O_2 Battery. *Journal of Solid State Electrochemistry*, *23*(4), 1121-1128. https://doi.org/10.1007/s10008-019-04205-9

Wei, L., *et al.* (2020). Fluoride Removal by Ca-Al-CO_3 Layered Double Hydroxides at Environmentally-relevant Concentrations. *Chemosphere*, *243*, 125307. https://doi.-org/10.1016/j.chemosphere.2019.125307

Wu, S., *et al.* (2017). Solvothermal Synthesis of Nickel–Aluminum Layered Double Hydroxide Nanosheet Arrays on Nickel Foam as Binder-Free Electrodes for Supercapacitors. *Journal of Inorganic and Organometallic Polymers and Materials*, *27*, 1933-1940.

Wu, X., *et al.* (2007). Fluoride Removal Performance of a Novel Fe–Al–Ce Trimetal Oxide Adsorbent. *Chemosphere*, *69*(11), 1758-1764.

Xu, H., *et al.* (2018). Ce-doped NiFe-Layered Double Hydroxide Ultrathin Nanosheets/Nanocarbon Hierarchical Nanocomposite as an Efficient Oxygen Evolution Catalyst. *ACS Applied Materials & Interfaces*, *10*(7), 6336-6345.

Xu, R., *et al.* (2023). A Global-scale Framework for Hydropower Development Incorporating Strict Environmental Constraints. *Nature Water*, *1*(1), 113-122. https://doi.org/10.1038/s44221-022-00004-1

Xu, Y., *et al.* (2021). Mn-promoted CaO-based Adsorbents with Enhanced CO_2 Uptake Performance. *Journal of Natural Gas Science and Engineering*, *94*. https://doi.org/-10.1016/j.jngse.2021.104029

Yagub, M. T., *et al.* (2012). Equilibrium, Kinetics, and Thermodynamics of Methylene Blue Adsorption by Pine Tree Leaves. *Water, Air, & Soil Pollution*, *223*, 5267-5282.

Yang, R., *et al.* (2022). Performance and Mechanism of Lanthanum-modified Zeolite as a Highly Efficient Adsorbent for Fluoride Removal from Water. *Chemosphere*, *307*, 136063.

Yang, Z.-z., *et al.* (2019). A Review on Strategies to LDH-based Materials to Improve Adsorption Capacity and Photoreduction Efficiency for CO_2. *Coordination Chemistry Reviews*, *386*, 154-182. https://doi.org/10.1016/j.ccr.2019.01.018

Yoshikawa, K., *et al.* (2014). Synthesis and Analysis of CO_2 Adsorbents Based on Cerium Oxide. *Journal of CO_2 Utilization, 8*, 34-38. https://doi.org/https://doi.org/10.1016/-j.jcou.2014.10.001

Yu, Y., *et al.* (2015). Adsorption of Fluoride by Fe–Mg–La Triple-metal Composite: Adsorbent Preparation, Illustration of Performance and Study of Mechanisms. *Chemical Engineering Journal*, *262*, 839-846.

Żaba, A., *et al.* (2021). Photodegradation Process of Organic Dyes in the Presence of a Manganese-Doped Zinc Sulfide Nanowire Photocatalyst. *Materials*, *14*(19), 5840.

Zeng, H., *et al.* (2022). Porous Adsorption Materials for Carbon Dioxide Capture in Industrial Flue Gas. *Frontiers in Chemistry*, *10*, 939701.

Zhang, H., *et al.* (2018). Super Adsorption Capability of Rhombic Dodecahedral Ca-Al Layered Double Oxides for Congo Red Removal. *Journal of Alloys and Compounds*, *768*, 572-581. https://doi.org/10.1016/j.jallcom.2018.07.241

Zhang, J., *et al.* (2021). Synthesis of Layered Double Hydroxides with Nitrate and its Adsorption Properties of Phosphate. *Water Science and Technology*, *83*(1), 100-110.

Zhang, M., *et al.* (2020). Effects of the Surface Adsorbed Oxygen Species Tuned by Rare-earth Metal Doping on Dry Reforming of Methane Over Ni/ZrO_2 Catalyst. *Applied Catalysis B: Environmental*, *264*, 118522. https://doi.org/https://doi.org/10.1016/j.-apcatb.2019.118522

Zhao, Y., *et al.* (2015). Ni^{3+} Doped Monolayer Layered Double Hydroxide Nanosheets as Efficient Electrodes for Supercapacitors. *Nanoscale*, *7*(16), 7168-7173.

Zhao, Y., *et al.* (2018). Sub-3 nm Ultrafine Monolayer Layered Double Hydroxide Nanosheets for Electrochemical Water Oxidation. *Advanced Energy Materials*, *8*(18), 1703585. https://doi.org/https://doi.org/10.1002/aenm.201703585

Zhou, H., *et al.* (2021). Application of FeMgMn Layered Double Hydroxides for Phosphate Anions Adsorptive Removal from Water. *Applied Clay Science*, *200*. https://doi.org/-10.1016/j.clay.2020.105903

Zhou, J., *et al.* (2018). Highly Selective and Efficient Removal of Fluoride from Ground Water by Layered Al-Zr-La Tri-metal Hydroxide. *Applied Surface Science*, *435*, 920-927.

Zhu, J., *et al.* (2019). Efficient Degradation of Organic Pollutants by Peroxymonosulfate Activated with MgCuFe-Layered Double Hydroxide. *RSC Advances*, *9*(4), 2284-2291.

Zhu, X., *et al.* (2020). Efficient CO_2 Capture from Ambient Air with Amine-functionalized Mg–Al Mixed Metal Oxides. *Journal of Materials Chemistry A*, *8*(32), 16421-16428. https://doi.org/10.1039/d0ta05079b

Zou, Y., *et al.* (2016). Controllable Synthesis of Ca-Mg-Al Layered Double Hydroxides and Calcined Layered Double Oxides for the Efficient Removal of U(VI) from Wastewater Solutions. *ACS Sustainable Chemistry & Engineering*, *5*(1), 1173-1185. https://doi.org/10.1021/acssuschemeng.6b02550

Zubair, M., *et al.* (2017). Adsorption of Eriochrome Black T from Aqueous Phase on MgAl-, CoAl- and NiFe-Calcined Layered Double Hydroxides: Kinetic, Equilibrium and Thermodynamic Studies. *Journal of Molecular Liquids*, *230*, 344-352.

Appendix A

List of Publications During the PhD Study:

1. Wagassa, A. N., Zereffa, E. A., Shifa, T. A., & Bansiwal, A. Breakthrough Study of CO_2 Adsorption and Regeneration Performance of Mn- and Ce-Doped Ni–Al Layered Double Hydroxides Derived Mixed Oxides in Packed-Bed Column. Advanced Sustainable Systems, 2300558. https://doi.org/10.1002/adsu.202300558

2. A. N. Wagassa, A. Bansiwal, T. A. Shifa and E. A. Zereffa (2024). Ce^{4+}-Substituted Ni–Al mixed oxide: fluoride adsorption performance and reusability. RSC Adv. 14, 2, 1229-1238. DOI: 10.1039/D3RA07690C

3. Wagassa, A.N., Shifa, T.A., Bansiwal, A., Zereffa, E.A. (2023). Kinetics, isotherm, mechanism, and recyclability of novel nano-sized Ce^{4+}-doped Ni–Al layered double hydroxide for defluoridation of aqueous solutions. Environ Sci Pollut Res 30, 119084–119094. https://doi.org/10.1007/s11356-023-30723-1

4. Wagassa, A. N., Tufa, L. T., Lee, J., Zereffa, E. A., & Shifa, T. A. (2023). Controllable Doping of Mn into $Ni_{0.075-x}Mn_xAl_{0.025}(OH)_2(CO_3)_{0.0125}\cdot yH_2O$ for Efficient Adsorption of Fluoride Ions. Global Challenges, 7(6), 2300018. https://doi.org/10.1002/gch2.202300018

5. Ananda Murthy, H., Wagassa, A. N., Ravikumar, C., & Nagaswarupa, H. (2021). Functionalized metal and metal oxide nanomaterial-based electrochemical sensors. Functionalized Nanomaterial-Based Electrochemical Sensors, 369-392. https://doi.org/10.1016/B978-0-12-823788-5.00001-6

6. Synthesis and Characterization of Mn^{2+}-Doped Ni-Al Layered Double Oxides Nanoplates for Fluoride Adsorption: Studies on Adsorption Isotherms, Kinetics, Thermodynamics and Regeneration. Applied Water Science, AWSC-D-23-00891 (under review)

Achievements during the PhD journey:

1. Joining CSIR-TWAS Sandwich Research Fellowship Program of 2021
2. Paper presentation titled "Mesoporous $Ni_{3-x}Mn_xAl(OH)_8(CO_3)_{0.5}\bullet yH_2O$ Layered Double Hydroxide for Efficient Fluoride Capture from Aqueous Media" in the 3rd International

Conference on Water Technologies 2023 (ICWT 2023), IIT Bombay from 4-7th December 2023

3. Participating in G20_2023 India Summit
4. Participation in a webnar on “How Nanoscience and Technology Inspired from Nature and Transforming the World?” organized by Department of Natural Science, AMET, India on 28/04/2021.